Università degli Studi di Napoli "Federico II"

Dottorato di ricerca in Fisica Fondamentale ed Applicata

XX Ciclo

Measurement of the charged kaon lifetime with the KLOE detector

Paolo Massarotti

Coordinatore	*Relatori*
prof. Gennaro Miele	prof. Marco Napolitano
	dott. Fabio Ambrosino

Anno accademico 2006 - 2007

Contents

La speranza è un sogno fatto da svegli.

Aristotele

Io, con tutto il rispetto per Nostro Signore, mi pigliavo qualche giono in più ma le cose venivano meglio.

Afredo
di
"Nuovo cinema paradiso".

Introduction

This Ph.D. thesis has been done in the framework of the KLOE experiment, which was in operation at DAΦNE, the e^+e^- ϕ-factory of the Laboratori Nazionali di Frascati of the Istituto Nazionale di Fisica Nucleare.

The main aim of the KLOE experiment is the measurement of the $\mathcal{CP}$ violation in the $K^0\overline{K^0}$ system, but its detector has the capability to exploit a much more vast physics program, including neutral and charged kaon decays and radiative decays. Actually, since the ϕ mesons decays 49.2% of the time into a K^+K^- pair, DAΦNE is a very rich source of tagged and kinematically constrained charged kaons.

We focused our attention to the measurement of the charged kaon lifetime, whose most recent measurement has been done in 1995. It is important to stress that the only other in-flight measurement has been done in 1969. This quantity is a fundamental parameter for the extraction of the V_{us} element of the CKM matrix, together with all the other inputs measurable at KLOE, namely the semileptonic branching ratios and the form factor slopes.

We present a new measurement of the charged kaon lifetime. In order to cross check systematic effects we developed two different analysis methods, one relying on the reconstruction of the kaon path length and one measuring directly the the kaon decay time, for both the charges. A comparison of the lifetime for the two charges can provide a CPT symmetry test.

The thesis structure goes as follows: in the first chapter I discuss the theoretical aspects of the evaluation of V_{us} via the measurement of the branching ratio of the K_{l3} decay, the charged kaon lifetime and the form factor slopes. I also discuss the other charged kaon lifetime measurements previously performed.

The KLOE detector and its performance are briefly described in the second chapter.

Chapter three is devoted to the description of the data reconstruction and event classification procedures.

The selection of the charged kaons events and their specific re-tracking procedure are described separately in the fourth chapter.

Finally the measurement of the charged kaon lifetime is discussed in last chapter.

Chapter 1

Charged kaon lifetime

The Standard Model is a field-theoretic description of strong and electroweak interactions at the energy of several hundred GeV. In the Standard Model, the fundamental fermionic constituents of matter are the quarks and leptons. Only quarks engage in the strong interactions as a consequence of their color-charge. The charged kaon lifetime measurement, which is my phd thesis work, is an imporant parameter for the determination of V_{us}, an element of the CKM matrix.

1.1   The CKM quark mixing matrix

In the Standard Model with $SU(2) \times U(1)$ as gauge group of electroweak interactions, both the quarks and leptons are assigned to be left-handed doublets and right-handed singlets. The quark mass eigenstates are not the same as the weak eigenstates, and the matrix relating these bases was defined for six quarks and given an explicit parametrization by Kobayashi and Maskawa [1] in 1973. This parametrization generalizes the four-quarks case, where the matrix is parametrized by a single angle, the Cabibbo angle [2]. By convention the mixing is often expressed in terms of 3×3 unitary matrix V_{CKM} operating on the charge $-e/3$ quark mass eigenstates (d,s, and b):

$$
\begin{pmatrix} d' \\ s' \\ b' \end{pmatrix} = \begin{pmatrix} V_{ud} & V_{us} & V_{ub} \\ V_{cd} & V_{cs} & V_{cb} \\ V_{td} & V_{ts} & V_{tb} \end{pmatrix} \cdot \begin{pmatrix} d \\ s \\ b \end{pmatrix} \tag{1.1}
$$

There are several parameterizations of the Cabibbo-Kobayashi-Maskawa (CKM) matrix. The most relevant are the "standard" one [3], based on three angles and one phase, and the Wolfenstein's parametrization [4]. The "standard" parametrization allows to write V_{CKM} using three angles $\theta_{12}, \theta_{23}, \theta_{13}$ and a phase δ_{13}:

$$V_{CKM} = \begin{pmatrix} c_{12}c_{13} & s_{12}c_{13} & s_{13}e^{-i\delta_{13}} \\ -s_{12}c_{23} - c_{12}s_{23}s_{13}e^{i\delta_{13}} & c_{12}c_{23} - s_{12}s_{23}s_{13}e^{i\delta_{13}} & s_{23}c_{13} \\ s_{12}s_{23} - c_{12}c_{23}s_{13}e^{i\delta_{13}} & -c_{12}s_{23} - s_{12}c_{23}s_{13}e^{i\delta_{13}} & c_{23}c_{13} \end{pmatrix} \qquad (1.2)$$

with $c_{ij} = cos\theta_{ij}$ and $s_{ij} = sin\theta_{ij}$ for the generation labels $i, j = 1, 2, 3$. This has distinct advantages of interpretation, for the rotation angles are defined and labeled in a way that relates to the mixing of two specific generations and if one of these angles vanishes, so does the mixing between those two generations; in the limit $\theta_{23} = \theta_{13} = 0$ the third generation decouples, and the situation reduces to the usual Cabibbo mixing of the first two generations with θ_{12} identified with the Cabibbo angle.
The Wolfenstein parametrization emphasizes the hierarchy in the size of the angles $s_{12} \gg s_{23} \gg s_{13}$. It is possible to set $\lambda \equiv s_{12}$ and then to write the other elements in terms of powers of λ:

$$V_{CKM} = \begin{pmatrix} 1 - \lambda^2/2 & \lambda & A\lambda^3(\rho - i\eta) \\ -\lambda & 1 - \lambda^2/2 & A\lambda^2 \\ A\lambda^3(1 - \rho - i\eta) & -A\lambda^2 & 1 \end{pmatrix} + \mathcal{O}(\lambda^4) \qquad (1.3)$$

with A, ρ and η real numbers that were intended to be of order unity.
Theoretical prediction do not depend on which of the possible parameterizations is used, as long as a single one is used consistently and care is taken to be sure that no other choice of phases is in conflict. The values of individual matrix elements can in principle be all determined from weak decays of the relevant quarks, or from deep inelastic neutrino scattering. Assuming only three generations and the constraints from experimental values, the 90% confidence limits on the magnitude of the elements of the complete matrix are:

$$\begin{pmatrix} 0.9739 \div 0.9751 & 0.221 \div 0.227 & 0.0029 \div 0.0045 \\ 0.221 \div 0.227 & 0.9730 \div 0.9744 & 0.039 \div 0.044 \\ 0.0048 \div 0.014 & 0.037 \div 0.043 & 0.9990 \div 0.9992 \end{pmatrix}. \qquad (1.4)$$

The ranges shown are for the individual matrix elements. The constraints of unitarity connect different elements, so choosing a specific value for one element restricts the range of the others.

1.2   The CKM unitarity problem

The unitarity constraint $\sum_i V_{ij}^* V_{ik} = \delta_{jk}$ on the CKM matrix written for its first row states

$$|V_{ud}|^2 + |V_{us}|^2 + |V_{ub}|^2 = 1 \qquad (1.5)$$

Since $|V_{ub}|^2 \simeq 19(7) \cdot 10^{-6}$ [5] is negligibly small, the unitarity relation (1.5) reduces to

$$|V_{ud}|^2 + |V_{us}|^2 = 1. \tag{1.6}$$

If a deviation from unitarity is seen, it signals the presence of unaccounted physics by the Standard Model. Otherwise if unitarity is respected, constraints on new physics can be implied.

The value of $|V_{ud}|$ can be determined from three distinct sources: nuclear super-allowed $0^+ \to 0^+$ Fermi beta decays, the decay of the free neutron, and pion beta decay [6]. The results provided by these three methods are in agreement within the errors.

Measurement method	$|V_{ud}|$
Nuclear super-allowed Fermi β-decays	0.97377 ± 0.00027
Free neutron decay	0.9746 ± 0.0018
Pion β-decay	0.9728 ± 0.0030

Table 1.1: Values of $|V_{ud}|$ provided by the three possible measurements [6].

The value of $|V_{us}|$ can be obtained via the study of semileptonic K_{e3}, $K_{\mu3}$ and hyperons decays [7], and via the ratio of $K_{\mu2}$ and $\pi_{\mu2}$ decays [8].

The formula which allows to obtain $|V_{us}|$ starting from the study of K_{e3} decays is [7]:

$$\Gamma(K \to \pi e \nu(\gamma)) = \frac{BR(K_{e3})}{\tau_K} = \frac{G_F^2 m_K^5}{192\pi^3} |V_{us}|^2 |f_+(0)|^2 S_{EW} C_K^2 I_K^e (1 + \delta_K^e) \tag{1.7}$$

where

- $C^2 = 1$ for $K_{S,L}$ (for both $\pi^\pm e^\mp$ decays) and $C^2 = 1/2$ for $K^\pm$;

- $S_{EW} = 1.022$ is the Sirlin term which takes in account the short-distance radiative correction [9];

- $\delta_{K^0}^e = (+1.3 \pm 0.3)\%$ and $\delta_{K^+}^e = (-0.1 \pm 0.7)\%$ are model dependent long-distance QED corrections [10];

- the form factor $f_+(0) = f_+^{K^0\pi^-} = 0.961 \pm 0.008$ incorporates $SU(3)$ breaking, it has been evaluated by Leutwyler and Roos and has been recently confirmed by χPT [11] and lattice [12] calculations; in the case of charged kaons $f_+^{K^+\pi^0} \simeq 1.022\ f_+^{K^0\pi^-}$;

- I_K^e is a phase space factor and it is function of the slope of the form factor.

For several years the PDG has reported values of $|V_{ud}|$ and $|V_{us}|$ in slight disagreement with unitarity. In the last four years new measurements have been performed and the experimental picture is changed. The 2006 PDG [6] gives
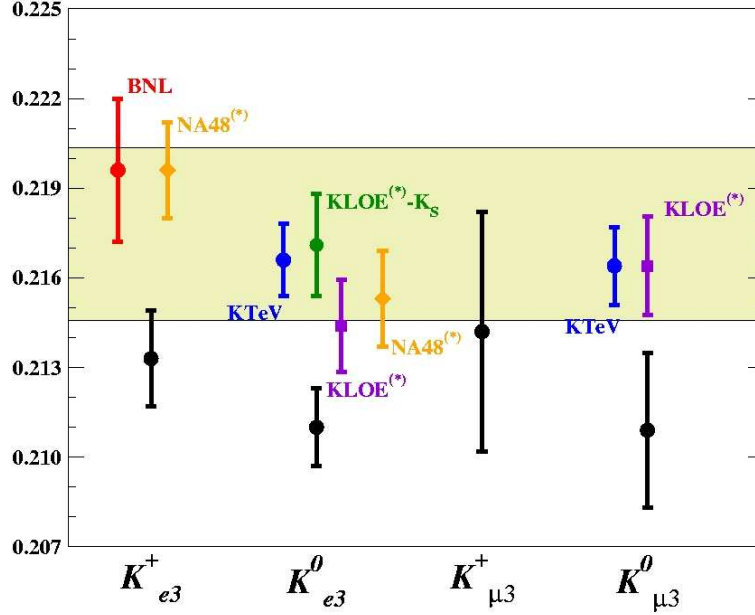
Figure 1.1: Summary of the 2004 $|V_{us}|f_+(0)$ measurement, shown by F. Mescia at the conference ICHEP 2004 [14]. In black the 2002 PDG values.

$$|V_{ud}| = 0.9738 \pm 0.0003 \qquad (1.8)$$
$$|V_{us}| = 0.2257 \pm 0.0021 \qquad (1.9)$$

from which the sum of the squares is $|V_{ud}|^2 + |V_{us}|^2 = 0.9992 \pm 0.0011$ with a deviation smaller than one σ; this result is however based on the so called PDG fit.

1.3   KLOE results and V_{us} determination

At the conference Kaon07, at the "Laboratori Nazionali di Fascati, KLOE presented the measurements of the branching ratios of K_{Se3}, K_{Le3}, $K_{L\mu3}$, K_L lifetime and the preliminary measurements of the the branching ratios of K_{e3}^+, $K_{\mu3}^+$ and K^+ lifetime [15]:

$$BR(K_S^0 \rightarrow \pi^\pm e^\mp \nu) = (7.046 \pm 0.091) \cdot 10^{-4}$$
$$BR(K_L^0 \rightarrow \pi^\pm e^\mp \nu) = 0.4049 \pm 0.0021$$
$$BR(K_L^0 \rightarrow \pi^\pm \mu^\mp \nu) = 0.2726 \pm 0.0016$$
$$BR(K^\pm \rightarrow \pi^0 e^\pm \nu) = (4.965 \pm 0.052) \cdot 10^{-2}$$
$$BR(K^\pm \rightarrow \pi^0 \mu^\pm \nu) = (3.233 \pm 0.039) \cdot 10^{-2}$$

$$(1.10)$$

$$\begin{aligned}
\tau(K_L^0) &= (50.92 \pm 0.0030) \text{ ns} \\
\tau(K^\pm) &= (12.384 \pm 0.048) \text{ ns}
\end{aligned}$$

$$(1.11)$$

From those results, and using the ones given by ISTRA+, KTeV, NA48 and PDG [26], we can extract:

$$|V_{us}| \cdot f_+^{K_{Se3}}(0) = 0.21554 \pm 0.00142 \qquad (1.12)$$

$$|V_{us}| \cdot f_+^{K_{Le3}}(0) = 0.21638 \pm 0.00055 \qquad (1.13)$$

$$|V_{us}| \cdot f_+^{K_{L\mu3}}(0) = 0.21678 \pm 0.00067 \qquad (1.14)$$

$$|V_{us}| \cdot f_+^{K_{e3}^\pm}(0) = 0.21746 \pm 0.00085 \qquad (1.15)$$

$$|V_{us}| \cdot f_+^{K_{\mu3}^\pm}(0) = 0.21810 \pm 0.00114. \qquad (1.16)$$

Their average is:

$$|V_{us}| \cdot f_+(0) = 0.21668 \pm 0.00045 \qquad (1.17)$$

The $|V_{us}|$ question (summarized in figure 1.2) is moving, the CKM unitarity seems to be safe even if problems of the different values obtained using neutral or charged kaons still remains and the theorical picture is on work.

1.4 Experimantal picture

Present knowledge of $\tau(K^\pm)$ comes from five measurements performed between 1965 and 1995. The PDG average [26]

$$\tau = (1.2386 \pm 0.0024) \cdot 10^{-8}\text{s}. \qquad (1.18)$$

However this average stems from five measurements which are not in agreement between each other, and whose errors must be multiplied by a factor 2.1 in order to obtain $\chi^2 \approx$ number of degrees of freedom. The discrepancies between the only "in-flight" [27] measurement and the "at-rest"[29], [28], [30] measurements calls for a new "in flight" determination of this quantity. The statistical error on the lifetime measurements depends on the numbers of events collected and on the time interval covered in the measurement:

$$\frac{\delta\tau}{\tau} = \frac{1}{\sqrt{N}} \times \left[\frac{e^{3T} - 1 + (e^T - e^{2T})(3 + T^2)}{(e^T - 1)^3}\right]^{-0.5} \qquad (1.19)$$
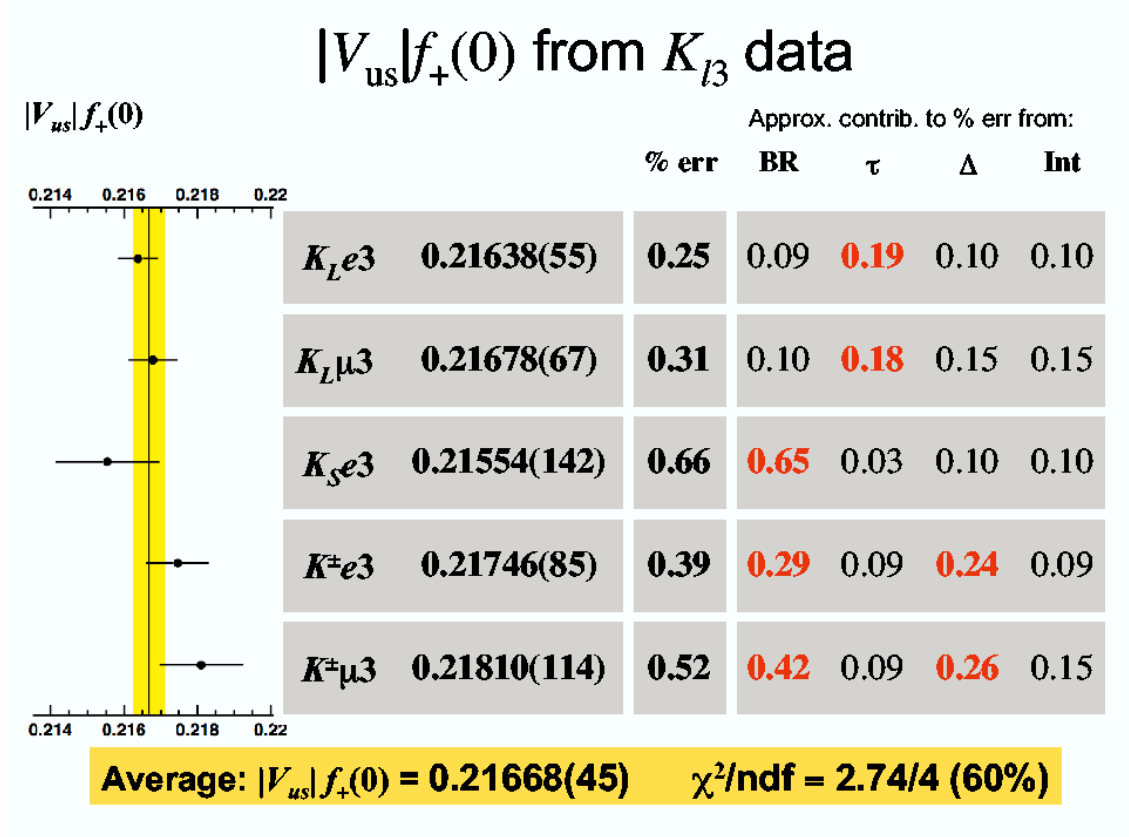
Figure 1.2: Summary of the $|V_{us}|f_+(0)$ measurement, by M. Palutan Kaon07 [15].

$\tau(\mathrm{K}^{\pm})(10^{-8})$s	Autor	Date	Comment
1.2451±0.0030	KOPTEV	95	K at rest, U target
1.2368±0.0041	KOPTEV	95	K at rest, Cu target
1.2380±0.0016	OTT	71	K at rest
1.2272±0.0036	LOBKOWICZ	69	K in flight
1.2443±0.0038	FITCH	65	K at rest

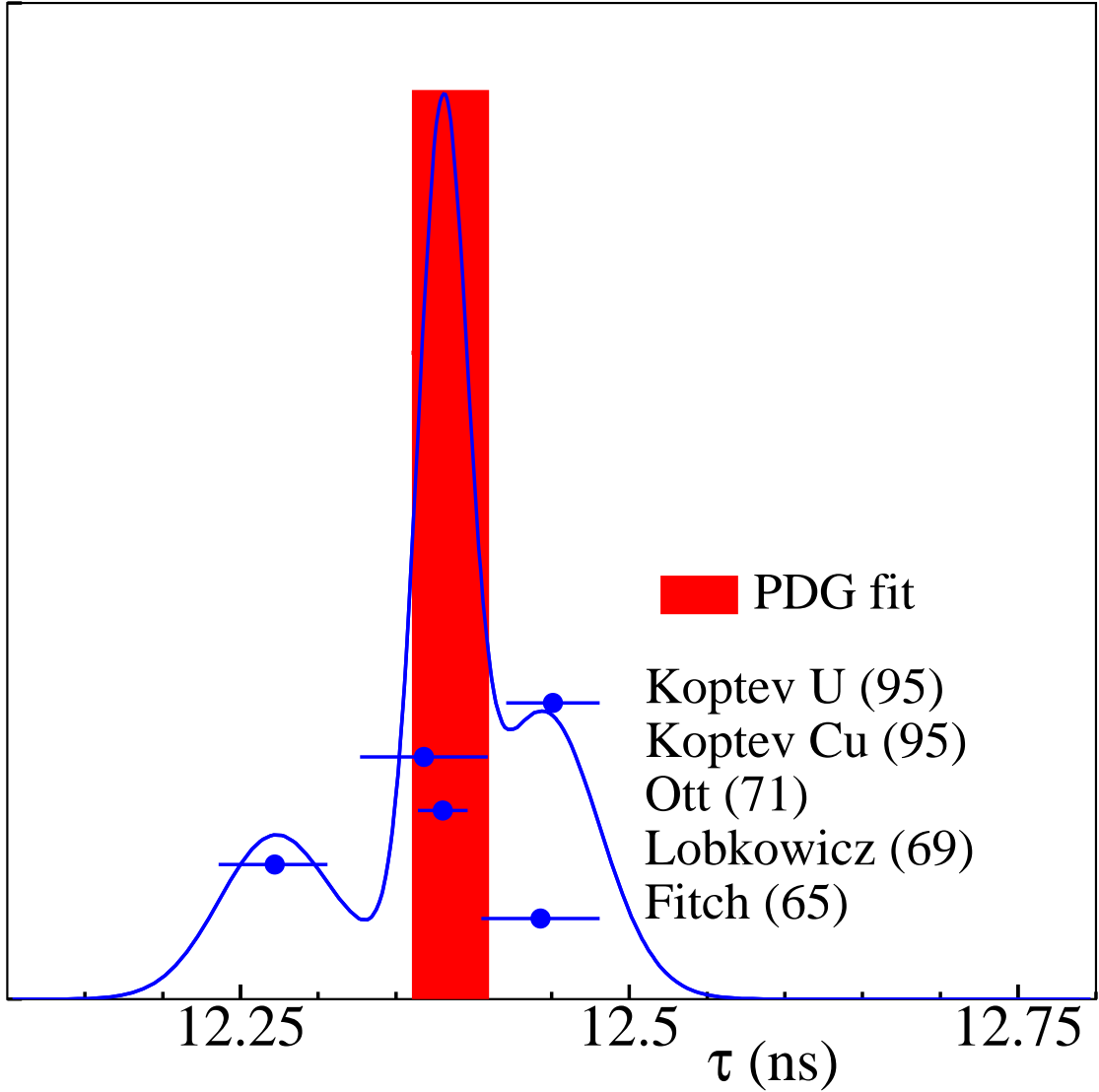Table 1.2: Measurements of the charged kaon lifetime quoted by PDG(2006) [26].

Figure 1.3: Charged kaon lifetime quoted by PDG.

run	1	2	3	4
N	944,000	381,000	981,000	720,000
$\delta\tau_{stat}$, ns, Ott	0.0072	0.0107	0.0071	0.0080
$\delta\tau_{stat}$, ns, min	0.0133	0.0209	0.0139	0.0152
ratio	1.85	1.96	1.84	1.90
$\delta\tau_{syst}$, ns, Ott	0.0261	0.0278	0.339	0.299

Table 1.3: Analysis of the statistical and systematic error of the most precise measurement of the K^+ lifetime [28]

where T = Δt/τ is the fitted time interval in K$^\pm$-lifetime units. The most precise measurement used in PDG average (namely [28]) divide the data-taking in four runs. For each run they evaluate the statistical and the systematical error (see table 1.3). As it is possible to see in the table 1.3, Ott quotes a statistical error smaller than the best one obtainable with eq. 1.19 by a factor $\approx$ 2. The systematic errors are averaged run by run in order to obtain a systematic error as smaller as possible:

$$\sigma_{syst} \approx 0.01 \text{ ns} .$$ (1.20)

It seeems more reliable that the systematic error is common to all the runs; one could take the average:

$$\sigma_{syst} \approx 0.0294 \text{ ns} .$$ (1.21)

The more reliable estimation for the K^+ lifetime of the experiment [28] is:

$$\tau(K^+) = (12.380 \pm 0.0074_{stat} \pm 0.0294_{syst}) \text{ ns} =$$
$$(12.380 \pm 0.030) \text{ ns } \textbf{vs } (12.380 \pm 0.016) \text{ ns} .$$ (1.22)

The most recent measurements [30] have been done in 1995 using two different stopper. They also measure the π^+ lifetime which does not change in Cu, C and SiO$_2$. Therefore the conclude there are no systematic uncertainties due to nuclear interaction. Then they measure the K^+ lifetime and find 12.368$\pm$0.041 in Cu and 12.451$\pm$0.030 in U. It is important to stress that the systematic check with pions has no relevance for kaons, the former being a case of so called surface beam, and that the probability of a statistical fluctuation is 10%. We have also to note that the weighted mean quoted in [30] had been obtained using as weigth $1/\sigma$ instead of $1/\sigma^2$. It is more reliable take ane half the difference as systematic error due to nuclear interaction, then they would obtain:

$$\tau(K^+) = (12.422 \pm 0.024_{stat} \pm 0.048_{syst}) \text{ ns} =$$
$$(12.422 \pm 0.053) \text{ ns } \textbf{vs } (12.415 \pm 0.024) \text{ ns} .$$ (1.23)

The only in "flight" measurement has been done by Lobkowick et al. in 1969 [27]. They fist measure 1 - $\tau(K^+)/\tau(K^-)$ and then they measure the K^-, not K^+, lifetime obtaining, as first evaluation, $\chi^2 = 52.8$ for four degrees of freedom. Then the statistical errors are enlarged by a factor $(\frac{1}{4}\chi^2)^{1/2}$. The motivation for this correction is a not perfect evaluation of the kaon momentum but a similar bias, which does not

affect the 1 - $\tau(K^+)/\tau(K^-)$ measurement, could give also a shift in the lifetime measurement.

If we avegare the modified measurements in eq. 1.22, 1.23 and the Fitch one we obtain:

$$\tau(K^+) = (12.407 \pm 0.021) \text{ ns } . \tag{1.24}$$

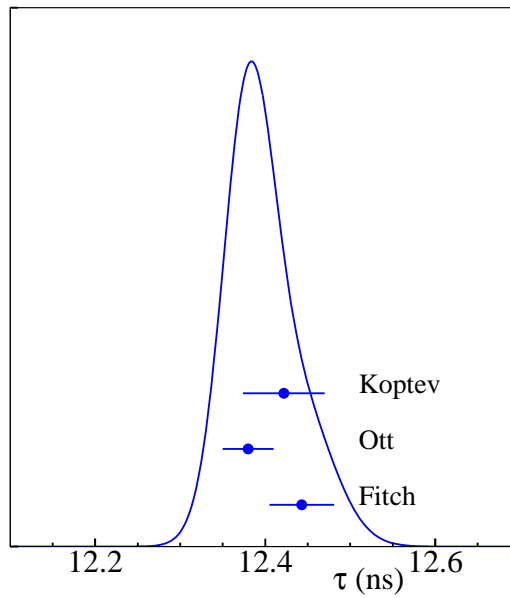This new measurement is thus necessary in order to clarify the present experimental scenario.

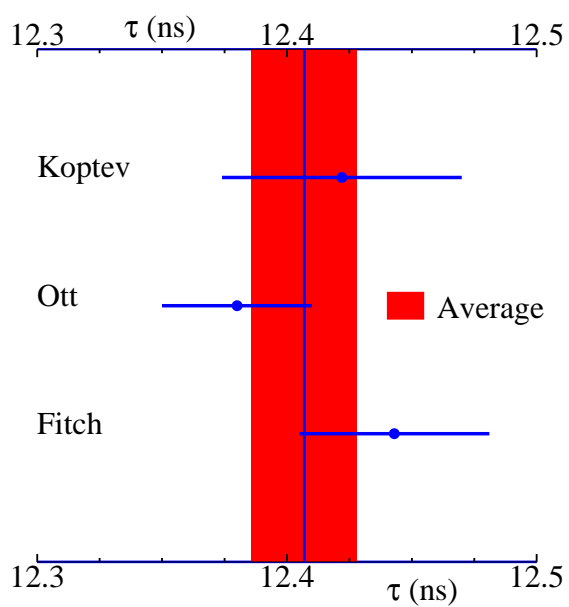Figure 1.4: Charged kaon lifetime distribution using the correct values given in the text.

Figure 1.5: Charged kaon lifetime average using the correct values given in the text.

Chapter 2

The KLOE experiment at DAΦNE

The KLOE experiment has been recording e^+e^- collisions at DAΦNE, the ϕ–factory at Laboratori Nazionali in Frascati, since April 1999. In March 2006, it was successfully concluded. In this chapter the DAΦNE collider and the KLOE detector are presented. Also an overview of the MonteCarlo simulation of the experiment is given.

2.1   The collider DAΦNE

DAΦNE (Double Anular ϕ–factory for Nice Experiments) [31] is an electron-positron collider, designed to work at the center of mass energy $\sqrt{s} \simeq 1020$ MeV, corresponding to the resonance peak of the vector meson ϕ, with mass $M_\phi = (1019.460 \pm 0.019)$ MeV [26], see Figure 2.1.
Electron and positron beams are stored in two separate rings, to reduce beam–beam effects. The two rings intersect in two collision points, IP, with an horizontal half crossing angle of $\pm$ 12.5 mrad, which results in a small momentum component ($\sim$ 13 MeV in the horizontal plane) of the ϕ mesons produced. At one the KLOE detector is located, while the other is alternatively occupied by two experiments: DEAR and FINUDA to study atomic and nuclear physics. The DAΦNE design accepts a maximum number of 120 bunches corresponding to a bunch crossing period of 2.7 ns. The finite crossing angle results in a small average ϕ momentum of about 13 MeV along the transverse x–axis. The main parameters of the collider corresponding to the last KLOE run are listed in Table 2.1.
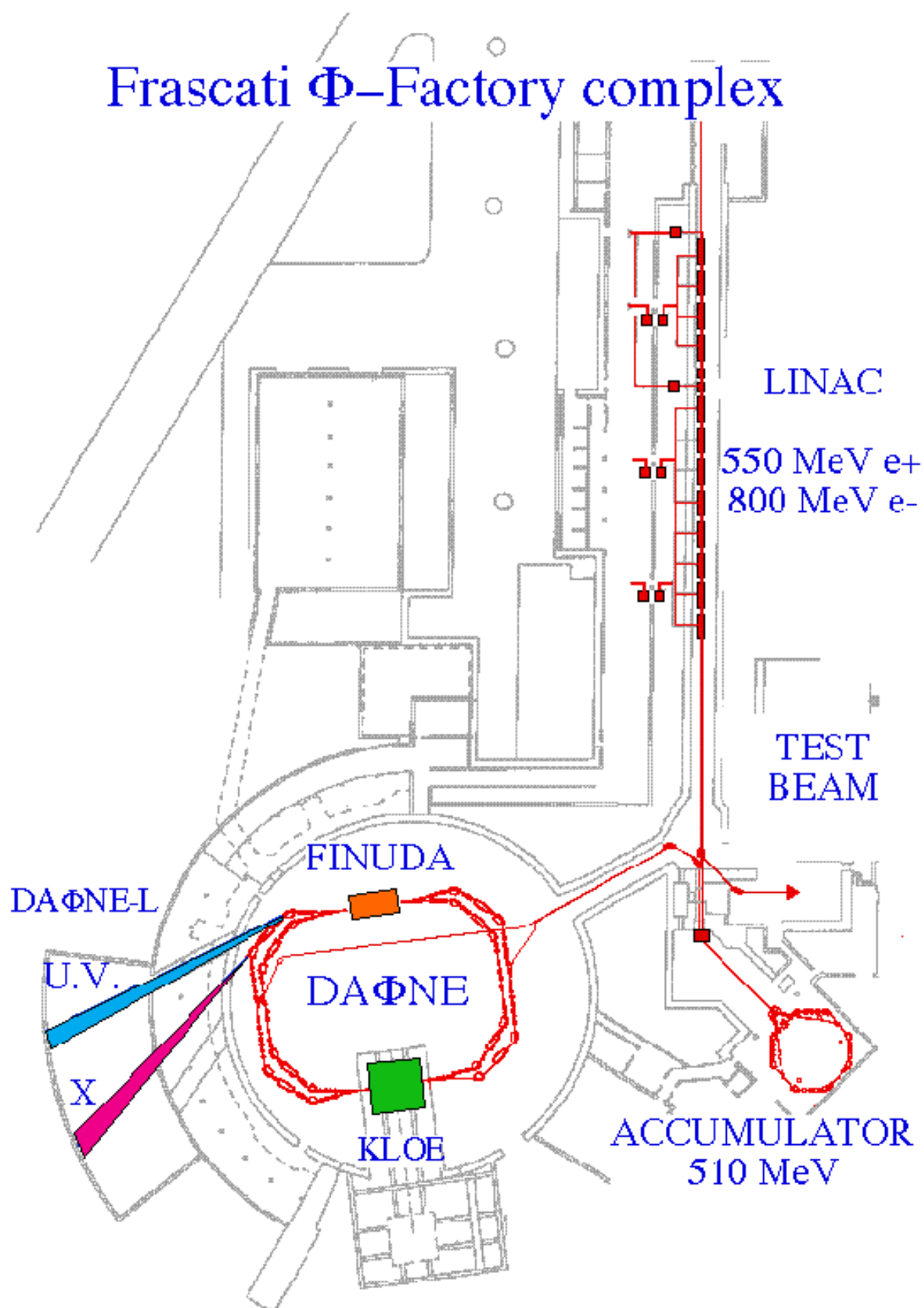
Figure 2.1: Scheme of the DAΦNE collaider apparatus.

Energy	0.51 GeV
Trajectory lenght	97.69 m
RF frequency	368.26 MHz
Harmonic number	120
Damping time, τ_E/τ_x	17.8/36.0 ms
Beam current e^-e^+	2/1.4 Amps
Number of colliding bunches	111
Beta functions β_x/β_y	1.7/0.017 m
Emittance, ε_x (KLOE)	0.34 mm mrad
Coupling at 0 current	0.3 %
Tunes ν_x/ν_y	0.091/0.166 e^- 0.109/0.191 e^+

Table 2.1: DAΦNE Parameter list.

2.2 The DAΦNE luminosity at KLOE

First collisions in the KLOE interaction region after the KLOE installation were detected on April 14, 1999. During the first data taking (1999 ÷ 2000), a total integrated luminosity of $\simeq 2.4$ pb^{-1} has been collected, with istantaneous luminosity peak between 3 and $5 \cdot 10^{30}$ cm^{-2} s^{-1}. This value lower than the one expected $(5 \cdot 10^{32}$ cm^{-2} s$^{-1})$ has been improved with some changes:

- the magnetic field of KLOE has been reduced from 6 to 5.6 kGauss,

- the KLOE interaction region has been modified in the optics and supports,

- colliding current has been increased due to the vacuum conditioning and the continuous improvements of the feedback system.

In the 2004 ÷ 2006 KLOE run, DAΦNE has delivered an integrated luminosity in excess of 2 fb^{-1} on energy 1019.4 MeV see Figure 2.2 and, in the last part of the run > 0.25 fb^{-1} off peak 1000 MeV.
A high statistic scan of the ϕ resonance has been also performed collecting more than 10 pb^{-1} per point at 4 different energies (1010, 1018, 1023, and 1030 MeV).
As shown in Figure 2.3 the machine performance have been continuosly improving during the on-energy run. The highest peak and daily integrated luminosities measured by KLOE have been $L_{peak} = 1.53 \cdot 10^{32}$ cm^{-2} s^{-1} and $L_{day} = 10$ pb^{-1}, respectively.
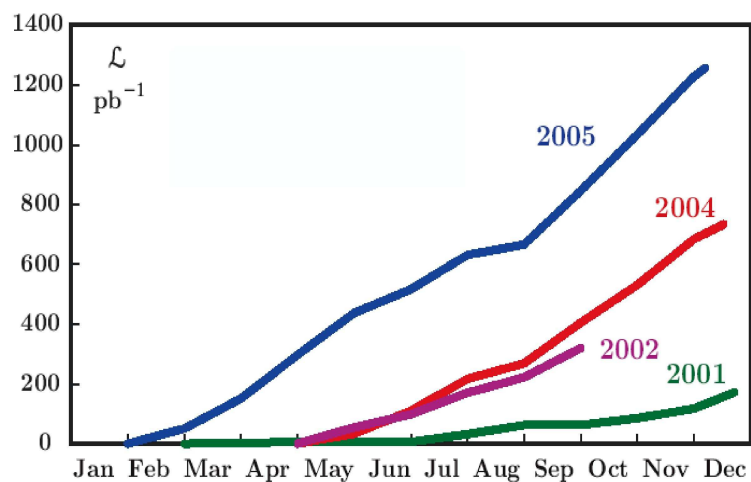
Figure 2.2: Integrated luminosity in pb^{-1} as function of the number of days of data taking for the years 2001 ÷ 2005.
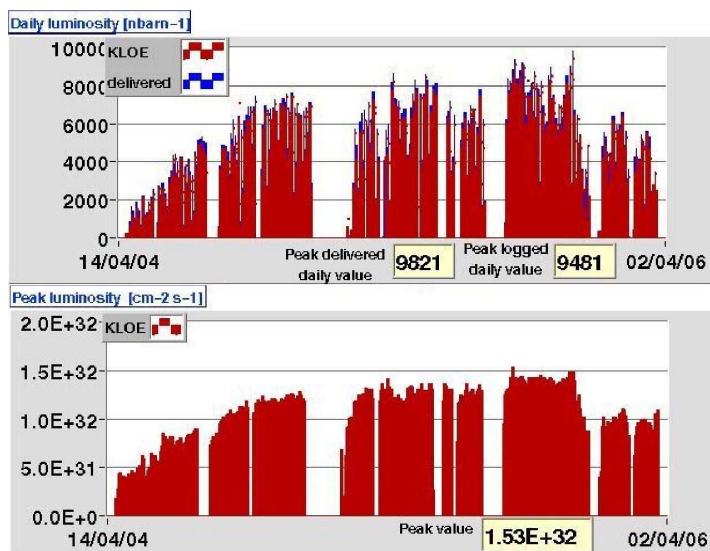

Figure 2.3: Last KLOE run peak and integrated luminosity.

2.3 The KLOE detector

The KLOE detector consist of a superconducting coil able to furnish a magnetic field up to 6 kGauss, whose iron return is designed to keep the field as much as possible uniform and parallel to the beam axis; a drift chamber, to track the charged particles; an electromagnetic calorimeter, to detect neutral particles; two more tile calorimeters surrounding the quadrupoles, to complete the calorimetric hermeticity. A section of the KLOE detector is shown in Figure 2.3. In the following we will refer to an axes system where the z–axis lies along the beams and the x and y–axes are the standard ones, x horizontal and y vertical.

Decay channels	Momenta (Mev/c)
$K_{S,L} \to \pi^+\pi^-$	$155 \leq p_\pi \leq 256$
$\pi \to \mu\nu$	$p_\mu \leq 280$
$K_L \to \pi e \nu$	$p_\pi \leq 300$
	$p_e \leq 260$
$K_L \to \pi\mu\nu$	$p_\pi \leq 260$
	$p_\mu \leq 260$
$K_L \to \pi^0\pi^0$	$160 \leq p_{\pi^0} \leq 270$
$\pi^0 \to \gamma\gamma$	$20 \leq p_\gamma \leq 280$
$K_L \to \pi^+\pi^-\pi^0$	$p_\pi \leq 170$
$\phi \to K^+K^-$	$120 \leq p_K \leq 135$
$K^\pm \to \mu^\pm\nu$	$300 \leq p_\mu \leq 320$
$K^\pm \to \pi^\pm\pi^0$	$270 \leq p_\pi \leq 280$
$\pi^0 \to \gamma\gamma$	$20 \leq p_\gamma \leq 180$
$K^\pm \to \pi^0 e^\pm\nu$	$p_e \leq 300$
$\pi^0 \to \gamma\gamma$	$20 \leq p_\gamma \leq 325$
$K^\pm \to \pi^0\mu^\pm\nu$	$p_\mu \leq 290$
$\pi^0 \to \gamma\gamma$	$20 \leq p_\gamma \leq 310$
$K^\pm \to \pi^\pm\pi^+\pi^-$	$p_\pi \leq 190$
$K^\pm \to \pi^\pm\pi^0\pi^0$	$p_\pi \leq 180$
$\pi^0 \to \gamma\gamma$	$20 \leq p_\gamma \leq 135$

Table 2.2: Momenta of the particles involved in some of the K_L and $K^\pm$ decays.

2.3.1 The beam-pipe

The interaction region consists of a sphere (see Figure 2.6) of 10 cm radius, corresponding to $\sim 17K_S$ decay length in order to avoid regeneration.
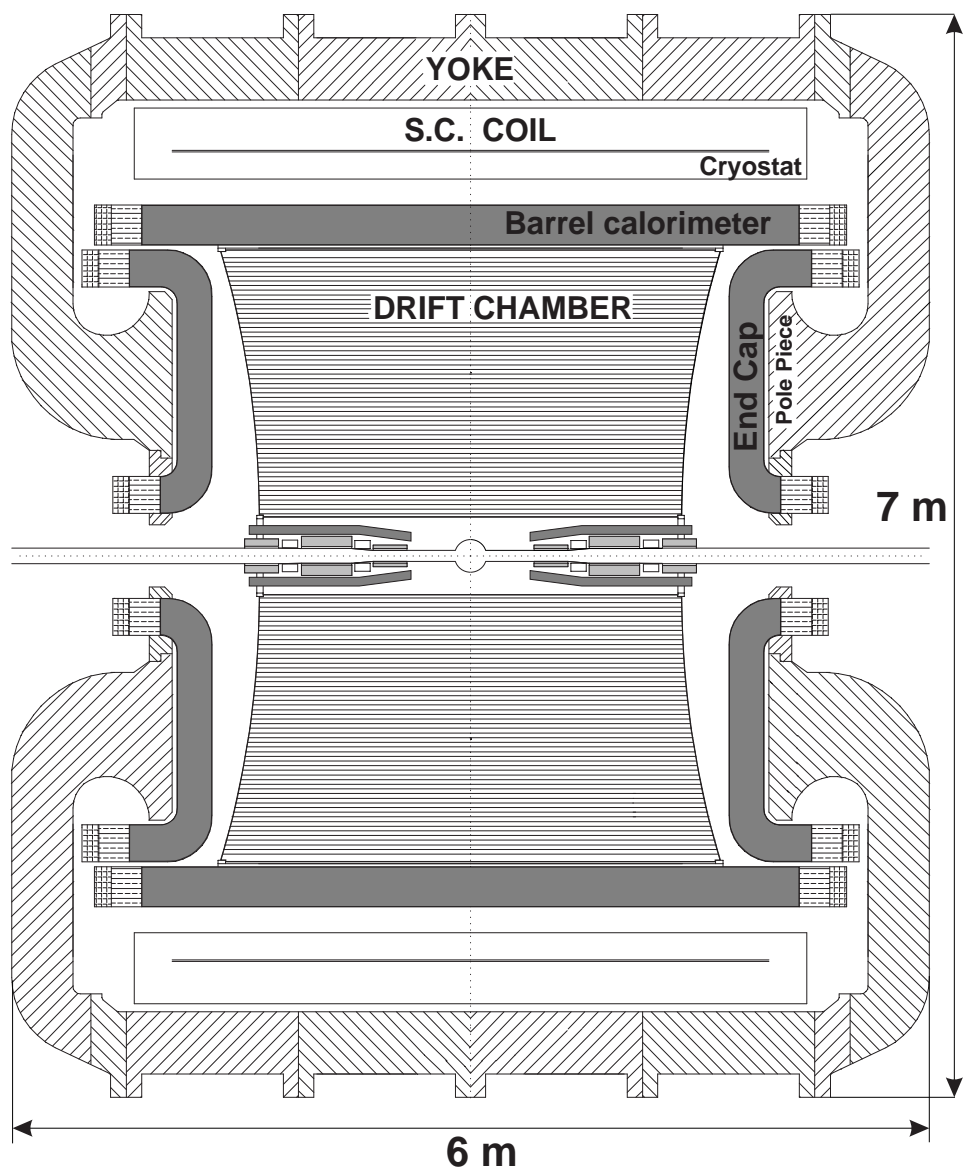
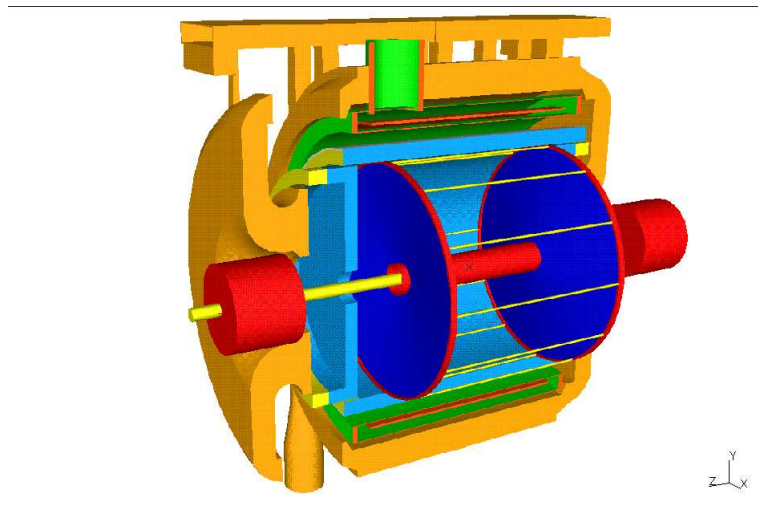Figure 2.4: Vertical transverse section of the KLOE detector.

Figure 2.5: 3D view of the KLOE detector.

The wall of the beam-pipe is made of AlBeMet, an alloy of beryl-aluminum 60%–40% with thickness 0.5 mm. A small layer of beryl, thick 0.05 mm guarantees continuity to the pipe inside the sphere. Beryl has been chosen because of its low atomic number in order to reduce multiple scattering, regeneration, energy loss of particles and photon conversion.

2.3.2 The drift chamber

The KLOE tracking detector is a cylindrical drift chamber [32], see Figure 2.7, whose length is variable from 2.8 m near the beam-pipe to 3.3 m near the calorimeter walls; the outer radius is 2 m, the inner radius is 25 cm. The drift chamber has the following properties:

- high and uniform reconstruction efficiency over a large volume, in order to reconstruct correctly particles that decay inside its sensitive volume (such as K_L);

- very good momentum resolution $(\Delta p_\perp/p_\perp)$ for low momentum tracks $(50 < p < 300$ MeV). In this energy range the dominant contribution to the momentum resolution is multiple scattering:

$$\frac{\Delta p_\perp}{p_\perp} = \frac{0.053}{|B|L\beta}\sqrt{\frac{L}{X_0}}$$

where $p_\perp$ is the transverse momentum in GeV, β is the velocity of the particle, L is the total track length in m, B is the magnetic field in T and X_0 is the radiation length;

Figure 2.6: The beam–pipe.

Figure 2.7: The KLOE drift chamber at the end of the wire stringing.

- it is transparent to low energy photons (down to 20 MeV);

- track resolution in the transverse plane $\sigma_{R\phi} \simeq 200$ μm and a vertex resolution $\sigma_{vtx} \simeq 1$ mm.

The chamber has a uniform cell structure. The uniform filling of the chamber has been achieved through a structure of drift cells "almost" square shaped (see Figure2.8), arranged in coaxial layers with alternating stereo angles which increases in magnitude with radius from ± 60 to ± 150 mrad.
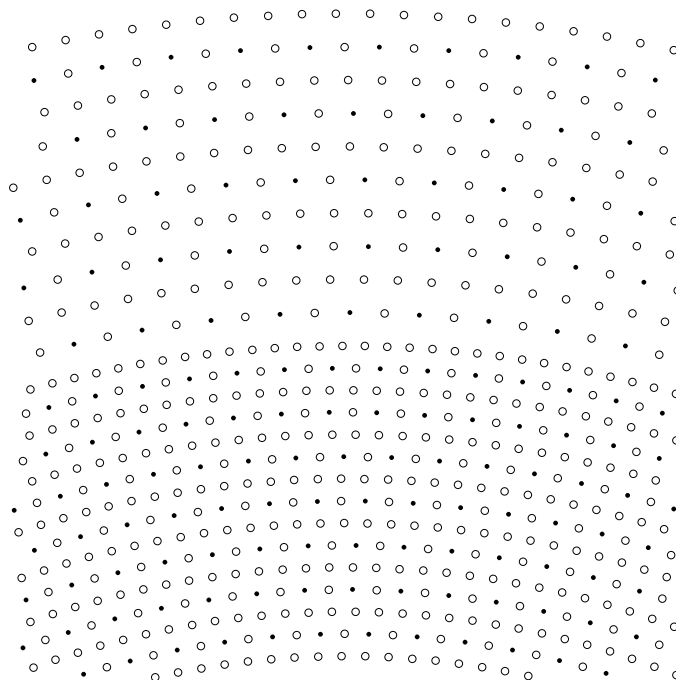
Figure 2.8: Drift cells configuration at $z = 0$; a portion of chamber at boundary between small cells (inner layers) and big cells (outer layers) is shown. Full dots indicate sense wires, circles indicate field wires.

The stereo angle is defined as the angle between the wire and a line parallel to the z–axis passing through the point on the plate of the DC, where the wire is connected, see Figure 2.9. The ratio of field to sense wires (3:1) is a satisfactory compromise in maximizing the track sampling frequency, while maintaining the electrostatic stability of the drift cell. The sense wires are made of gold-plated tungsten and their diameter is 25 μm. The field wires are made of silver-plated aluminum and their diameter is 80 μm; to the field wires are applied ~ 1900 V. There are 12 inner and 46 outer layers, the corresponding cell areas are 2×2 and 3×3 cm^2, respectively, for a total of 12582 single-sense-wire cells and 52140 wires.

Materials were chosen in order to minimize the density along the path of neutral kaons, charged particles and photons. A carbon fiber composite ($\leq 0.1X_0$) has been
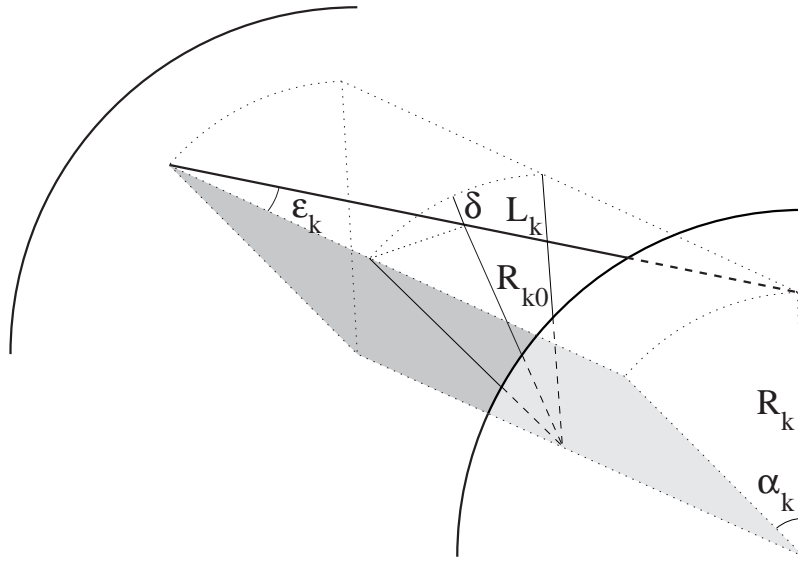
Figure 2.9: KLOE drift chamber geometry: the z-axis is defined along the beam direction. The stereo angle ε_k is defined in such a way that the *stereo drop* δ is constant.

chosen for the chamber shell.

The gas used is a 90% helium, 10% isobutane mixture. The helium is the active component of the mixture and thanks to its low atomic mass reduces the effect of multiple scattering and regeneration. The isobutane acts like quencher, it absorbs UV photons produced in recombination processes in order to avoid the production of discharges in the DC, it can't be more than 10% due to its flammability. The mixture has a radiation length $X_0 \simeq 1300$ m, while taking into account also the presence of the wires, the average radiation length in the whole chamber volume is about $X_0 \simeq 900$ m.

The cell efficiency is determined using cosmic ray tracks with more than 96 hits. The "hardware efficiency" is defined as the ratio of the number of hits found in a cell to the number of tracks crossing the cell. This efficiency is $\simeq 99.6\%$ both for small and big cells and it is costant over the whole drift chamber volume. The "software efficiency" is defined requiring the hit found in the cell to be used by the track fit and it is $\simeq 97\%$. The "software" and "hardware" efficiencies are show in Figure 2.11. As can be seen, the software efficiency is lower for small drift distances, this is due to the worse resolution close to the wires due to non-linearity of space to time (s–t) relations.

Using samples of Bhabha–scattering events, the momentum resolution for 510 MeV $e^{\pm}$ has been evaluated. It can be seen in Figure 2.12 that for $50° < \theta < 130°$ (θ being the angle between the z-axis and the direction of the particle, polar angle of emission) the momentum resolution are $\sigma_p \simeq 1.3$ MeV and $\sigma_p/p = 2.5 \times 10^{-3}$.
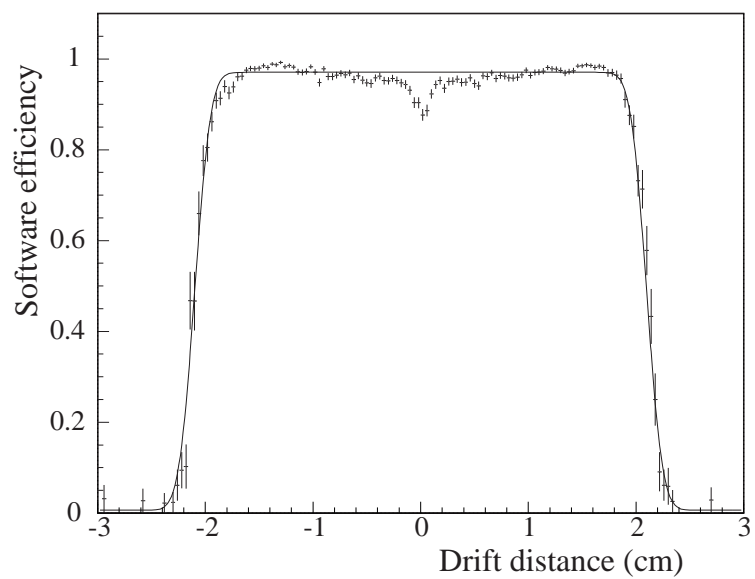
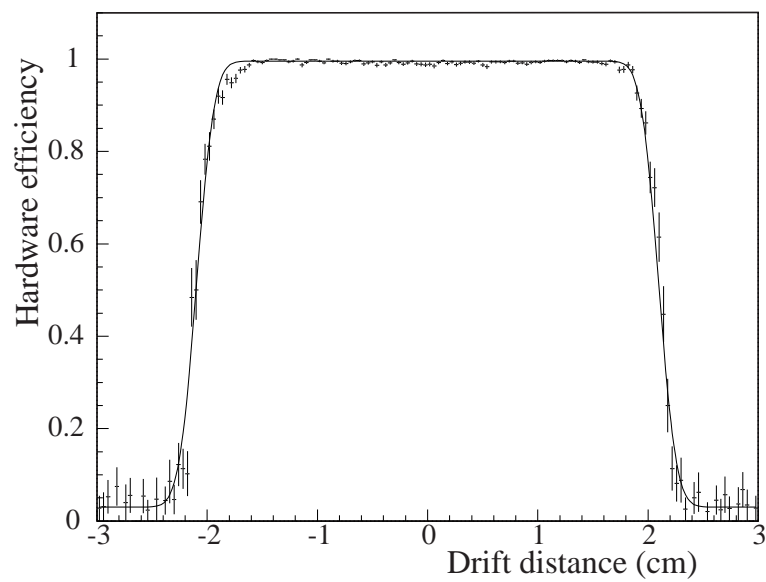Figure 2.10: Software efficiencies as function of the drift distance.

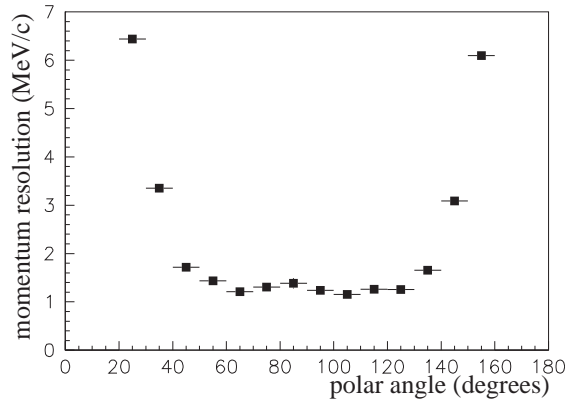Figure 2.11: Hardware efficiencies as function of the drift distance.

Figure 2.12: Momentum resolution as function of polar angle, using Bhabha events.

2.3.3   The electromagnetic calorimeter

The KLOE EMC [33], is a fine-sampling lead scintillanting-fiber calorimeter with photomultiplier read out Figure 2.13. The calorimeter has the following properties:

- a very good time resolution ($\simeq 100$ ps) and a good determination ($\simeq 1$ cm) of the photon conversion point, in order to allow the K^0 neutral decay vertex determination with an accuracy of few mm.
  The good position resolution together with the large radius ($\simeq 2$m) consent to have a very good resolution on the angle of the photon conversion point;

- an high hermeticity (98% of the solid angle), thanks to which multiphoton process has an acceptable geometrical efficiency and events with different number of photons can be separated correctly.
  The energy resolution is good ($5.7\%/\sqrt{E[\text{GeV}]}$) and the calorimeter is fully efficient over the range $20 \div 300$ MeV;

- it has also a very fast time response, that is used to trigger events at first stage.

A lead-scintillating fiber sampling calorimeter has been designed to fulfill these requirements. Scintillating fibers offer several advantages, in particular they provide good light transmission over the required distances, up to ~ 4.3 m. Superior timing accuracy is obtained because of single mode propagation. The calorimeter shape is adapted to the geometrical requirements obtaining good hermeticity. The cylindrical barrel consists of 24 modules of trapezoidal shape 4.3 m long, 23 cm thick and ~ 60 cm wide. Each endcap consists of 32 vertical modules $0.7 \div 3.9$ m long and 23 cm thick. The modular scheme of calorimeter can be seen in Figure 2.15.
The barrel covers a region between 40° and 310°, the endcaps covers the angles included between 9° and 46° and between 134° and 171° respectively. The cross-section of the modules is rectangular, of variable width.
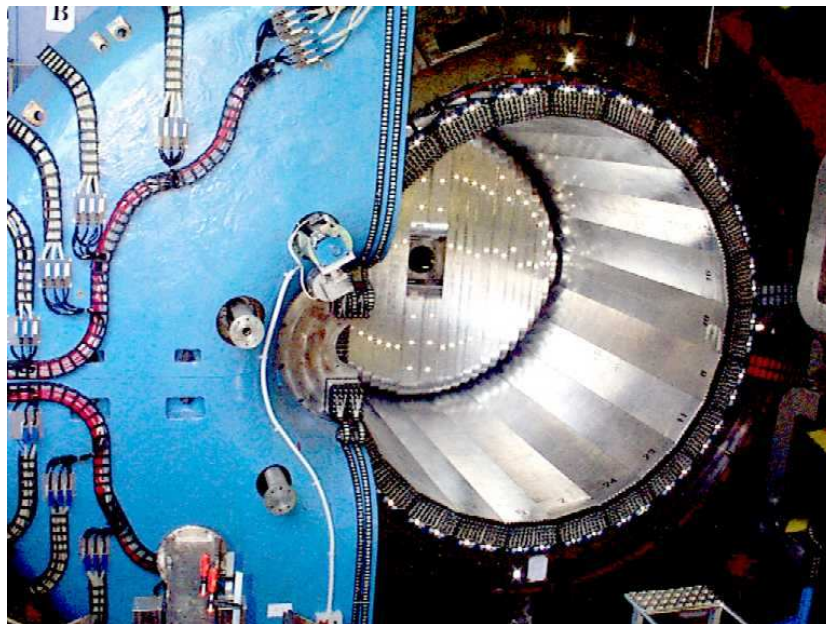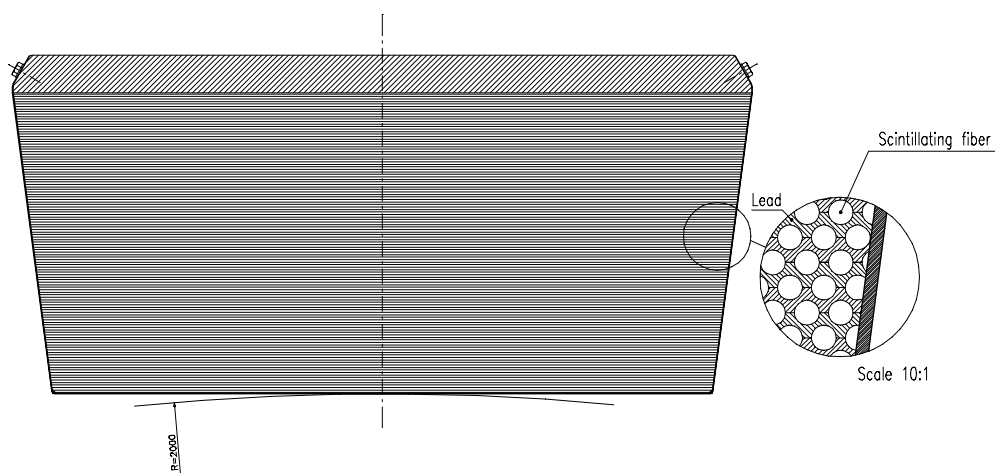
Figure 2.13: KLOE electromagnetic calorimeter.

Figure 2.14: Schematic view of the fiber-lead composite of each module of the electromagnetic calorimeter.
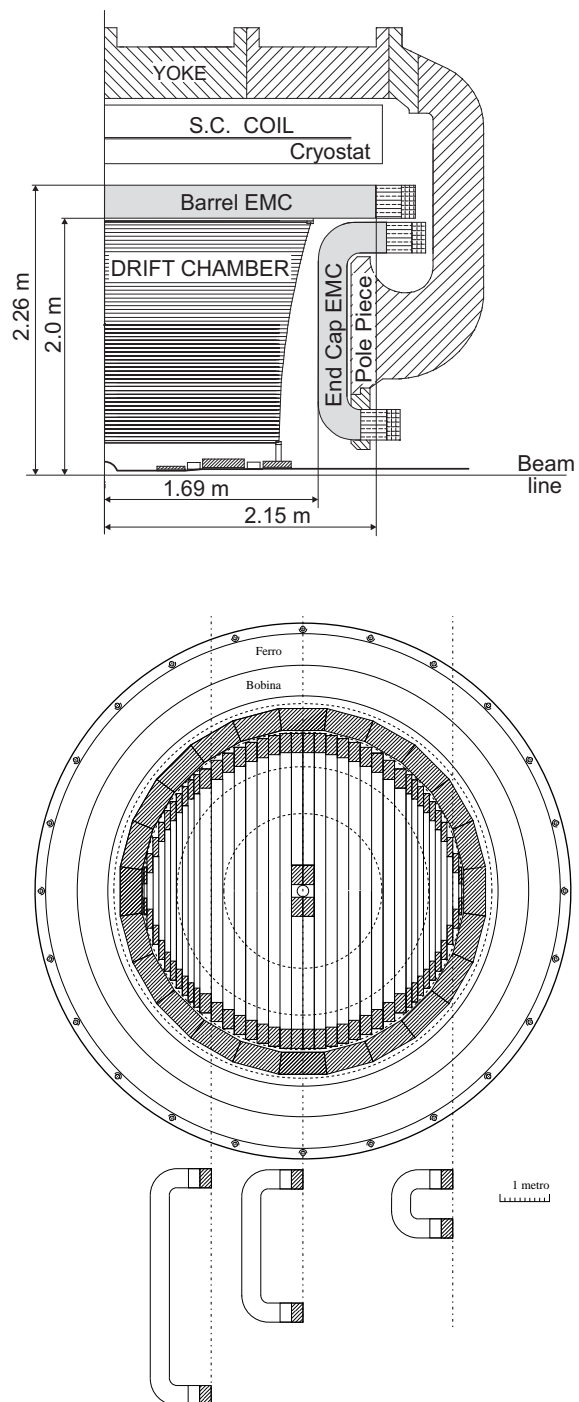
Figure 2.15: Top: transverse cross section of the KLOE detector, it is possible to see the shapes of the endcap EMC modules. Bottom: vertical cross section of the KLOE detector.

Modules are bent at the upper and lower ends to allow insertion into the barrel calorimeter and also to maintain the photo-tube axes parallel to the magnetic field. Due to the large overlap of barrel and endcaps, the KLOE calorimeter has no inactive gap at the interface between those components. The central endcap modules are vertically divided into two halves to allow the passage of the beam-pipe.

All modules are made of 200 grooved, 0.55 mm thick lead foils alternating with 200 layers of scintillating fibers with diameter 1 mm, glued in the grooves with a special epoxy, which is not harmful to the fiber plastic. Fibers are mostly orthogonal to the entering particles in order to avoid channeling. The ratio by volume of the different component material is: lead:fiber:epoxy = 42:48:10, the high scintillator content is necessary to maximize the number of collected photons per MeV released by the impinging particle, so to optimize the energy and time resolutions. The attenuation length of the fibers is $\lambda \geq 3$ m, while the average density is 5 g/cm^3, the radiation length is ~ 1.5 cm and the overall thickness of the calorimeter is ~ 15 radiation length.

Light is collected on both sides of each module, via light pipes which match almost square portions of the module end faces to 4880 photo-tubes. The read-out splits the calorimeter into five planes in depth, each deep 4.4 cm with the exception of the last which is 5.2 cm deep. In the transverse direction each plane is subdivided into cells 4.4 cm wide. The set made of 5 cells lined up, one for each transverse plane is named "column".

The read-out $r - \phi$ $(x - z)$ granularity for the EMC is finally $\sim 4.4 \times 4.4$ cm^2 slightly varying in size across the modules. This allows a very good spatial resolution.

The energy deposit in each cell is obtained from the charge measured at each side of the modules by the ADC's. The cell time is derived by time intervals measured at each side of the modules by the TDC's. The difference of the signal arrival times at both ends allows to reconstruct the coordinate along the fibers. Therefore the resolution on the z longitudinal coordinate depends on the statistics of photoelectrons: $\sigma_z \sim 9$ mm/$\sqrt{E[\text{GeV}]}$.

The energy resolution and the linearity of the energy response have been measured using photons from radiative Bhabha events and from $\phi \rightarrow \pi^+\pi^-\pi^0$ events. In both cases the photon energy E_γ is estimated by tracks momenta (reconstructed by the drift chamber) and it is compared with the measured cluster energy E_{CL}. The fractional resolution σ_E/E_γ and the relative deviation from linearity $(E_\gamma - E_{CL})/E_\gamma$, obtained from radiative Bhabha events are plotted in figure 2.16 as function of the photon energy. Linearity is better than 1% for $E_\gamma > 75$ MeV, while deviations from linearity at the $4 \div 5\%$ level are observed for low energies, probably due to the loss of shower fragments. The fit of the energy resolution to the function $a/\sqrt{E[\text{GeV}]} + b$ gives a negligible constant term, proving that the resolution is dominated by sampling fluctuations, and gives a stochastic term $a = 5.7\%$:

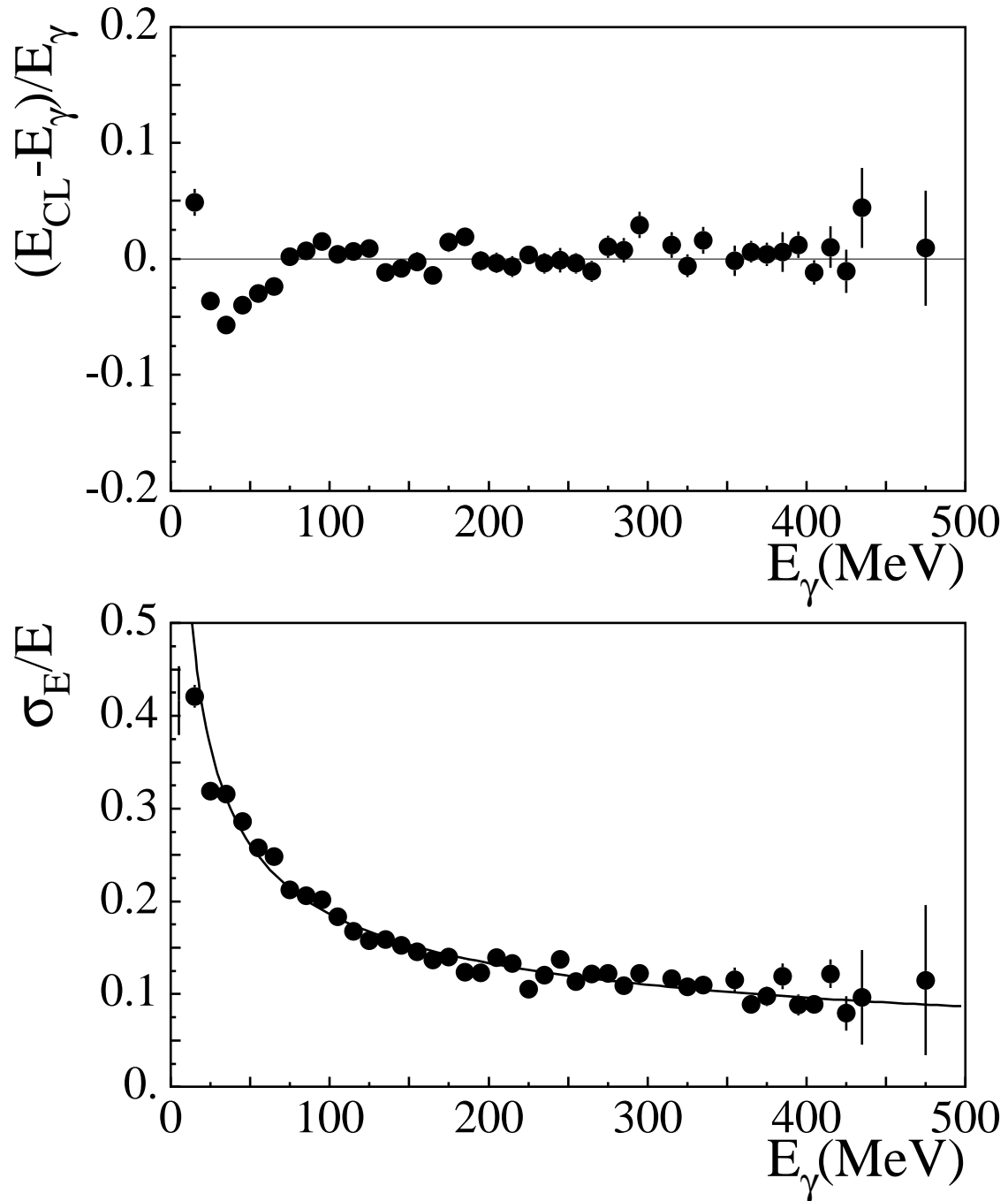$$\frac{\sigma_E}{E} = \frac{5.7\%}{\sqrt{E(\text{GeV})}} \tag{2.1}$$

Figure 2.16: Top: linearity of the calorimeter energy response as a function of the photon energy. Bottom: energy resolution of the calorimeter as a function of the photon energy. The two curves are evaluated with radiative Bhabha events.

Compatible results are obtained from $\phi \to \pi^+\pi^-\pi^0$.

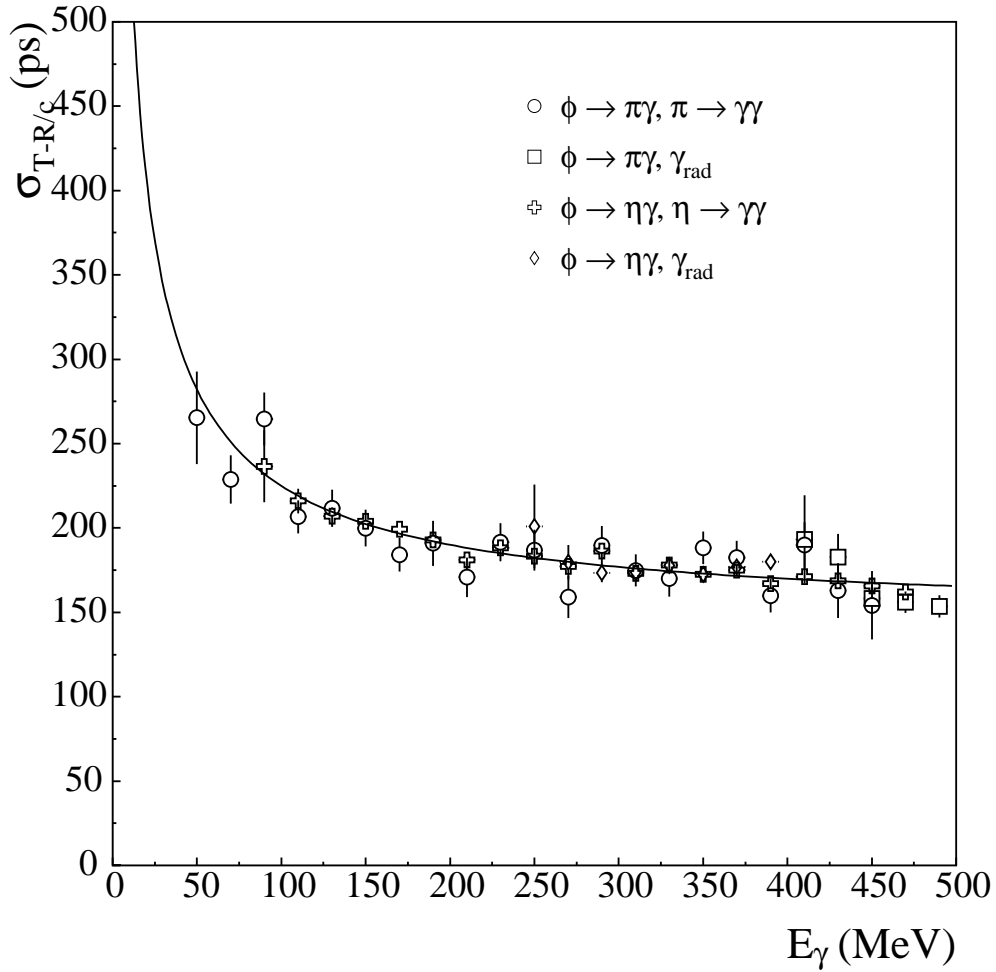The time resolution derived by the analysis of various radiative ϕ decays is shown in Figure 2.17.

Figure 2.17: Time resolution of the calorimeter as a function of the photon energy, for radiative ϕ decays.

Good agreement between the measurements for different channels is observed down to 100 MeV. The curve in the plot is the result of a fit:

$$\sigma_t = \frac{54 \text{ ps}}{\sqrt{E[\text{GeV}]}} \oplus 140 \text{ ps} \tag{2.2}$$

where the sampling fluctuation term is in agreement with test beam data [35] and the second term is a constant to be added in quadrature. The constant term is given by

the quadrature sum of two contributions: the intrinsic time spread due to the finite length of the luminous point in the beam direction, which contributes for ~ 125 ps, and the resolution of the synchronization with the DAΦNE radio–frequency, which contribute for ~ 50 ps.

Compatible results are obtained from $\phi \to \pi^+\pi^-\pi^0$ and from radiative Bhabha decays.

The photon detection efficiency is an important quantity for various analysis. Three data samples have been used to estimate it: radiative Bhabha events and $\phi \to \pi^+\pi^-\pi^0$ decays, which provide a source of photons coming from the interaction point, and $K_L \to \pi^+\pi^-\pi^0$ decays, in which the photons originate from a K_L decay vertex in the DC volume. The detection efficiency ε_γ, resulting from these three analysis, are shown as a function of the photon energy in Figure 2.18.
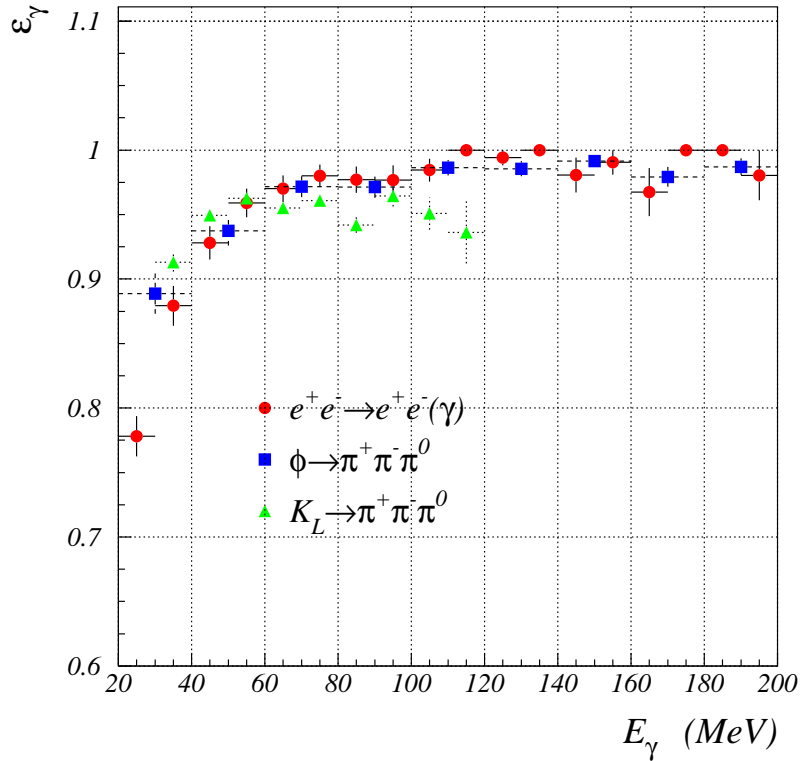
Figure 2.18: Photon detection efficiency using: $e^+e^-\gamma$ (Bhabha radiative), $\phi \to \pi^+\pi^-\pi^0$, $K_L \to \pi^+\pi^-\pi^0$.

A constant value of more than 98% is observed above 100 MeV, while a loss in efficiency is evident below 100 MeV.

2.3.4   The quadrupole calorimeters (QCAL)

In order to achieve the maximum possible luminosity, the last focusing quadru- poles are very close to the interaction point, inside the KLOE detector. The presence of this quadrupoles limits the geometrical acceptance for photons coming from K_L^0 decays encreasing by a factor 5 the probability to lose one single photon, then a sensitive detector covering the quadrupoles is certainly welcome.

Detector design must satisfy stringent weight and volume requirements to fit between the quadrupoles and the drift chamber inner wall. The adopted solution is a sampling calorimeter made of lead and scintillator tiles see Figure 2.19.

The calorimeter is divided in 16 radial section whose light is collected by wavelength shifting fibers. Each fiber curved and shared between two non adjacent sector allowing to place the PMs only on the side far from the interaction point and avoiding double hits on the same fiber.

Looking from the interaction point each radial sector has a conical part (50 cm long) followed by a cylindrical one (31 cm long). Each sector contains 16 lead planes (2 mm thick) and 15 scintillator layers (1 mm thick) for a total of ~ 5.5 radiation lengths. PMs are of mesh-dynode type to reduce the effect of magnetic field.[1] The signal coming out from each PMs is splitted in two: the first is shaped and sent to the ADC, the second is discriminated and sent to the TDC. Main request for the QCAL detector is the photon detection efficiency. This can be measured using cosmic rays selected by the drift chamber. The energy released by a cosmic MIP is equivalent to that of a 75 MeV photon.

The efficiency for the single sector is 98 %, but when both signal at the fiber ends are requested the efficiency drop down to 75 %. The hit coordinate along the fiber is determined by the difference in the arrival time at two ends from:

$$z = L - v\frac{t_2 - t_1}{2} \tag{2.3}$$

where L is half of the total fiber length and v is the light speed in the fiber. Photon detection efficiency has been evaluated using $K_L^0 \to \pi^0\pi^0\pi^0$ and $K_L^0 \to \pi^+\pi^-\pi^0$ samples and looking for a photon not detected by calorimeter that intersects the QCAL region. The result for a single photon efficiency is $92 \pm 4\%$.

Time resolution obtained with cosmic rays events is:

$$\sigma(t) = 0.9 \pm 0.2 \text{ ns} \tag{2.4}$$

corresponding to:

$$\sigma(t) = \frac{240 \text{ ns}}{\sqrt{E(\text{GeV})}} \tag{2.5}$$

Energy resolution is expected to be larger than 40% and indicates that QCAL detector can be used as photon counter but not a precise calorimeter.

---

[1]Nonetheless a gain reduction of $\sim 60\%$ has been observed once the PMs have been installed inside the KLOE magnetic field.

Pb layers (1.9 mm)

Scintillator tiles (1 mm)
and W LS fibers

R ext= 21.5 cm

R ext= 16.5 cm

PM 1

PM 2

90 cm

5.5 cm

R in = 11 cm

KLOE - QCAL

Al-mylar Sheet

Scintillator tiles

Lead Layers
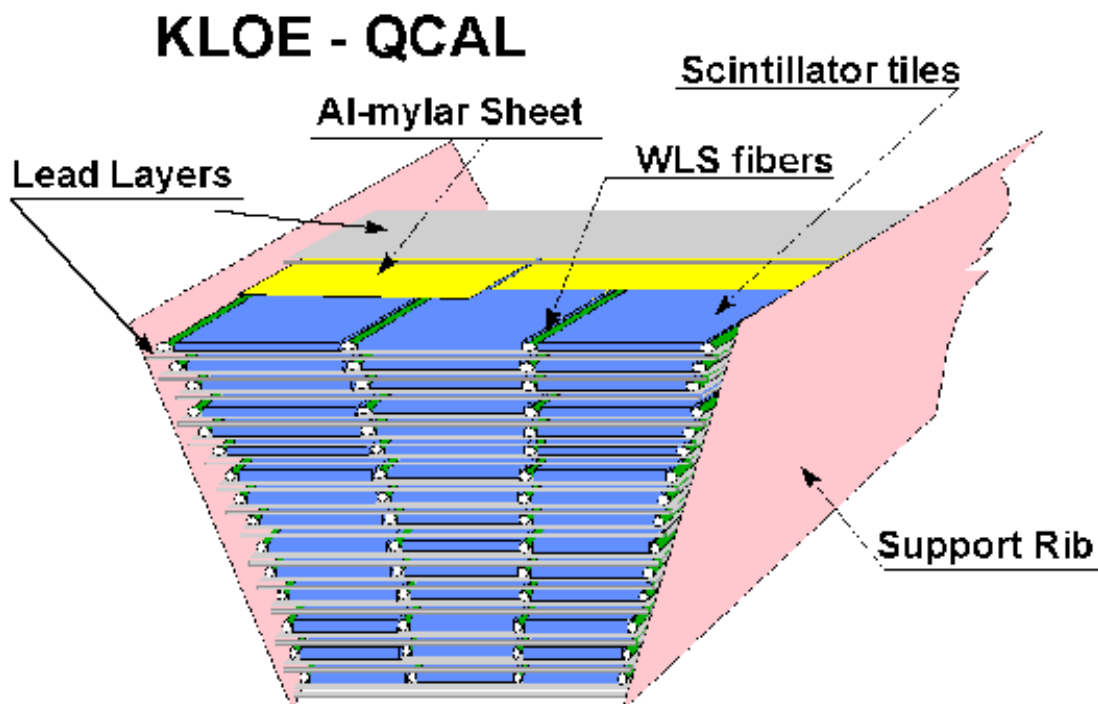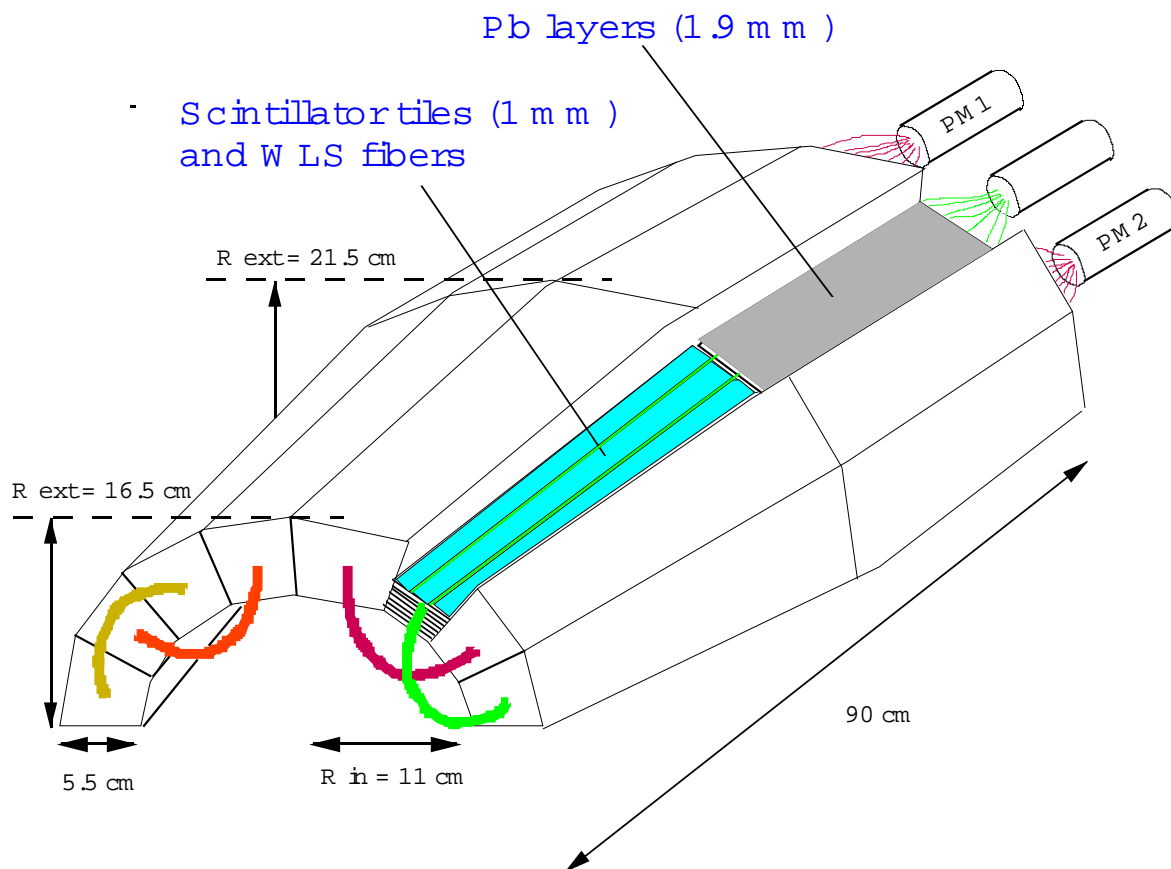
WLS fibers

Support Rib

Figure 2.19: Schematic view of a quadrupole calorimeter.

2.4 The trigger system

The main goal of the KLOE trigger system [47] is to:

- produce a trigger signal for all ϕ events;

- recognize Bhabha and cosmic-ray events and accept a downscaled sample for calibration purposes;

- reject the machine background.

There are two main sources of background.
One is due to Bhabha events at small angles, where electrons and positrons hit two focusing quadrupoles located very close to the IP and produce showers inside the detector.
The other source is due to particle losses from the DAΦNE beams. These off-momentum particles come from beam-gas interactions or Touschek scattering. The trigger is based on local energy deposit in calorimeter and multiplicity information from the drift chamber. It is composed by two levels (see Figure 2.20) in order to both produce an early trigger with good timing to start the Front End Electronic (FEE) operations and to use as much information as possible from the drift chamber. Specifically, after the arrival of a first level trigger, additional information is collected from the drift chamber, which is used, together with the calorimetric information, to confirm the former and to start the DAQ system. The calorimeter triggers on local energy deposits larger than a programmable threshold. Two thresholds are given for each EMC signal, the first at low energy ~ 50 MeV in order to trigger on low energy particles from ϕ decays entering the calorimeter (Low Energy Threshold, LET), and the second at high energy ~ 350 MeV in order to identify and reject (or accept as downscaled sample) Bhabha events (BhaBha Trigger, BBT).
The drift chamber triggers on the multiplicity of fired wires: each sense wire signal, after preamplification, is fed into the discriminator card where signals for the TDCs and the trigger are formed; for the trigger they are formed to a width of 250 ns, i.e. the coincidence width which optimizes both signal efficiency and background rejection, and produces a fast trigger signal.
The **first level** trigger algorithm can be summarized as follows:

- *ϕ trigger:* (2 calorimeter LET hits with Barrel-Barrel, Barrel-Endcap or Endcap-Endcap topology) OR (15 drift chamber hits within 250 ns).

- *Bhabha veto:* 2 calorimeter BBT sectors with Barrel-Barrel or Endcap-Endcap topology.

The level one trigger T1 sets a 2 μs long acknowledge signal, which vetoes other first level triggers and allows signals formation from the drift chamber cells.
Before being distributed to the calorimeter FEE, the first level trigger is synchronized with a resolution of 50 ps with the DAΦNE radiofrequency divided by 4 ($T = 10.8$

Figure 2.20:
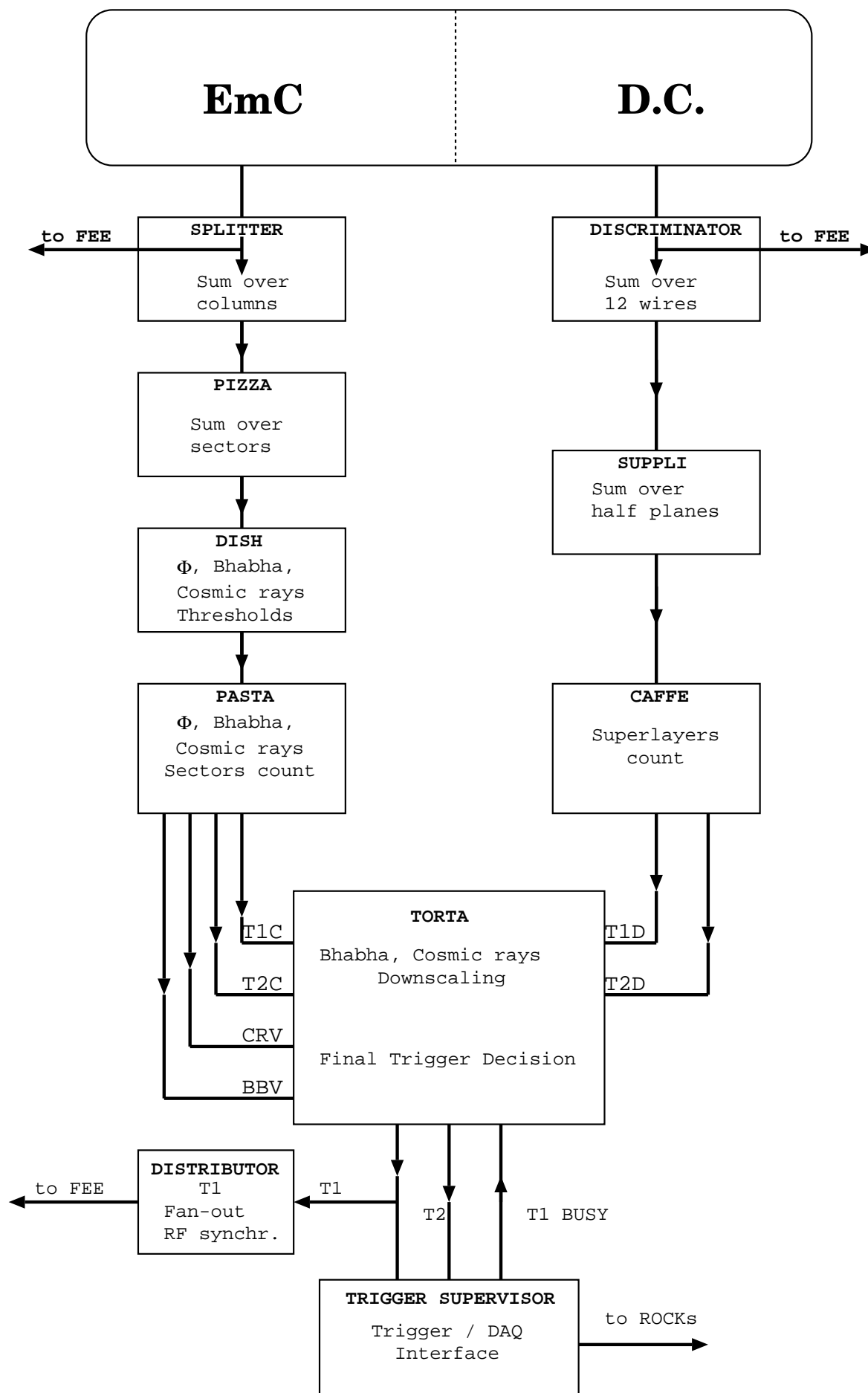
ns). Therefore the calorimeter TDCs measure the time with respect to a bunch crossing coming n periods after the collision that originated the event, where n has to be determined by the offline reconstruction of the event. This technique allows us to preserve the resolution on time measurement at the level of pico-second, which would be otherwise spoiled by the intrinsic jitter of the trigger signal formation.

At the end of the dead time the trigger system asks for a confirmation of the level 1 decision. The signal from these dedicated channels are treated in the same way as those used to define the ϕ or Bhabha calorimetric triggers but with threshold chosen to be equal to the average energy released in a cell by a minimum ionizing particle MIP ($40 \div 50$ MeV). Once two sectors are above threshold, the cosmic rays bit is activated and the event flagged. To avoid rejection of $\mu^+\mu^-$ events, which trigger easily the external planes of the calorimeter, a third level trigger (T3) has been developed. Each event detected as cosmic ray events by the second level trigger are flagged and not rejected, then these events pass through the T3 filter before being written on tape. The T3 filter performs a fast preliminary pattern recognition looking for tracks coming from the interaction point. If no track is coming from the IP the event is rejected. The level two trigger T2 gives the stop to chamber TDCs and starts the data acquisition.

The **second level** algorithm can be summarized in this way:

- ϕ *trigger:* (at least 1 calorimeter hit in the Barrel or 3 hit in the same Endcap) OR (40 drift chamber hits integrated during 850 ns after T1).

- *Cosmic flag:* 2 hits on the external plane of the calorimeter with Barrel-Barrel or Barrel-Endcap topology.

2.5 The data acquisition system

The KLOE data acquisition system [36] (DAQ) was designed to collect data from more than 23000 electronic channels (13000 DC and 10000 EmC channels) at a maximum rate of 50 Mbytes/s. A two level concentration scheme has been adopted, Figure 2.21.

In the first level *sub−events* are processed, where a sub-event is a piece of an event produced by a subset of the front end electronics (FEE). The FEE are housed in crates together with read-out controllers (ROCK's). The crates are organized in 10 chains.

A ROCK manager, the ROCKM, reads sub-events, associated to a trigger number, from a chain through a custom bus, the *C−bus*. The ROCKM's are housed in second level crates together with CPU's equipped with FDDI interfaces. The CPU's reads the data from the ROCKM's and send it to the CPU online farms. The addresses of the online farm processors is provided by a Data Flow Controller (DFC). The DFC

guarantees that all sub-events with the same trigger number are sent to the same CPU online farm. After arriving the online farm processor, the sub-events from different chains, associated to the same trigger number, are merged together to build a whole event, and are written in YBOS format into a circular buffer. Here the formatted events are read by the two processes: the *Recorder*, which writes events to disk, and on tapes; the *Spy-Daemon*, wich writes events in a spy buffer for online monitoring, eventsin a spy buffer for online monitoring, event display, and detector calibration.

These tasks are accomplished by numerous processes. Among these, the *Trgmon* process, reading information about trigger sectors, provides a fast monitor of quantities such as instantaneous luminosity, background level, and data rates. The *L3* process selects Bhabha, $\gamma\gamma$, and CR events used for detector online calibration and monitoring. Finally, the *Trkmon* process, calculates for each run the average ϕ momentum and position by using Bhabha events, and checks drift chamber wire efficiencies.

2.6   MonteCarlo: detector simulation and physics generators

The KLOE MonteCarlo program, GEANFI, is based on the GEANT 3.21 library [37] widely used in current high-energy and astroparticle physics experiments. GEANFI incorporates a detailed description of the KLOE apparatus, including:

- the new interaction region: the beam pipe, the low–beta quadrupoles, and the QCAL calorimeters;

- the drift chamber;

- the endcap and barrel calorimeters;

- the superconducting magnet and the return yoke structure

A set of specialized routines has been developed to simulate the response of each detector, starting from the basic quantities obtained from the GEANT particle-tracking and energy deposition routines. Moreover the simulation of $\frac{dE}{dX}$ measurement in drift chamber and the treatment of nuclear interactions/regeneration in drift chamber wall and beam pipe are inserted.

GEANFI contains the code to generate the physics of interest at DAΦNE. The cross section for the relevant processes in e^+e^- collisions at $\sqrt{s} = 1.02$ GeV are listed in Table 2.3.

A precise Bhabha-event is required for the measurement of the luminosity.
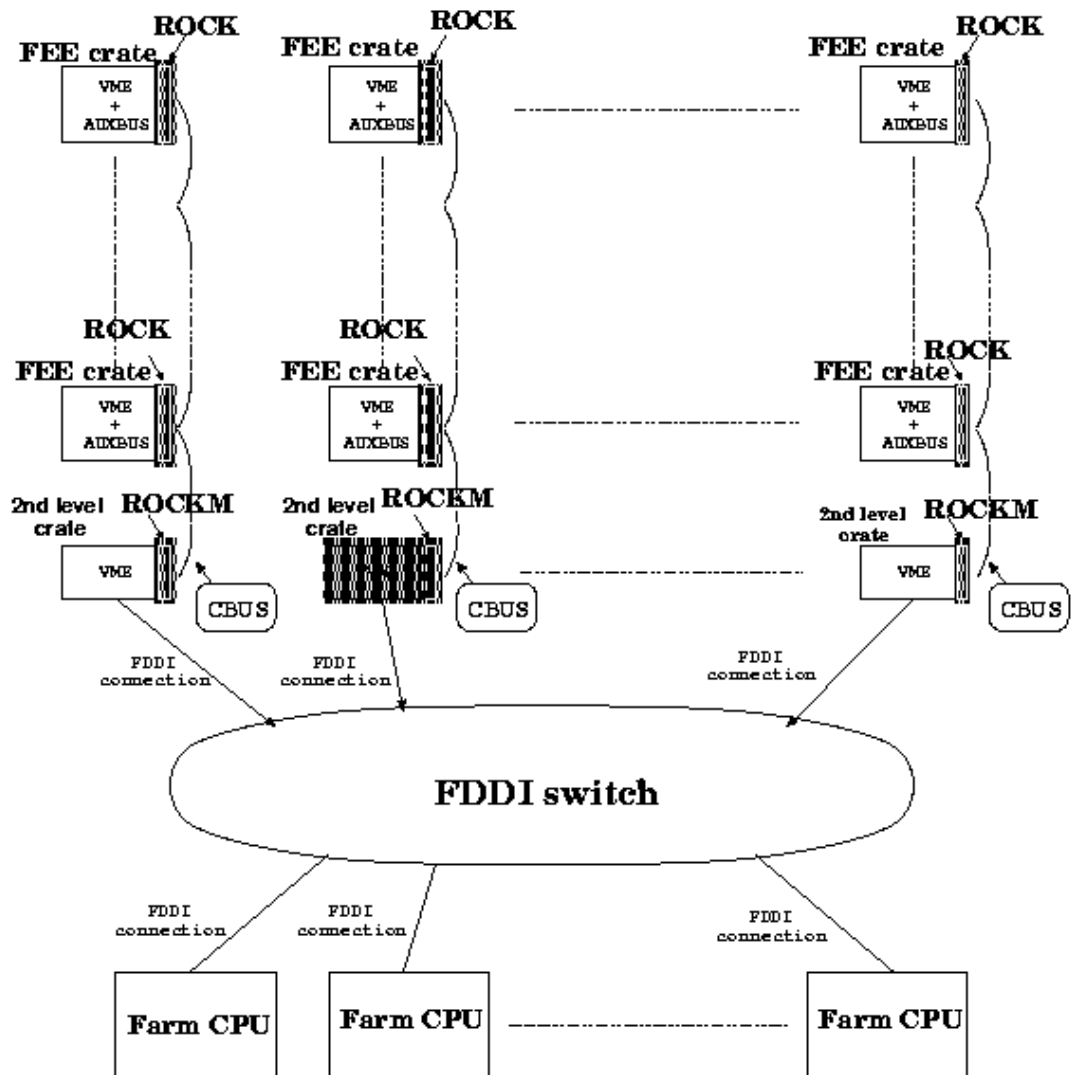
Figure 2.21: Scheme of the DAQ–system hardware.

Process	Polar Angle	$\sigma(\mu)$ b
$e^+e^- \rightarrow e^+e^-(\gamma)$	$20° < \theta < 160°$	6.2
$e^+e^- \rightarrow \mu^+\mu^-(\gamma)$	$20° < \theta < 160°$	0.085
$e^+e^- \rightarrow \pi^+\pi^-(\gamma)$	$20° < \theta < 160°$	0.080
$e^+e^- \rightarrow \gamma\gamma(\gamma)$	$20° < \theta < 160°$	0.30
$e^+e^- \rightarrow \omega\pi^0$		0.008
$e^+e^- \rightarrow \phi$		3.1

Table 2.3: Cross sections for several e^+e^- interaction processes at $\sqrt{s} = 1.02$ GeV. For the process $e^+e^- \rightarrow \phi$, the visible cross section is listed.

To reach an accuracy of a few per mill for the effective cross-section radiative corrections must be properly treated. BABAYAGA [39] generator [37, 38] has been interfaced with GEANFI. This generator is based on the application to QED of the parton-shower method originally developed for perturbative QCD calculations. The generator takes into account corrections due to initial-state radiation (ISR), final-state radiation (FSR), and ISR-FSR interference, and has an estimated accuracy of 0.5%. BABAYAGA can also be used to generate $e^+e^- \rightarrow \mu^+\mu^-$ and $e^+e^- \rightarrow \pi^+\pi^-$ events. The routines in the GEANT library simulate two and three body decays according to pure phase-space distributions. Only the main decay modes of muons, pions, kaons, and mesons are simulated. We have enriched the list of simulated particle-decay modes to include rare decays and refined the kinematic distributions of the secondaries to include the correlations expected from the matrix elements for the different decay processes.

The generator for ϕ events, BABAYAGA, selects the ϕ decay channel and declares the decay products to GEANT. Initial-state radiation and the beam-energy spread of the machine ($\Delta E_{beam}/E_{beam} = 0.05\%$) are taken into account event by event in the simulation of the decay kinematics.

All decays modes of the charged and neutral kaons meson are simulated.

Chapter 3

Data reconstruction and event classification

3.1 Data reconstruction

The reconstruction of raw data, which are written to mass storage by the DAQ system, starts with the translation, performed through the detector maps, of electronic addresses into geographical detector addresses: time and position of the DC hits and time, position and released energy of the EMC cells. These quantities are then processed in order to reconstruct the physical quantities of the events.

3.1.1 Clustering

The clustering algorithm for the KLOE Electromagnetic Calorimeter, has to reconstruct the energy, impact point and the arrival time of each photons that reach the calorimeter.
Let us call *cell* a calorimeter segment, which is defined as the smallest calorimeter physical channel viewed by two photo-multipliers in the plane transversal to the fibre direction. For each cell two time signals, $t^{A,B}$ and two amplitude signals $S^{A,B}$ are recorded from the photo-multipliers on the two side of the fibre. The longitudinal position of the energy deposit is derived from the time difference between the two ends of the fibre, $t^A - t^B$. Let us define some useful variables:

- the TDC calibration constants $c^{A,B}$, in $]textns/TDC$ counts;

- the average times measured in a dedicate run $T^{A,B}$;

- the fine corrections to the time offsets $t_0^{A,B}$;

- the cell length L (cm);

- the light velocity in the fibres v (cm/ns);

The particle arrival time t and its coordinate z along the fibre direction are obtained from these variables as:

$$t = \frac{t^A + t^B}{2} - \frac{t_0^A + t_0^B}{2} - \frac{L}{2v} \qquad (3.1)$$

$$z = \frac{v}{2}\left[t^A - t^B - (t_0^A - t_0^B)\right] \qquad (3.2)$$

with

$$t^{A,B} = c^{A,B} \times T^{A,B} \qquad (3.3)$$

The energy signal on each side of a cell i is defined as:

$$E_i^{A,B} = \frac{S_i^{A,B} - S_{0,i}^{A,B}}{S_{M,i}} \times k_E \qquad (3.4)$$

where S are the ADC counts, $S_{0,i}$ are the zero offsets of the amplitude scale, $S_{M,i}$ is the response for a minimum ionising particle crossing the calorimeter centre and k_E is a scale factor, that gives the energy scale in MeV. The energy of the cell is obtained as the average of the two sides weighted with a factor that takes into account the attenuation due to the light propagation along the fibre:

$$E_i^{cell} = \frac{E_i^A A_i^A + E_i^B A_i^B}{2} \qquad (3.5)$$

The *clustering algorithm* works to put together cells hit by the same particle: joining the adjacent cells to form pre-clusters and then these pre-clusters are joined or split using both time and position informations.

The cluster time is defined as the energy weighted average of the times of the cells belonging it:

$$t_{cl} = \frac{\Sigma_{cells} E_i t_i}{\Sigma_{cells} E_i} \qquad (3.6)$$

The same procedure is used for the three coordinates of the clusters:

$$x_{cl} = \frac{\Sigma_{cells} E_i x_i}{\Sigma_{cells} E_i} \qquad (3.7)$$

$$y_{cl} = \frac{\Sigma_{cells} E_i y_i}{\Sigma_{cells} E_i} \qquad (3.8)$$

$$z_{cl} = \frac{\Sigma_{cells} E_i z_i}{\Sigma_{cells} E_i} \qquad (3.9)$$

A significant systematic effect induced by the clustering is the production of spurious clusters from the splitting of a unique energy deposit in the calorimeter.

This effect is strongly dependent on the energy of the particle releasing its energy and on the position of the cluster in the EMC and affects the photon multiplicity observed by the detector in a given event. For this reason it has been studied on well-define photons samples such as those produced in $e^+e^- \to e^+e^-\gamma$ events and in ϕ radiative decays. The probability of having a cluster splitting is computed as a function of cluster energy and polar angle, and is finally used to unfold the true multiplicities from the observed ones.

After cluster reconstruction, an estimate of the reference time of the event (the absolute T^0) is given by assuming that the first cluster in time is due to a prompt photon coming from the origin; this photon must have at least 50 MeV and must lie farther than 60 cm from the collision axis. The hypothesis of the being a prompt cluster reasonably fits a large set of events (radiative ϕ decays, K_L with at least a γ or a π^0 produced, $e^+e^- \to e^+e^-\gamma$), but is inadequate to describe $K^{\pm}$ events: in the charged kaon case, after event classification, a new estimation of the $T0$ must be done. Once that the absolute $T0$ is determined, it is taken as reference for all the times of the event.

3.1.2   Tracking

The tracking and vertexing procedure [41, 42] are based on the algorithms developed for the ARGUS drift chamber [43], and are modified to take into account the stereo geometry of the KLOE drift chamber and to optimize the vertex-finding efficiency over all the detecting volume.

The chamber operates with a helium-based gas mixture to minimize the tracks multiple scattering.

Due to the large cell dimensions the drift velocity is not saturated and the cell response is not linear. Specific sets of space to time relations (s-t relations), which allow to reconstruct the distance of closest approach of the particle to the sense wire, are computed as function of the drift time. Due to the square shape of the drift cell and to the deformations induced on it by the stereo geometry, the s-t relations depend on the spatial coordinates of the cell and on the incidence direction of the track in the cell. This dependence has been parametrized according to two variables (defined as shown in Figure 3.1): the track incidence angle $\tilde{\phi}$ and the shape parameter β, which takes into account the peculiar geometry of the upper part of the cell. It has been seen [44] that 232 parameterizations accounting for cell type (small or big), track orientation, and cell shape, are a reasonable compromise which allows a good description of the s-t relations and a limited number of parameterizations.
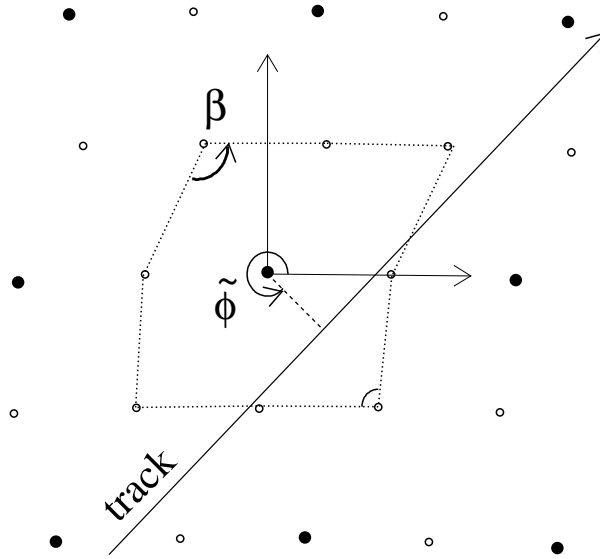
Figure 3.1: Definitions of the variables used in the s-t relations classification.

The s-t relations are parametrized in terms of a 5th order Chebychev polynomial, $d(C_k, t - T_0)$, and the C_k are 6×232 coefficients.

The track reconstruction procedure starts with the **pattern recognition**. The pattern recognition gives also a first estimate of the track parameters. Owing to the stereo geometry of the drift chamber, the hits are distributed on 2 nearby curves when projected onto the x–y plane. One of these curve is made up by the hits which fire wires with the positive stereo angle and the other one by the hits of wires with negative angle.

The pattern recognition first combines the hits on each view separately. The 2D candidates are then matched and merged to define the final track candidate. In merging the two views the z information is also extracted and an evaluation of the parameters describing the trajectory is made.

The **track fit** is a least-square fit of the track candidates whose initial parameters are taken from the pattern recognition results. The ultimate goal is to give the best estimation of the particle momenta and positions. The fit yields the parameters $\overrightarrow{q}$ which minimize the quadratic form:

$$\chi^2 = [\overrightarrow{d}_{meas} - \overrightarrow{d}_{\overrightarrow{q}}]^T W [\overrightarrow{d}_{meas} - \overrightarrow{d}_{\overrightarrow{q}}]$$

where $\overrightarrow{d}_{meas}$ are the measured drift distances, $\overrightarrow{d}_{\overrightarrow{q}}$ are the distances of the closest approach of the track to each wire and W is the inverse covariance matrix of the measured coordinates. The minimization is performed using an iterative procedure in which the track model is locally linearized. Energy loss and multiple scattering suffered by particles in crossing the drift chamber are also taken in account. The track fit procedure also contains some additional features designed to increase the

performance of the hit assignments using the parameters available at the track fit level, which are more refined than those available at pattern recognition level. These are:

- **Hit addition**: an ansatz is made to add hits that were not associated to any track candidate by the pattern recognition. Each hit is added or not on the basis of its contribution to the χ^2.

- **Hit rejection**: hits associated to tracks by the pattern recognition may be removed if their contribution to the χ^2 is too large.

- **Track joining**: tries to merge two candidate tracks which could have been produced by the same particle and split by the pattern recognition.

- **Track splitting**: it operates in the opposite way if the track joining, it tries to split single tracks corresponding to two different physical signals.

3.1.3   Vertexing

After reconstructing tracks, the vertex fit [42] aims to reconstruct the positions of the decay vertexes in the DC volume.
In order to reconstruct the ϕ decay vertex tracks are extrapolated toward the nominal interaction point, taking into account the energy losses on the DC inner walls. For the other vertexes an iterative procedure is used to obtain the point of closest approach for all tracks. Pairs of tracks are searched, whose trajectories show an acceptable crossing point, both in the x–y plane and along the z coordinate. A χ^2 minimization is applied in order to obtain the best possible estimate of the vertex position, and if such procedure converges, the vertex is kept.
Vertexes are classified according to the quality of the fit. At this level, even more than one vertex can belong to a given track. A merging procedure is performed to join 2-tracks vertexes together, so obtaining vertexes with 3 or more tracks (this is particularly relevant for the $K^{\pm} \to \pi^{\pm}\pi^{+}\pi^{-}$ decay). An hypothesis test which compares the 4-tracks verteces versus the 2-tracks verteces is done. On the bases of the χ^2 the two hypotheses are taped.

3.2   The background rejection filter: FILFO

The background-rejection algorithm is based on calorimeter clustering and DC hit counting, so that background events can be eliminated before DC reconstruction, which is the most CPU-intensive section of our reconstruction program. The main FILFO features are the downscaling of Bhabha and cosmic events, and machine background rejection.
For the identification of background events, cuts are applied on the number of clusters; the number of DC hits; the total energy in the calorimeter; the average polar angle, position, and depth of the (two) most energetic cluster(s); and the ratio between the number of hits in the innermost DC layers and the total number of DC hits. These cuts have been studied to minimize losses for physics channels. Additionally, a simple cut on anomalously large energy deposits in any calorimeter region is included to reject rare machine background topologies due to sporadic beam-loss events.

3.3   Event Classification: EVCL

 Events surviving the rejection filters and reconstructed by means of drift chamber information are finally classified into distinct categories (data streams) by the event-selection algorithms, according to the different hypotheses for the final state. Selection algorithms must correctly separate the various ϕ decay channels with the highest possible efficiency and minimize the contaminations from the other streams. In order to avoid correlations, the same event can be tagged by more than one algorithm and saved in different data streams. Moreover, biases are avoided by adopting rather loose and simple selection criteria. This also allows to reduce the CPU time needed for the event classification to a very small fraction with respect to the complete data reconstruction chain. The main streams defined in the event classification are, see Figure 3.2:

- $\phi \to K^+ K^-$ (KPM);

- $\phi \to K^0_S K^0_L$ (KLS);

- $\phi \to \rho\pi, \pi^+\pi^-\pi^0$ (RPI);

- ϕ radiative decays (RAD);

- Bhabha and cosmic events useful for detector calibration (CLB). Also $e^+e^- \to \mu^+\mu^-$ and $e^+e^- \to \pi^+\pi^-$ events are collected within this sample;

- All events not identified by any of the EvCl algorithms (UFO);
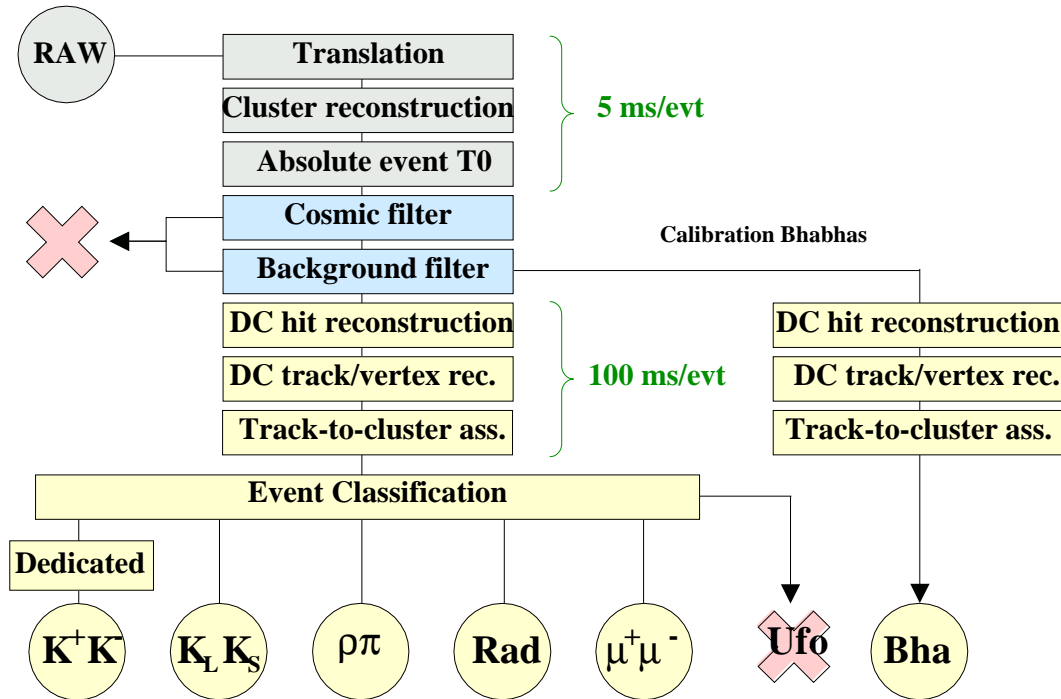
Figure 3.2: Logic scheme of the KLOE offline reconstruction.

- Bhabha scattering.

To save space on tape, only a little part of UFO events are kept, since a sizable amount of such events are unidentified Φ decays (for instance K^+K^- events in which both kaons have decayed in the interaction region without reaching the tracking volume) or machine background events.

Chapter 4

Selection of charged kaon events

$\phi \to K^+ K^-$ constitutes the most frequent decay mode of the ϕ meson, since the branching ratio for this channel is 49.2% [26]. In the ϕ rest frame, the two charged kaons have opposite momenta of 127 MeV , but due to the beam crossing angle the ϕ is produced with a momentum of $\sim 13\ MeV$. Then in the laboratory frame the kaon momentum ranges between $\sim 120\ MeV$and 135 MeV (see table 2.2).

The average value of the radius of curvature in the KLOE magnetic field ($\sim 0.52\ T$) for charged kaons having $p_z = 0$ is 81 cm; considering also the z component of its momentum, it turns out that a charged kaon has to travel in average $\sim 35\ cm$ from the interaction point before reaching the drift chamber volume. Given their velocity $\beta \simeq 0.25$ and their mean life $\tau = 1.2384 \cdot 10^{-8} s$ [26], charged kaons have decay length $\beta \gamma c \tau \simeq 95\ cm$, so that the probability for charged kaons to reach the DC volume and release a sufficient number of hits to determine a reconstructible track does not exceed 70%. Moreover, a particle coming from the interaction region, before entering the chamber, has to pass through the beam pipe, (see section 2.3.1) and through the drift chamber inner wall (see section 2.3.2), loosing on average 25 MeV, with a corresponding shortening of the decay length to about 75 cm.

4.1   The KPM stream selection algorithms

Five selection algorithms have been developed for the identification of $\phi \to K^+ K^-$ events and they constitute the official procedure of the Event Classification program for the KPM stream.

At the beginning of the data taking, during the machine tuning, till year 2000, only the first three algorithms were applied. Later two more algorithms more efficient and with higher cleaning capability have been developed.

1. *Algo1*, based on the existence of a candidate $\phi \to K^+ K^-$ vertex in the interaction region.

2. *Algo2*, looking for events with both K^+ and K^- tracks reconstructed without the ϕ vertex.

3. *Algo3*, trying to identify a charged kaon by requiring specific cuts on a single fitted track.

4. *TOPO*, exploiting the typical geometrical configuration of a K^+K^- event.

5. *TAG*, founded on the kinematic reconstruction and identification of a tagging $K^\pm$ two-body decay.

The first three algorithms are applied in cascade, according to the diagram shown in 4.1. Even if they have been replaced by the two newest algorithms we report them here for completeness purposes. Each algorithm analyzes the events by means of
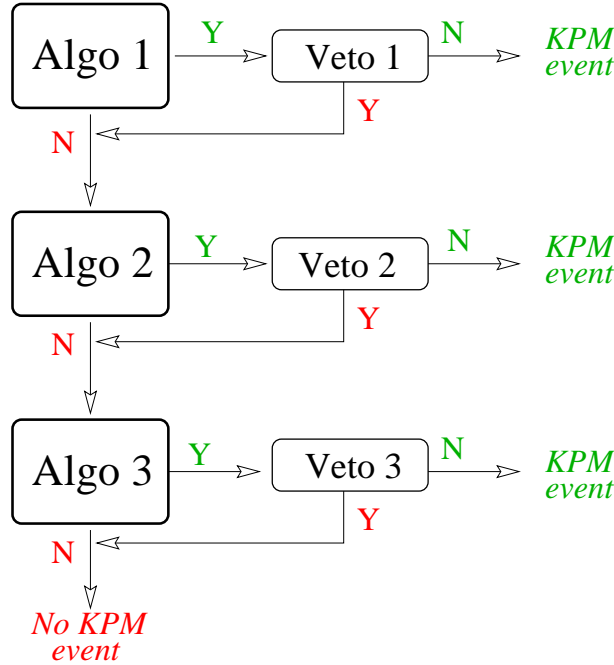
Figure 4.1: Logic scheme applied for the Algo1, Algo2 and Algo3 algorithms in the Event Classification program.

suitable selection criteria and a corresponding veto tests them against the background hypothesis: if such conditions are fulfilled, the events are definitively kept and no further requirements are imposed, otherwise the events are left to the analysis of the next algorithm(s). The definitions of the selection criteria applied in the first three algorithms are given in the following.

In the **Algo1** procedure vertexes with 2 tracks and total zero charge are required in the fiducial volume defined by:

- $r_V = \sqrt{x_V^2 + y_V^2} < 50\ cm$;

- $|z_V| < 40\ cm$;

in addition, the two tracks momenta $\overrightarrow{p}_1$ and $\overrightarrow{p}_2$ must be such that:

- $180 < |\overrightarrow{p}_1| + |\overrightarrow{p}_2| < 235 \ MeV$;

- $-20 < \overrightarrow{p}_{1x} + \overrightarrow{p}_{2x} < 40 \ MeV$;

- $|\overrightarrow{p}_{1y} + \overrightarrow{p}_{2y}| < 30 \ MeV$;

- $|\overrightarrow{p}_{1z} + \overrightarrow{p}_{2z}| < 20 \ MeV$.

Veto1 reject events for which any of the following requirement is satisfied.
Veto logic: (**1**.and.**2**).or.**3**.or.**4**:

1. $\theta_{K^+} < 0.60 \ rad$ (track produced at small polar angle);

2. $\theta_{K^-} < 0.60 \ rad$ (track produced at small polar angle);

3. $|r_{1PCA} + r_{2PCA}| \geq 16 \ cm$ where $r_{iPCA} = \sqrt{x_{iPCA}^2 + y_{1PCA}^2}$;

4. $|z_{1PCA} + z_{2PCA}| \geq 16 \ cm$;

and where x_{iPCA}, y_{iPCA}, z_{iPCA} and are coordinates of the Point of Closest Approach of the kaon track to the IP. The **Algo2** procedure asks for two tracks whose innermost (outermost) DC layer hit is < 20 (< 35), corresponding to $72.5 \ cm$ ($117.5 \ cm$) in the $x - y$ plane. The distance between the last hits of the two tracks has to be at least $88 \ cm$, the distance between the centers of the two helicoidal trajectories in the $x - y$ plane has not to exceed $25 \ cm$. Subsequently, the following cuts are required:

- $70 < |\overrightarrow{p}_1| < 170 \ MeV$;

- $|z_{1PCA}| < 70 \ cm$;

- $|r_{1PCA}| < 15 \ cm$;

- $50 < |\overrightarrow{p}_2| < 200 \ MeV$;

- $|z_{2PCA}| < 100 \ cm$;

- $|r_{2PCA}| < 25 \ cm$;

- $145 < |\overrightarrow{p}_1 + \overrightarrow{p}_2| < 260 \ MeV$;

- $|z_{1PCA} - z_{2PCA}| < 100 \ cm$;

- $|r_{1PCA} + r_{2PCA}| < 16 \ cm$.

The definition of **Veto2** coincides with Veto1.
In the **Algo3** procedure a single track is searched with innermost (outermost) DC layer hit < 10 (< 35), which corresponds to $48.5 \ cm$ ($117.5 \ cm$) in the $x - y$plane. Subsequently, the following cuts are required:

- track length $< 150\ cm$;

- $85 < |\overrightarrow{p}| < 120\ MeV$;

- $r_{PCA} < 10\ cm$;

- $|z_{PCA}| < 20\ cm$.

In order **Veto3** to be satisfied, at least one of the logical conditions is required.
Veto logic: **1**.or.**2**.or.**3**.or.**4**:

1. $|z_{PCA}| > 5cm$;

2. $|r_{PCA}| > 5cm$;

3. $|\overrightarrow{p}| < 80\ MeV$;

4. $|\theta K| < 0.7\ rad$.

The efficiency of the Algo1-Algo2-Algo3 cascade has been evaluated on Monte Carlo and is about 26%.

4.1.1   The new algorithms

A very high background rate in the KPM stream and a strong correlation in efficiency and systematic evaluation has been observed, since the starting of the KLOE data taking in 1999, when only these three algorithms were implemented in the Event Classification program. A typical background was due to pion photoproduction on the beam-pipe, see figure 4.2 and figure 4.3
Thus two more algorithms called **TOPO** and **TAG** have been developed in order to reduce the presence of background in the finally streamed data sample and to provide an estimate of the systematics induced by the first three algorithms. Their definitions are given below.
The old selection (the Algo-cascade) and the new algorithms have been "OR-ed" for 2001 and 2002 data.
The TOPO algorithm initially requires two tracks of opposite charge in the event which satisfy the following selection cuts:

- $|z_{PCA}| < 15cm$;

- $|r_{PCA}| < 15cm$;

- $70 < |\overrightarrow{p}_{PCA}| < 130\ MeV$;

- last hit in a fiducial volume obtained by rotating around the beam axis the isosceles trapezium having parallel sides, $250\ cm$ and $270\ cm$ long, whose distances from the z axis are $40\ cm$ and $150\ cm$ respectively.
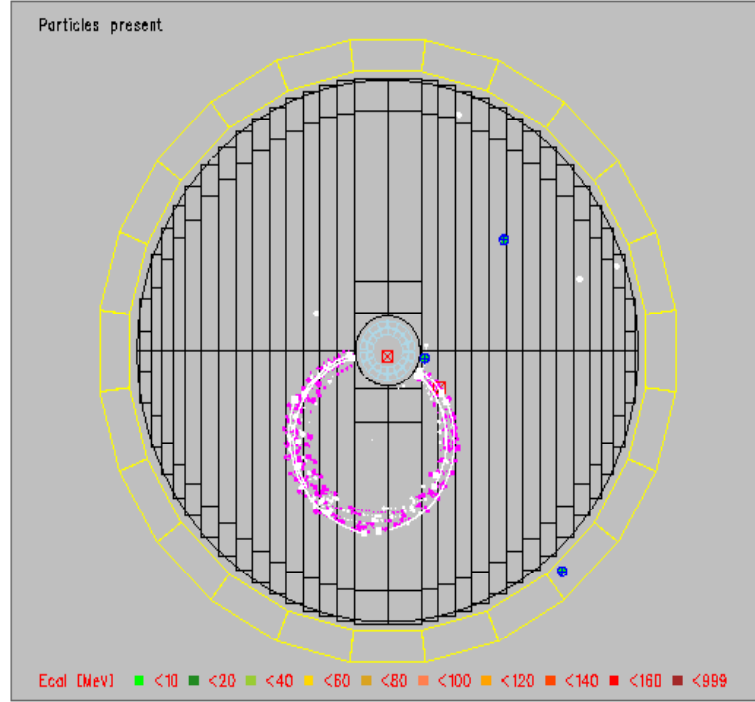
Figure 4.2: Reconstruction of a pion photoproduction event.

The angle ϕ_{em} between the emission line of the two kaons and the horizontal axis is then considered. The two momenta $\overrightarrow{p}_1$ and $\overrightarrow{p}_2$ have to satisfy these two conditions simultaneously:

- $(176 < |\overrightarrow{p}_1| + |\overrightarrow{p}_2| < 220 \ MeV)$ .OR. $(||\overrightarrow{p}_1| - |\overrightarrow{p}_2|| > 8 \ MeV)$;

- $||\overrightarrow{p}_1| - |\overrightarrow{p}_2|| > 25 \cdot (cos(\phi_{em}) - 0.6)$.

While the first condition exploits the correlation between the momenta of the two candidate tracks, the second condition uses the information of the boost of the ϕ meson.

The efficiency of the TOPO algorithm has been evaluated on Monte Carlo and is about 9%.

4.1.2 The TAG algorithm

The TAG algorithm tries to identify a two-body kaon decay $K \to \mu\nu$ or $K \to \pi\pi^0$, which are about 85% of charged kaon decays. It requires two tracks connected to the same vertex. First is required a track (kaon candidate) which has the point of closest approach to the IP smaller than $d_0 = 10 \ cm$ ($z_0 = 20 \ cm$) along the radial (longitudinal) axis. The radial distance between the kaon candidate decay vertex and the beam axis has to be $40 < R_V < 150 \ cm$. The kaon candidate must also have
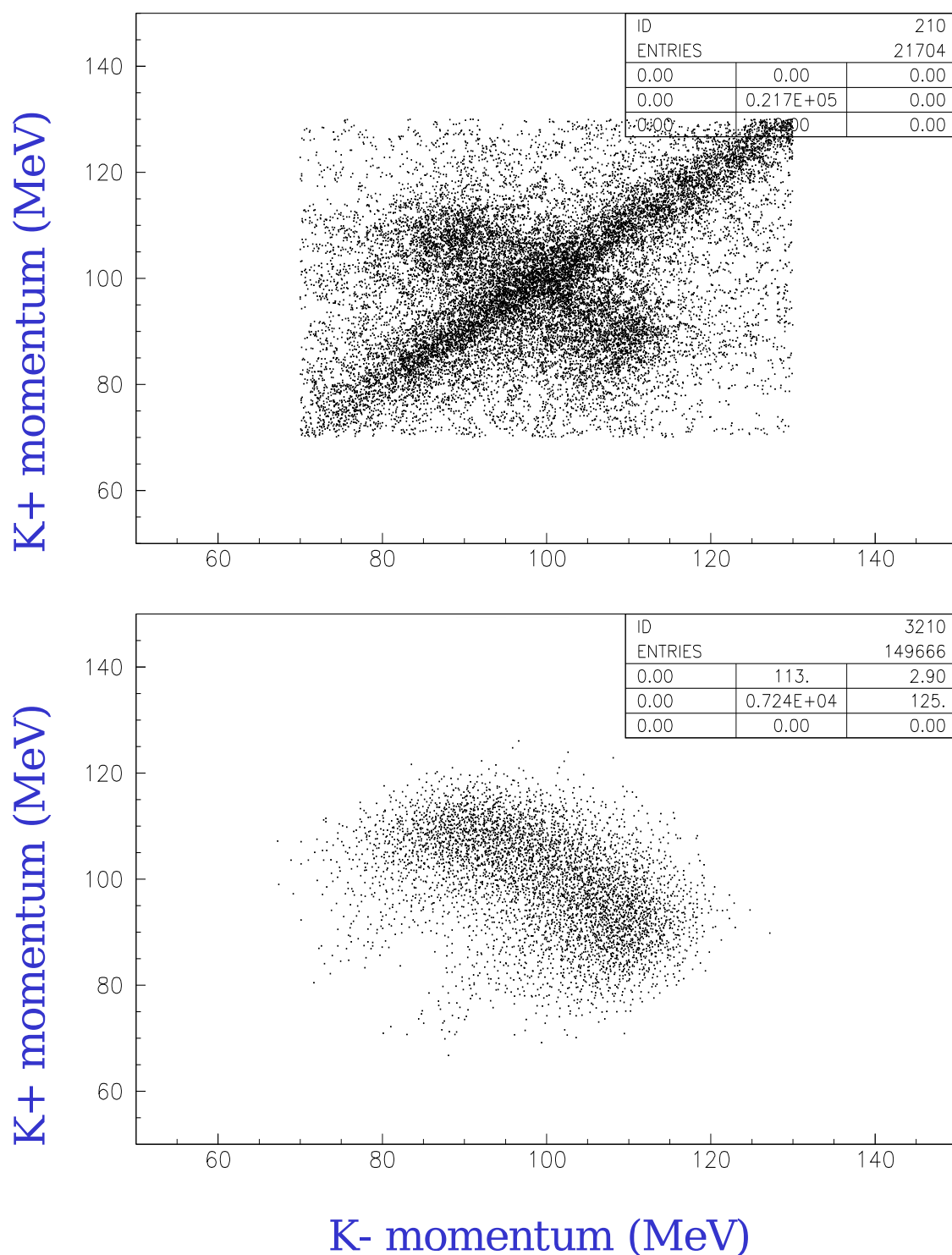
Figure 4.3: Momentum of K^+ versus the momentum of K^- for data (above) and Monte Carlo simulation (below). It possible to see a large amount of background due to pions photoproduced on the beam-pipe, which are characterized by the linear relation between the momenta of the two "kaon" candidate.

$70 < |\overrightarrow{p}| < 130$ cm. Once the kaon candidate has been identified, the candidate secondary track must have the same charge of the kaon and momentum in the laboratory ranging from 120 to 320 MeV and momentum in the kaon rest frame, using the $\pi^{\pm}$ mass hypothesis, ranging from 180 to 270 MeV.

Let's see how the tag algorithm acts on the event selection. First consider the distribution of d_0, z_0 and candidate kaon momentum before any cut (see figure 4.4). It is possible to see a big discrepancy between data and Monte Carlo especially in the distribution of the candidate kaon momentum mainly due to pion photoproduced contamination. Just applying the kaon preselection a large amount of these background events are discarded (see figure 4.5).

Then consider the distribution of the variables involved in the kaon decay: distance of the vertex from the beam axis R_V, momentum difference at the decay vertex Δp between the kaon and the secondary produced in the decay, momentum of the secondary in the kaon rest frame. Begin considering the first row of figure 4.6 which represents the radial distance of the kaon vertex corrected for the charge ($d_0 \equiv R_V$ in the figure; $R_V > 0$ if the kaon and the secondary have the same charge, otherwise $R_V < 0$). It is possible to see that there is a large amount of vertex at the interaction point which come from ϕ decay and pion photoproduction, since the charge of the particles involved in the vertexes is different. In the middle row is possible to see the distribution of Δp; the peak at zero corresponds to fake kaon decay vertexes which come from kaon broken tracks and the peak at 200 MeV corresponds to a secondary reconstructed with the wrong direction: the secondary charge is wrong and so the first hit is reconstructed as the last hit and viceversa. In the last raw is possible to see the presence of three body kaon decays (around 150 MeV) and of kaon broken tracks (near 50 MeV). It is possible to see how suitable cuts clean the data sample; see figure 4.7 where the following cut have been applied:

- 40 $cm < R_V < 150$ cm;

- 120 $MeV < |\Delta p| = |\overrightarrow{p}_K - \overrightarrow{p}_{sec}| < 320$ MeV.

For comparison with figure 4.3 we report in figure 4.8 the plot of the momentum of the K^+ versus the momentum of the K^- for double tagged events: the pollution due to pion photoproduction has disappeared.

The most important feature of the Tag algorithm is that works using the informations from only one of the two hemisphere of the event (K^+ or K^-). Since at DAΦNE kaons are always produced in pairs, the detection of $K^{\pm}$ without using the information from the second kaon $K^{\mp}$ allows us to consider the tag events as reference normalization and the kaons on the other hemisphere can be considered as a pure $K^{\mp}$ beam. Then it allows the measurement of absolute branching ratios.

The efficiency of the TAG algorithm has been evaluated on Monte Carlo and is about 20%.
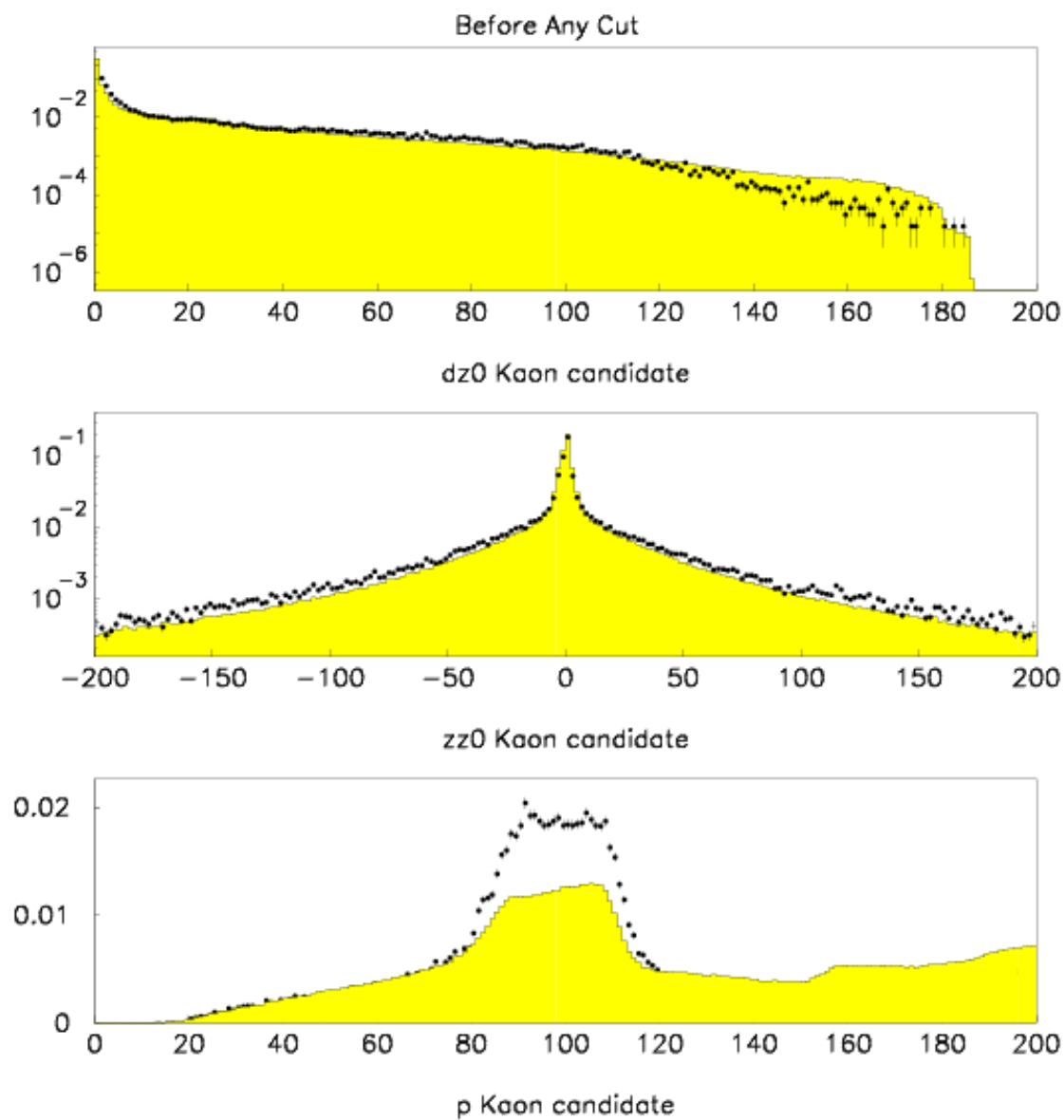
Figure 4.4: Distribution of d_0 (above) and z_0 (in the middle) for the kaon candidate, before any cut. Below is shown the kaon candidate momentum. Dots represent data and the yellow shape represents Monte Carlo.
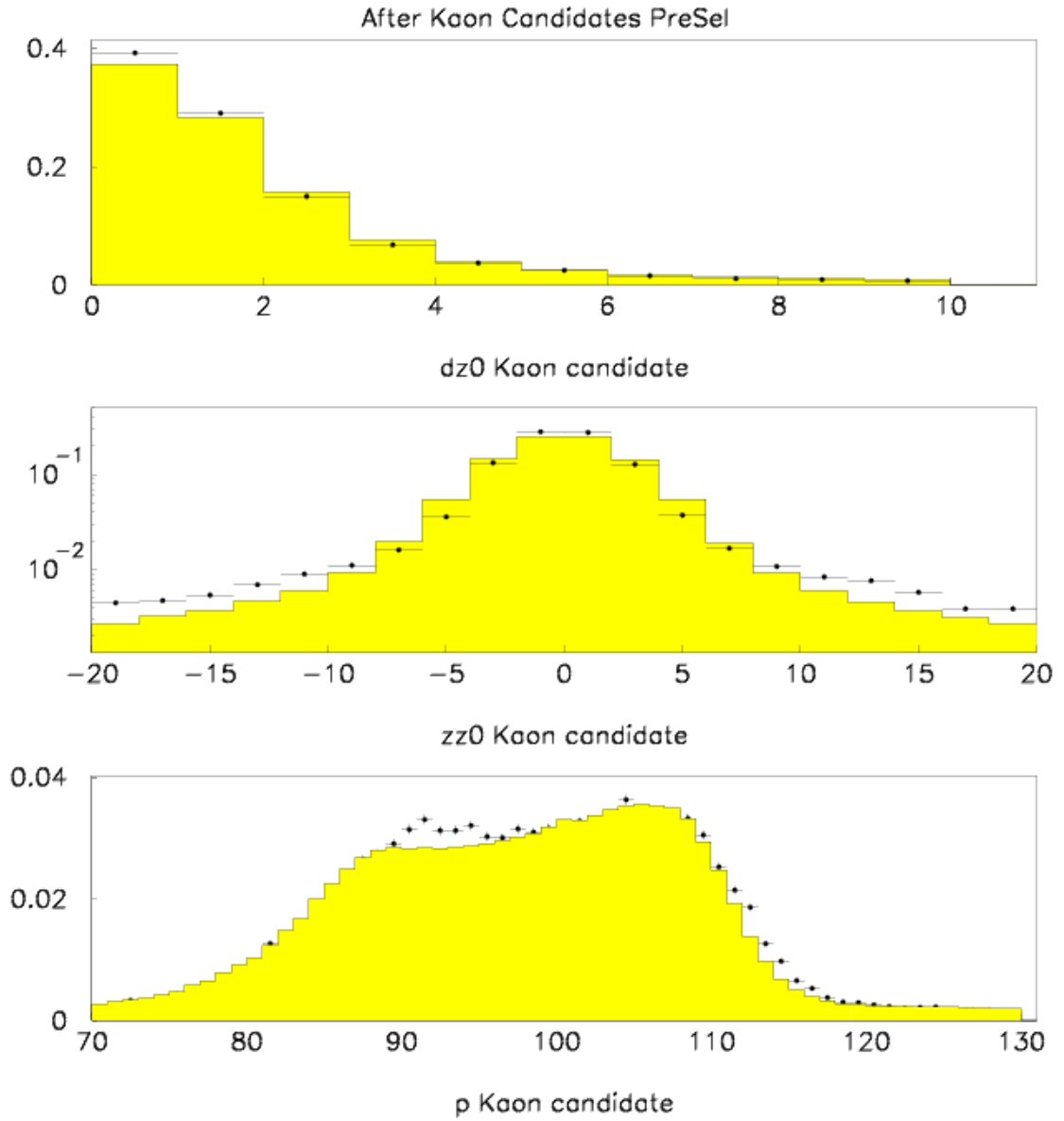
Figure 4.5: Distribution of d_0 (above) and z_0 (in the middle) for the kaon candidate, after kaon preselection. Below is shown the kaon candidate momentum. Dots represent data and the yellow shape represents Monte Carlo.
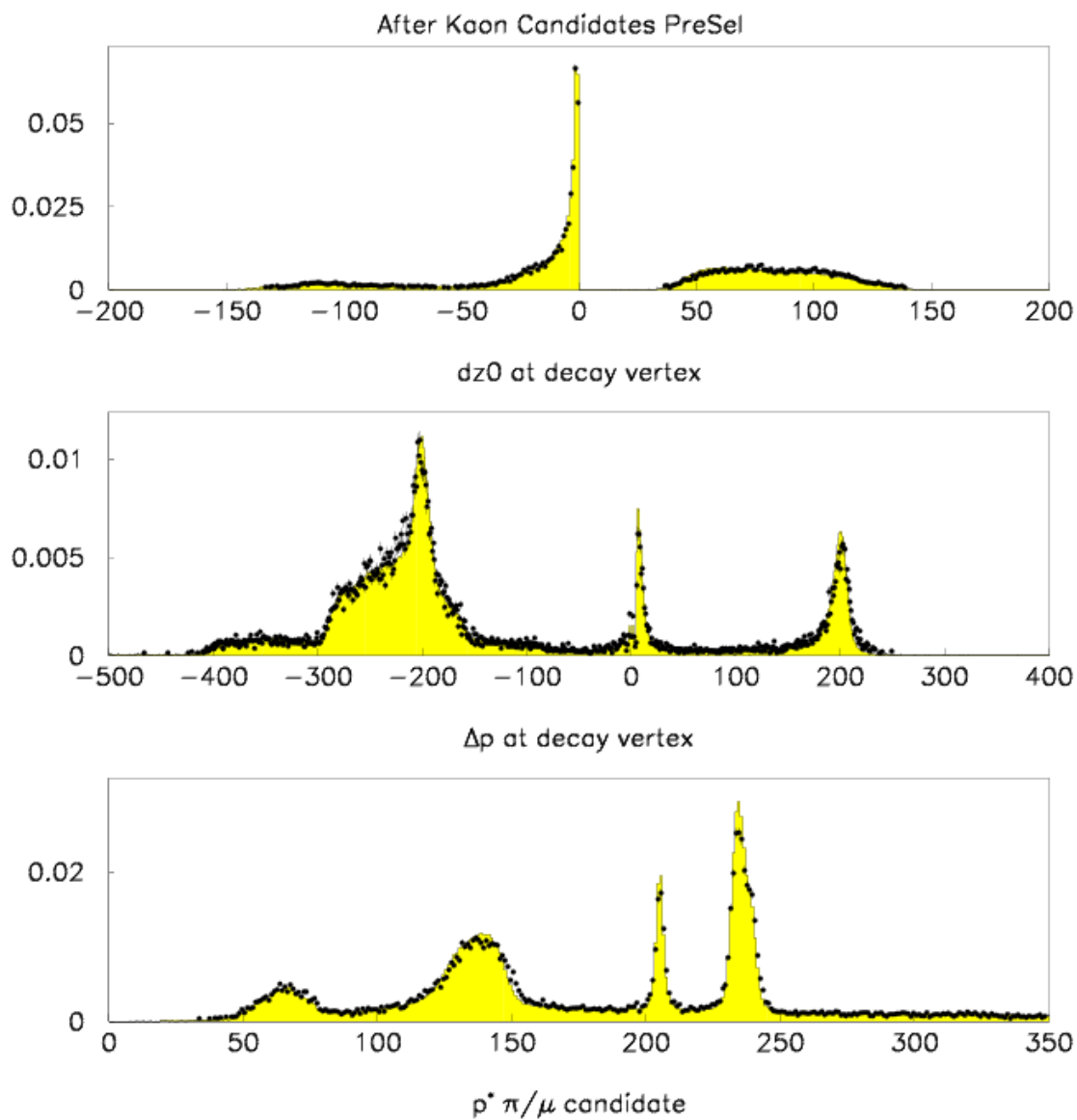
Figure 4.6: Distribution of $d_0 \equiv R_V$ (above), Δp (in the middle) and p^* (below) before any cut. Dots represent data and the yellow histogram represents Monte Carlo.
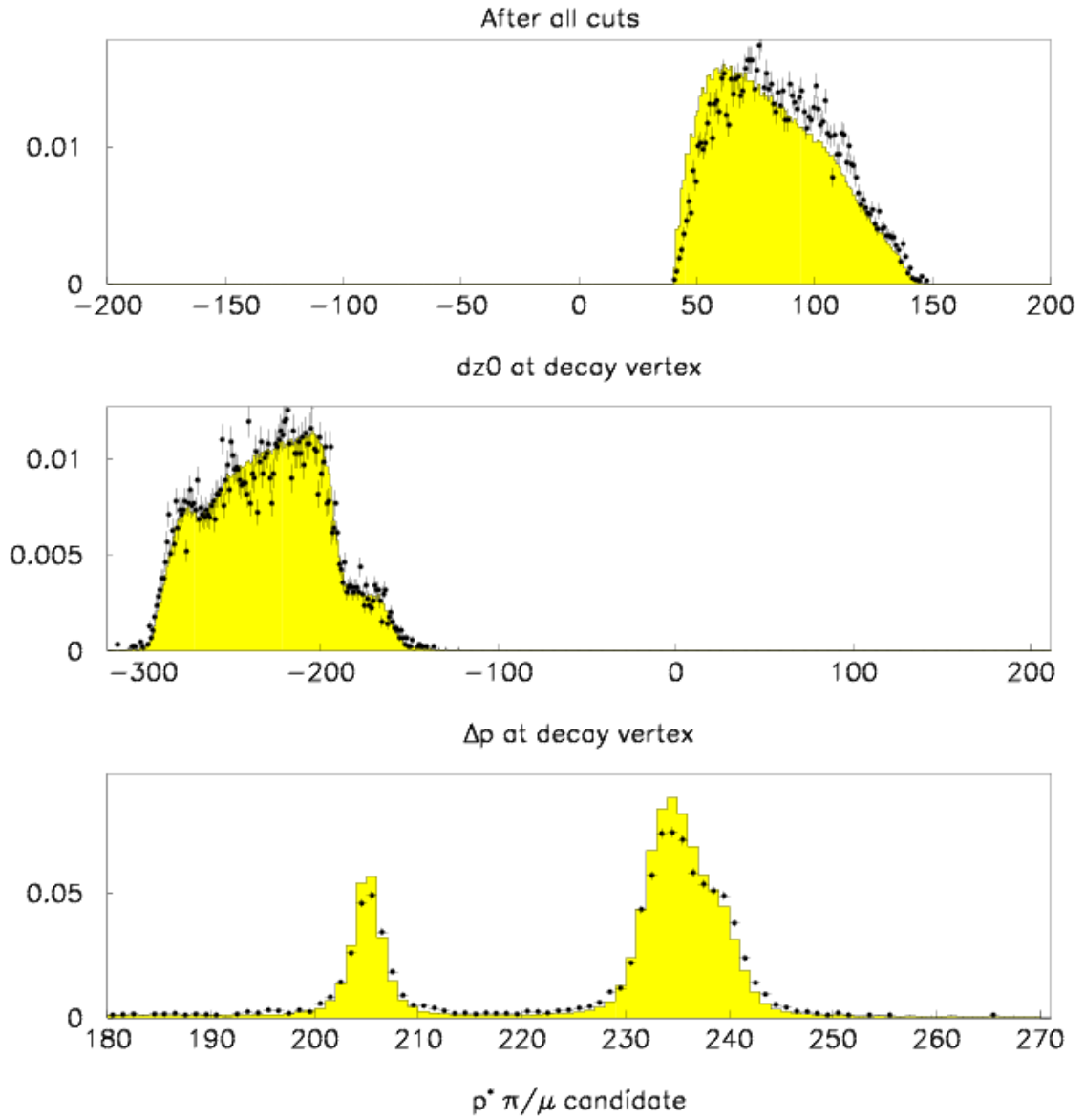
Figure 4.7: Distribution of $d_0 \equiv R_V$ (above), Δ_p (in the middle) and p^* (below) the cut on the secondary have been applied. Dots represent data and the yellow histogram represents Monte Carlo.

ID		3210
ENTRIES		149666
0.00	113.	2.90
0.00	0.724E+04	125.
0.00	0.00	0.00
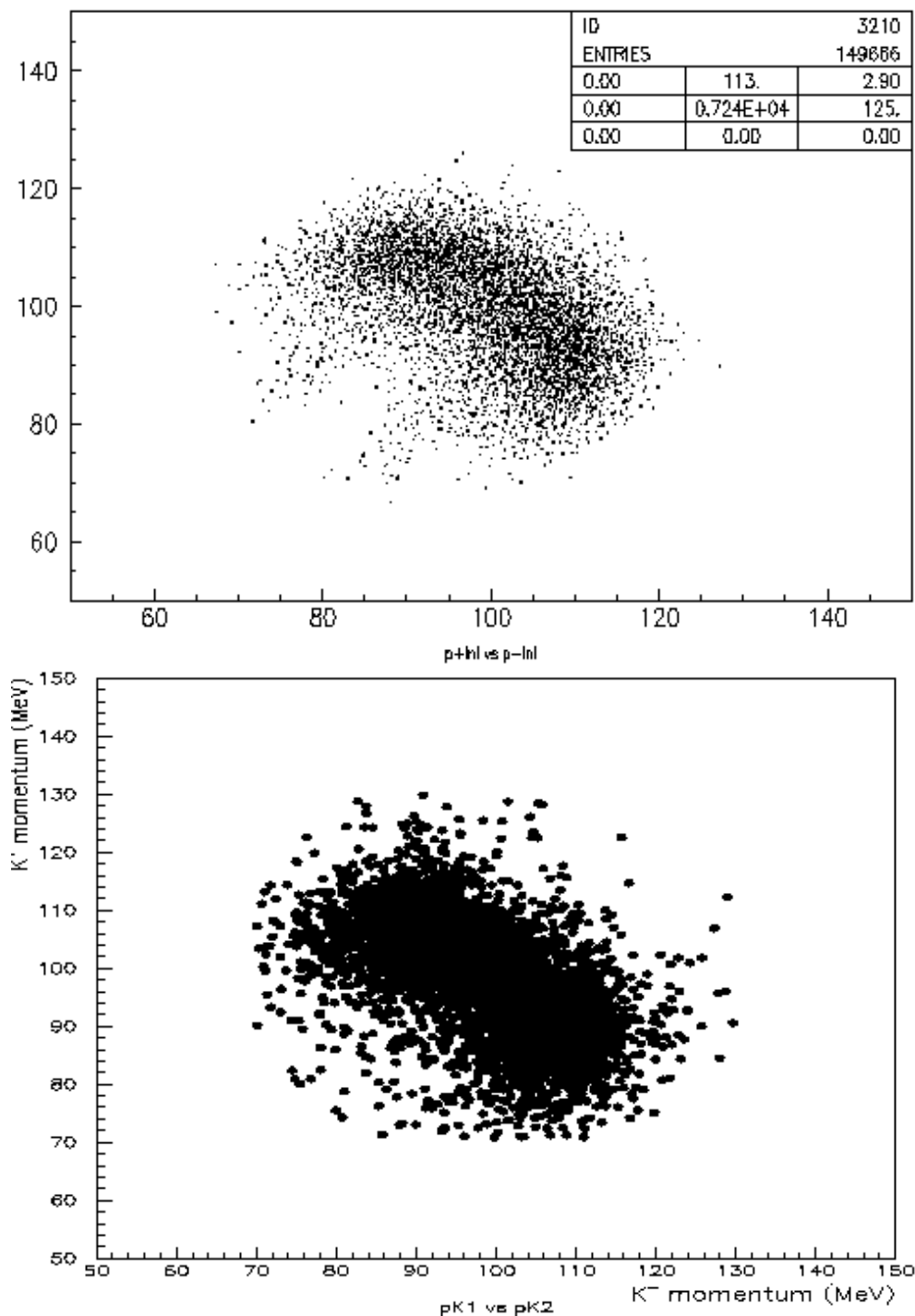
Figure 4.8: Momentum of K^+ versus the momentum of K^- for Monte Carlo simulation (above) and double tagged events (below). The background due to pions photoproduced on the beam-pipe visible in figure 4.3 has disappeared.

4.2 Retracking, merging and absolute timing

The KLOE reconstruction has been conceived to track neutral kaon decays. The tracking procedure is performed in the pion mass hypothesis. Therefore the reconstruction is not optimized for charged kaon tracks (see figures 4.9 and 4.10). It was mandatory to develop a retracking and merging procedure which takes into account the right mass hypothesis and the dE/dx in the chamber walls.

The retracking is performed taking into account the energy losses crossing the various detector materials or between consecutive hits traveling through the gas in the DC using the Bethe-Bloch formula under the correct mass hypothesis. It produces improvement of all quantities involved, as can be seen in figures 4.11, 4.12 and 4.13, where are shown respectively the improvements on the kaon momentum resolution, the improvement on the vertex resolution and the number of broken kaon tracks.

Also the reference time $T0$ must be calculated again because the standard KLOE procedure is based on photons coming from the IP (see section 3.1.1). The correct knowledge of the kaon momentum, obtained by the retracking, allows to re-compute the absolute $T0$ of the event, and consequently to improve the quality of the reconstruction of the whole event. The $T0$ finding is based on vertex position, cluster times, momentum of kaon and charged secondary at vertex for particles involved in the tag hemisphere and is performed tracing back the particles from the calorimeter to the IP, taking into account dE/dx for kaons.

For $\pi\pi^0$ decays it is possible to check neutral versus charged reconstructed decay time. Using double tag events it is possible to extract $T0$ resolution from data ($T0_+ - T0_-$). The $T0$ global algorithm has an high efficiency $\sim 96\%$, good resolution $\sigma_{T0} \sim 0.7 \; ns$ and it can be monitored from data with double tagged events.
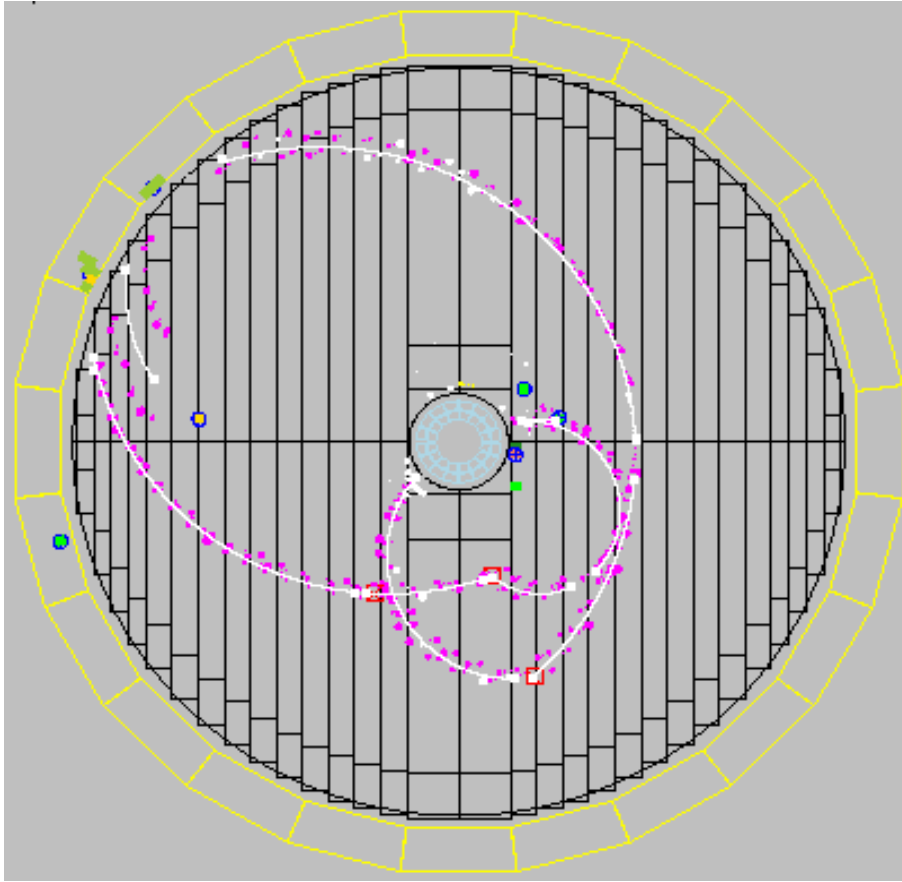
Figure 4.9: Reconstruction, without retracking of a $K^+ \to \mu^+\nu$, $K^- \to \mu^-\overline{\nu}$ event. Three fake vertexes have been reconstructed besides the two true vertexes.
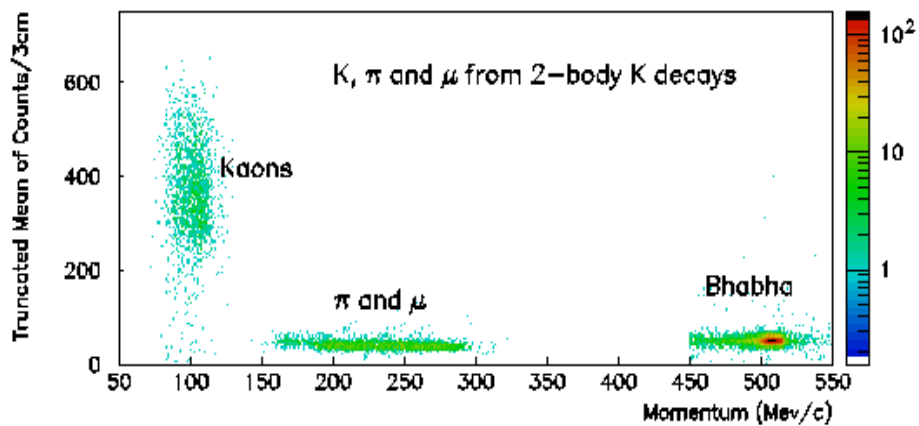
Figure 4.10: Energy released in the big cells versus the momentum of the particle, it is possible to see the big difference of energy released between kaons and their secondaries.
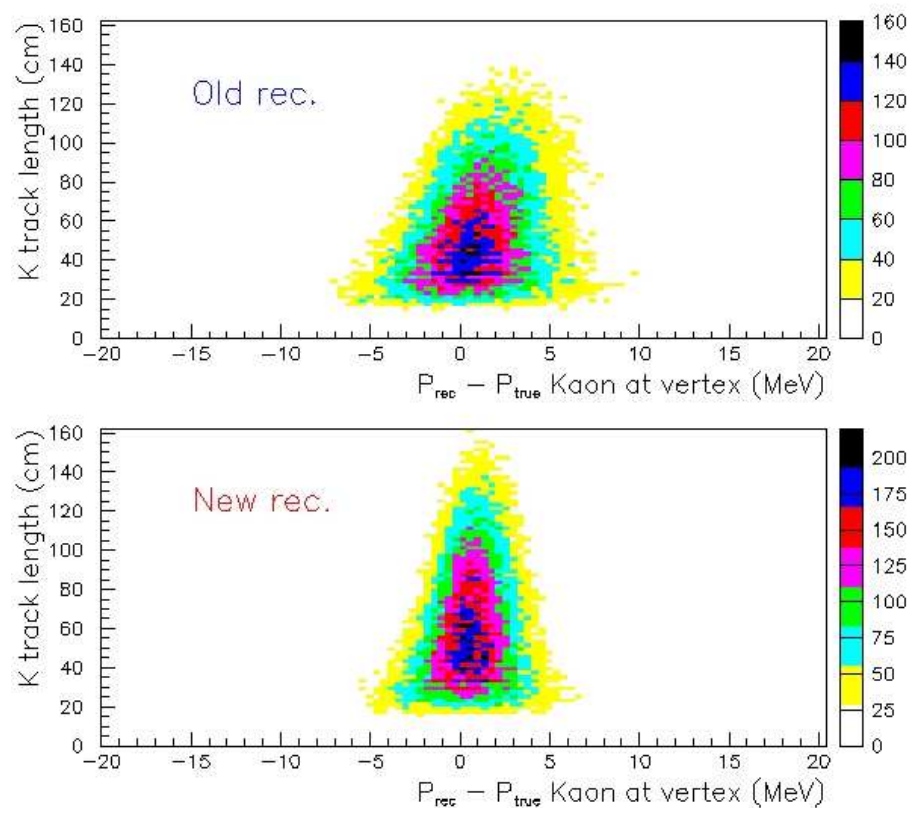
Figure 4.11: Resolution on the kaon momentum before (above) and after (below) retracking.
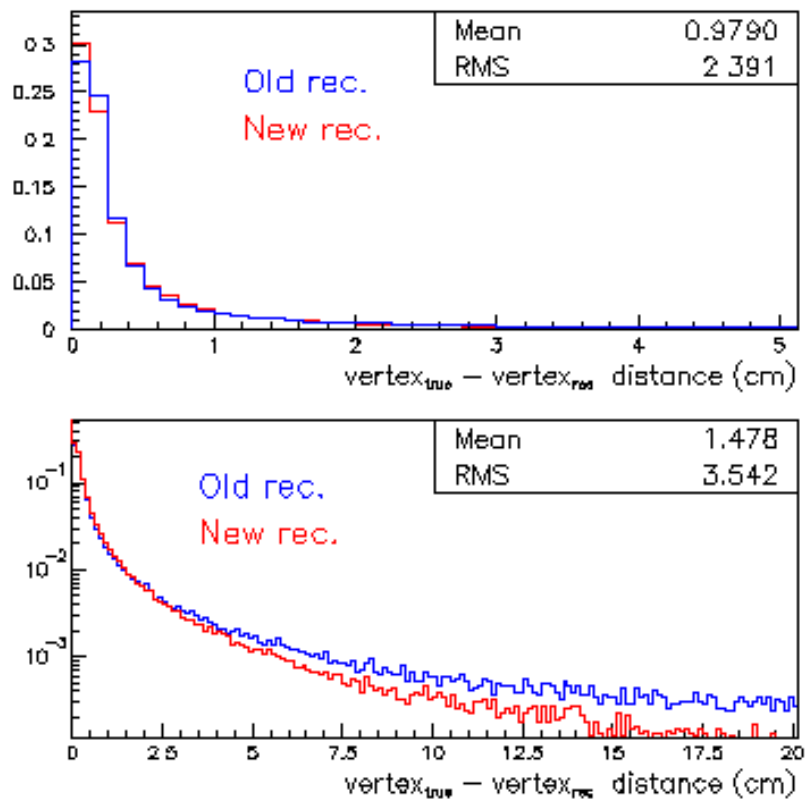
Figure 4.12: Vertex resolution before (above) and after (below) retracking.
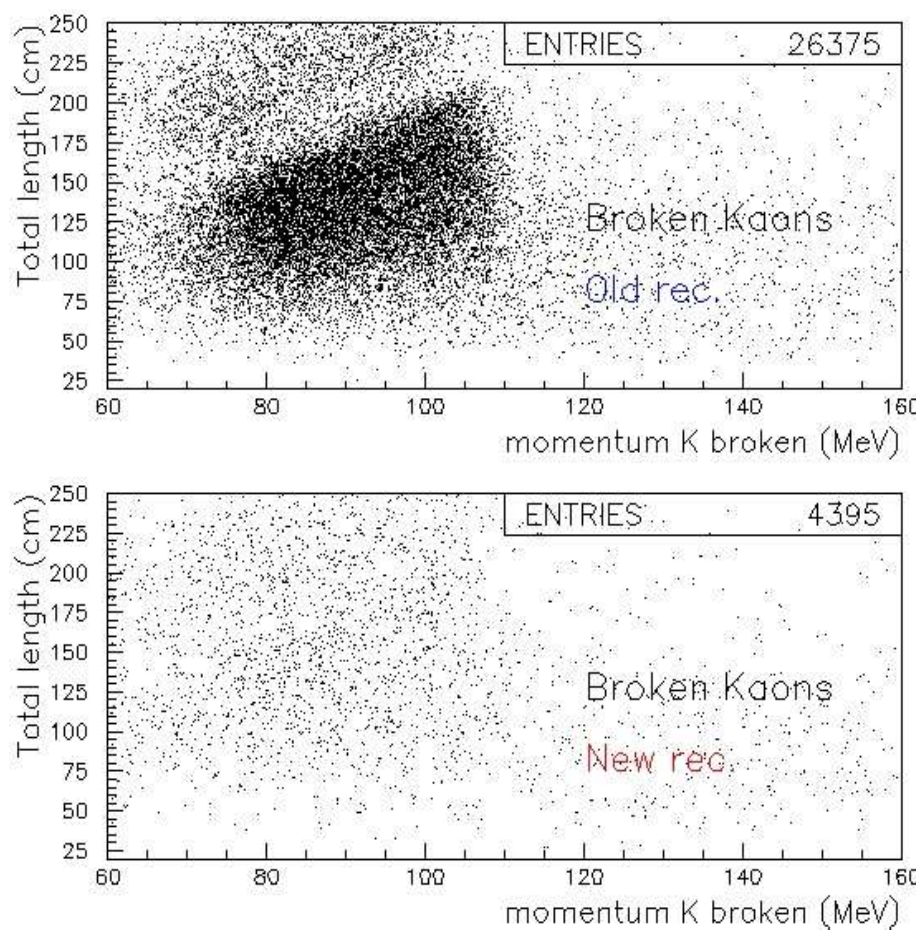
Figure 4.13: Number of broken kaon tracks before (above) and after (below) retracking.
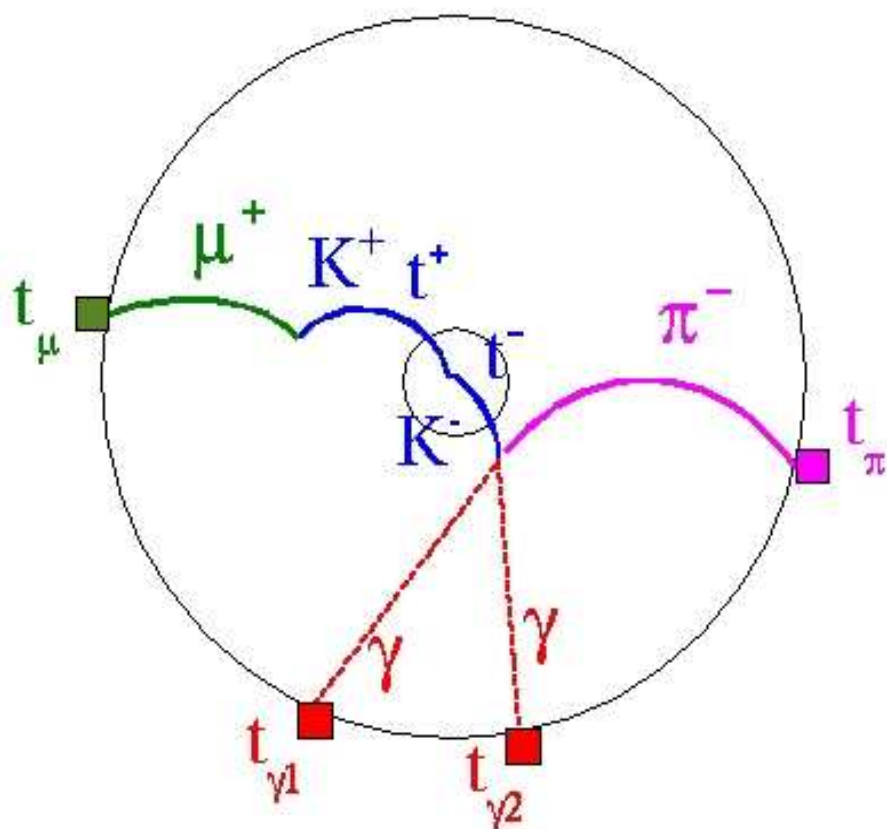
Figure 4.14: A schematic picture of a double tag $K \to \mu\nu$, $K \to \pi\pi^0$ event. The times of the clusters can be used for the $T0$ evaluation.
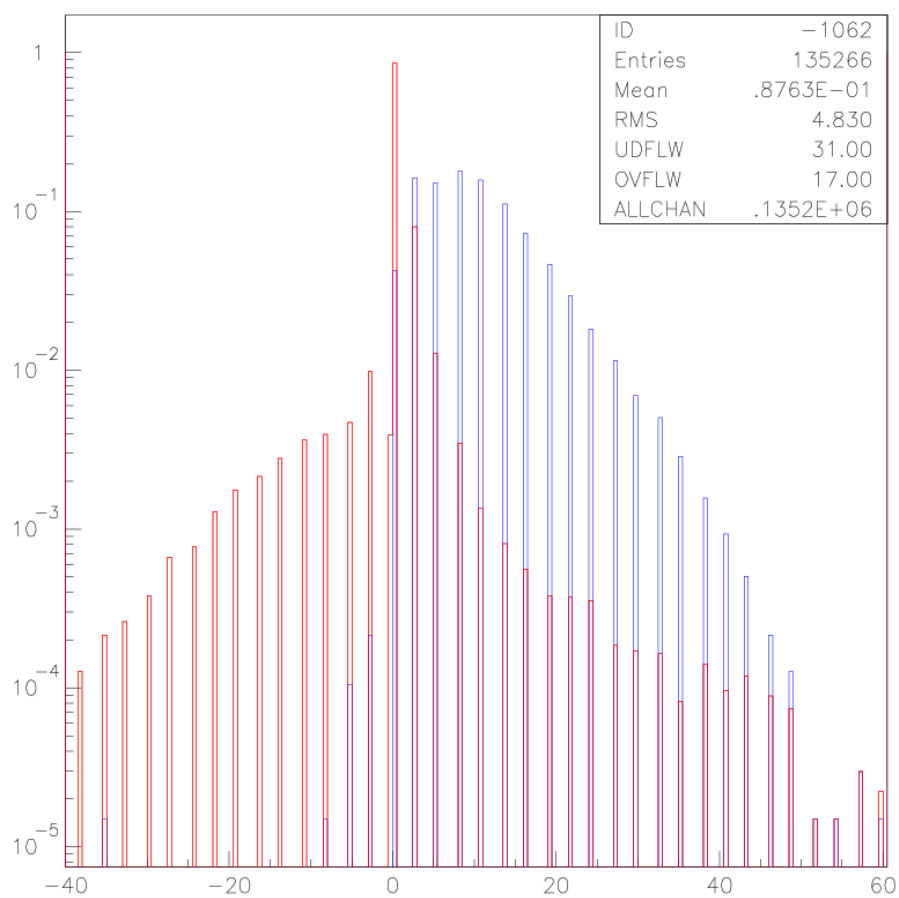
Figure 4.15: $T0$ evaluation for Monte Carlo charged kaon events, using the photon from the IP (in blue) and with charged kaon dedicated procedure (in red).

Chapter 5

The analysis

5.1 Introduction

In the following we describe the measurement of the charged kaon lifetime. This measurement is eagerly awaited from our community in order to clarify the present situation showing discrepancies between "in-flight" and "at-rest" measurements, so far used in the PDG average. Moreover this quantity is a fundamental parameter for the extraction of the V_{us} element of the CKM matrix, together with all the other inputs measurable at KLOE, namely the semileptonic branching ratio and the form factor slopes.
In order to cross check systematic effects we developed two different analysis methods: the kaon decay length and the kaon decay time measurement.
The measurement of the charged kaon decay length requires the reconstruction of the kaon decay vertex using only Drift Chamber, DC, information while the kaon decay vertex reconstruction efficiency is evaluated using a control sample given by ElectroMagnetic Calorimeter, EMC, information only.
The second method relies on the measurement of the kaon decay time using EMC information only. We consider events with a π^0 in the final state only:

$$K^{\pm} \rightarrow X + \pi^0 \rightarrow X + \gamma\gamma \tag{5.1}$$

In this case the kaon decay vertex reconstruction efficiency is evaluated using a control sample given by DC information only.

5.2 Analysis scheme

The procedure of this analysis can be summarized as follows:

1. Selection of a pure "$K^{\pm}$ beam" using the tag algorithm (see section 5.4).

2. Definition of the two methods and for each method:

(a) determination of the charged kaon proper time distribution (see sections 5.5.1 and 5.5.2), evaluation of the background events and background rejection, (see sections 5.5.1 and 5.5.2),

(b) evaluation of the efficiency to reconstruct the charged kaon decay vertex on data. The efficiency is corrected to take in account a small discrepancy between the true and the reconstructed MC efficiencies (see sections 5.6.1 and 5.6.2),

(c) measurement of the resolution curves as a function of the charged kaon proper time (see sections 5.7.1 and 5.7.2).

(d) fit of the proper time distribution, taking into account the correction given by the kaon decay vertex reconstruction efficiency and the resolution effects (see sections 5.8.1 and 5.8.2),

(e) evaluation of the systematics on the measurement. (see sections 5.9.1 and 5.9.3).

3. Evaluation of the correlation between the two different methods and of their weighted mean (see sections 5.10).

5.3 Data sample

The sample used for this analysis has been collected during 2002 data taking, processed and filtered with the KLOE standard reconstruction software and the event classification procedure [46]. We used about 210 pb^{-1} of data to evaluate the charged kaon decay vertex reconstruction efficiency as a function of the charged kaon proper time; we used 210 pb^{-1} of data to measure the charged kaon proper time distribution and the resolution curves.
We have produced about 175 pb^{-1} of MonteCarlo Which were used to evaluate the charged kaon decay vertex reconstruction efficiency as a function of the charged kaon proper time and to measure the charged kaon proper time distribution and the resolution curves.

5.4 Selection of the self-triggering tag events

The peculiarity of a ϕ-factory is that kaons are produced in pairs, namely K^+K^- and K_LK_S. Therefore the detection of a K guarantees the presence of a $\bar{K}$ on the other side with known momentum and direction. This feature allows the measurement of absolute branching ratios. The decay products of the $K^\pm$ pair define two ideally separated regions called hereafter the tag and the signal hemispheres.
To measure the charged kaon lifetime we consider the subsample of events selected by the TAG algorithm (see section 5.4.1). Once the algorithm has found a $K^\mp$ tag decay, it can be used as reference normalization and the kaons in the other hemisphere can

be considered as a pure $K^{\pm}$ beam. In the two-body decays the secondary tracks have a well defined momentum in the kaon rest frame and this allows a good particle identification. To minimize the impact of the trigger efficiency on the signal side, we look for a tag decay which also provided by itself the EMC trigger of the event. Even if the analyzed events already belong to the charged kaons stream, it is necessary to reprocess them for the following reasons: to tighten the requirements on the tag decay, cleaning the data sample, and to select a specific charge for the self-triggering tags (see section 5.4.2).

Hereafter we use a coordinate system with the z-axis defined as the bisectrix of the beams, the y-axis vertical and the x-axis toward the center of the collider rings.

5.4.1 The TAG algorithm

The TAG algorithm identifies the two-body decays $K \to \mu\nu$ or $K \to \pi\pi^0$, which are about 85% of charged kaon decays. It is based on the presence of a two-tracks vertex in the DC which defines the $K^{\pm}$ decay.

The first requirement is the existence of a track (kaon candidate) with the point of closest approach to the IP smaller than $d_0 = 10$ cm ($z_0 = 20$ cm) along the radial (longitudinal) axis. Then the radial distance between the kaon candidate decay vertex and the beam axis, R_V, has to fulfill $40 < R_V < 150$ cm. The kaon candidate must also have $70 < |\overrightarrow{p}| < 130$ MeV/c.

Once the kaon candidate has been identified:

- the candidate track associated to the charged decay particle (secondary) must have the same charge of the kaon;

- the momentum difference between the kaon and the secondary must fulfill $-320 < \Delta p = |\overrightarrow{p}_K| - |\overrightarrow{p}_{sec}| < -120$ MeV/c;

- the secondary charged particle momentum in the kaon rest frame, p^*, using the $\pi^{\pm}$ mass hypothesis, must be in the range $180 < p^* < 270$ MeV/c.

The following cuts are applied to distinguish between K_{μ} and $K_{\pi\pi^0}$ decays:

$$225 < p^* < 245 \text{ MeV/c} \qquad \Rightarrow \qquad K_{\mu}\text{-tag} \qquad (5.2)$$

$$195.5 < p^* < 213.5 \text{ MeV/c} \qquad \Rightarrow \qquad K_{\pi\pi^0}\text{-tag}. \qquad (5.3)$$

5.4.2 Self-triggering conditions

The particles on the tagging side are required to deposit enough energy in the calorimeter to trigger the data acquisition (self-triggering tag). The EMC trigger is given by two energy deposits in two trigger sectors which overcome the LET threshold [47], whose average values corresponds to about 50 MeV in the barrel and about 150 MeV in the endcaps.
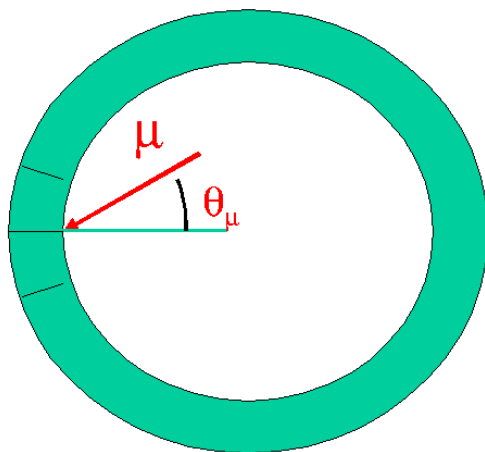
Figure 5.1: Schematic geometrical overview of a K_μ self-triggering event. Depending on the incidence angle θ_μ, the muon can cross two trigger sectors and then self-trigger the event.
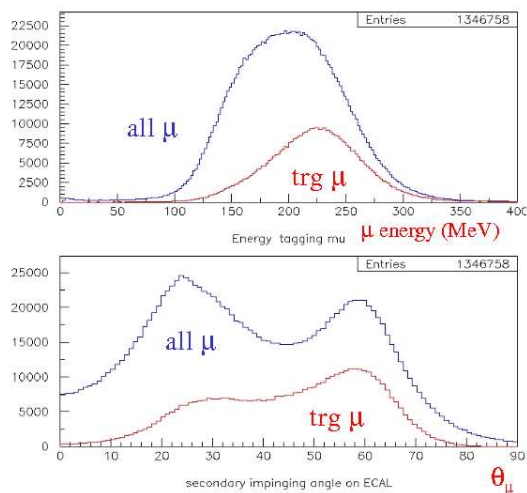
Figure 5.2: Above: distribution of self-triggering muon as function of the energy released by the muon in the calorimeter. Below: distribution of self-triggering muon as function of its impinging angle on the EMC.

The possibility for a K_μ decay to self-trigger the event is due to the cluster associated to the secondary $\mu^\pm$ track. The trajectory of the $\mu^\pm$ in the EMC can cross two adjacent trigger sectors. If the two energy deposits are over threshold we have a self-triggering K_μ decay event. The self-triggering request reduces the analysis sample. The yield has been evaluated on a 4.85 pb^{-1} data sample. The results are reported in table 5.1. The amount of self-triggering K_μ tag decays is about 35%. In the case of $K_{\pi\pi^0}$ tag decay the amount of self-triggering event is about 75%; this is due to the fact that either the charged pion or the photons from the π^0 decay can overcome the calorimeter energy threshold.

Kind of tag	Number of tags/pb^{-1}	Number of self-trigger/pb^{-1}
$K^- \rightarrow \mu^- \bar{\nu}$	279×10^3	95×10^3
$K^- \rightarrow \pi^- \pi^0$	95×10^3	73×10^3

Table 5.1: Number of self-triggering tag events per pb^{-1}, evaluated using a data sample of about 4.85 pb^{-1}

For the measurement we require self-triggering tags. It must be stressed that after the self-triggering tag request, we end up on the opposite hemisphere with a pure $K^\pm$ beam.

5.4.3 Why self-triggering request?

Before entering in the details of the analysis, we should comment on the self-triggering request. As shown in the previous section this request reduces the analysis sample, in fact the amount of self-triggering K_μ tag decays is about 35%. To understand the reason of this choice we have to study, on MonteCarlo simulation, the trigger efficiency, the tag efficiency given the trigger and the self-triggering tag efficiency as functions of the signal kaon *true* proper time which is the proper time given by the MonteCarlo simulation. It is defined as:

$$t^*_{true} = tof^K_{true} \cdot \sqrt{1 - \beta^2_{true}} \qquad \text{where} \qquad \beta_{true} = (\beta^{IP}_{true} + \beta^{VTX}_{true})/2, \qquad (5.4)$$

tof^K_{true} is signal kaon time of flight, in the laboratory frame, given by the MonteCarlo simulation while β^{IP}_{true} and β^{VTX}_{true} are the β values of the signal kaon at the Interaction Point, IP, and at the decay vertex, respectively. The energy loss in the DC decreases the beta of the kaon. This effect leads to an underestimate of about 0.65% of the true proper time. A correction has been introduced to take into account this effect. The trigger efficiency is defined as the ratio of the events K^+K^- with a trigger signal over threshold over the total number of K^+K^- events, as a function of the *true* proper time:

$$\varepsilon_{\text{Trig}} = \frac{N_{\text{Trig}_{K^+K^-}}}{N_{K^+K^-}}. \qquad (5.5)$$

The tag efficiency is defined as the ratio of triggered events with a tagging kaon over all the triggered K^+K^- events, as a function of the *true* proper time:

$$\varepsilon_{\text{Tag}} = \frac{N_{\text{TrigTag}}}{N_{\text{Trig}_{K^+K^-}}}.$$

(5.6)

The self-triggering tag efficiency is defined as the ratio of the events K^+K^- in which we reconstruct a self-trigger tag over all the events K^+K^-, as a function of the true proper time

$$\varepsilon_{\text{StrTag}} = \frac{N_{\text{StrTag}}}{N_{K^+K^-}}$$

(5.7)
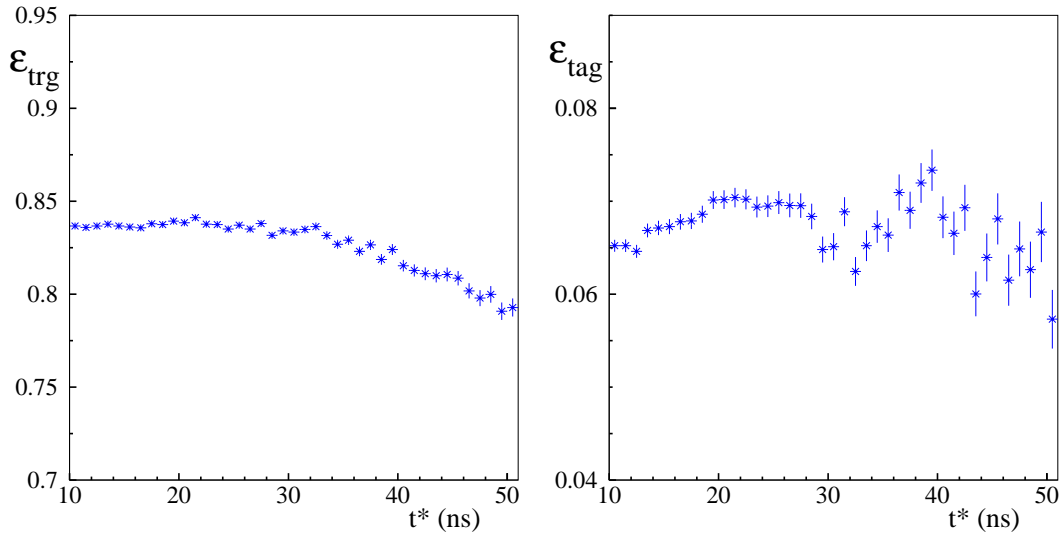
Figure 5.3: Left. Trigger efficiency as a function of the charged kaon proper time. Right. Tag efficiency, given the trigger, as a function of the signal kaon proper time.

As shown in figure 5.3, the trigger and moreover tag efficiencies behavior with respect to the kaon proper time are not flat. Therefore we should correct for these effects relying blindly in the MC. Instead, the self-triggering tag efficiency is constant for a wide range, between 12 and 35 ns and therefore we will use the self-triggering request, see figure 5.4.

In order to check the goodness of the MonteCarlo simulation we use the double tag events, events in which both the charged kaons are reconstructed and tagged, to compare on data and on MonteCarlo datalike the self trigger tag efficiency. This procedure has been used only to assess the systematic uncertainty on the MonteCarlo self-triggering tag efficiency used in our fit.
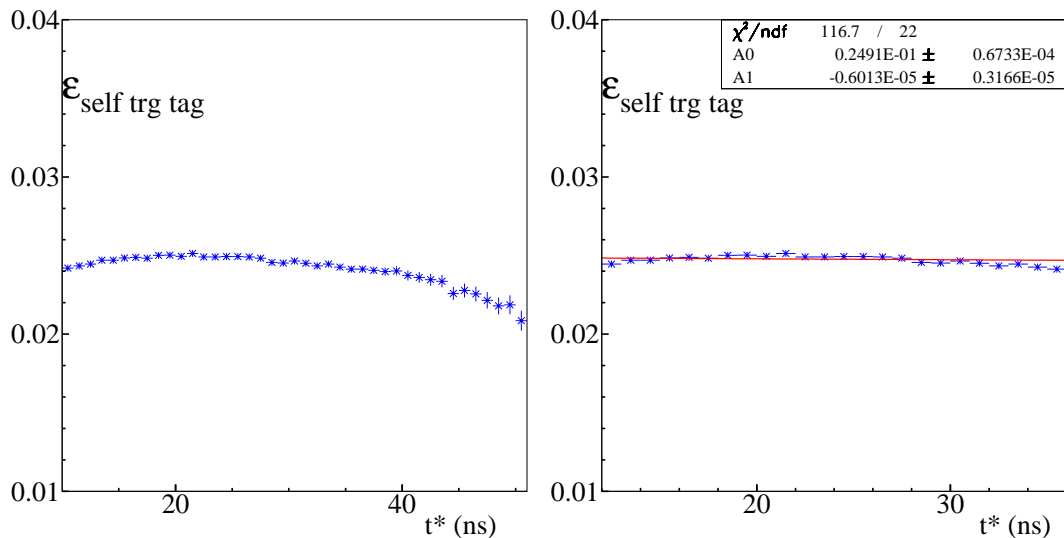
Figure 5.4: Left. Self-triggering tag efficiency as a function of the signal kaon proper time. Right. Zoom of the region between 12 and 35 ns.

The self-triggering tag efficiency, evaluated with the double tag events, is defined, bin by bin, as:

$$\varepsilon_{\text{StrTag(double tag)}} = \frac{N_{\text{StrTag2}(\mu_2)}}{N_{\text{StrTag1}}} \tag{5.8}$$

where N_{StrTag1} is the number of events in which a $K^{\mp}$ tags the event as a $K^{+}K^{-}$ event and fires the trigger, while $N_{\text{StrTag2}(\mu_2)}$ is the number of events in which a $K^{\pm} \rightarrow \mu^{\pm}\overset{(-)}{\nu}_{\mu}$ independentelly tags the event as a $K^{+}K^{-}$ event and fires the trigger. This efficiency is function of the reconstructed proper time. As it can be seen in the fig. 5.5 the agreement between the self-triggering tag efficiency evaluated using the double tag events on data and on MC datalike is good.

5.5 The event selection

5.5.1 First method: charged kaon decay length

For the first method we measure the kaon decay length, from the IP to the kaon decay vertex, reconstructed in the DC. The reconstruction efficiency of the kaon decay path is evaluated using a control sample selected with EMC information only.

Charged kaon proper time distribution

Given a charged kaon fulfilling the self-triggering tag requirements, our signal is given by an opposite charged kaon which decayed in the DC. This signal is selected looking
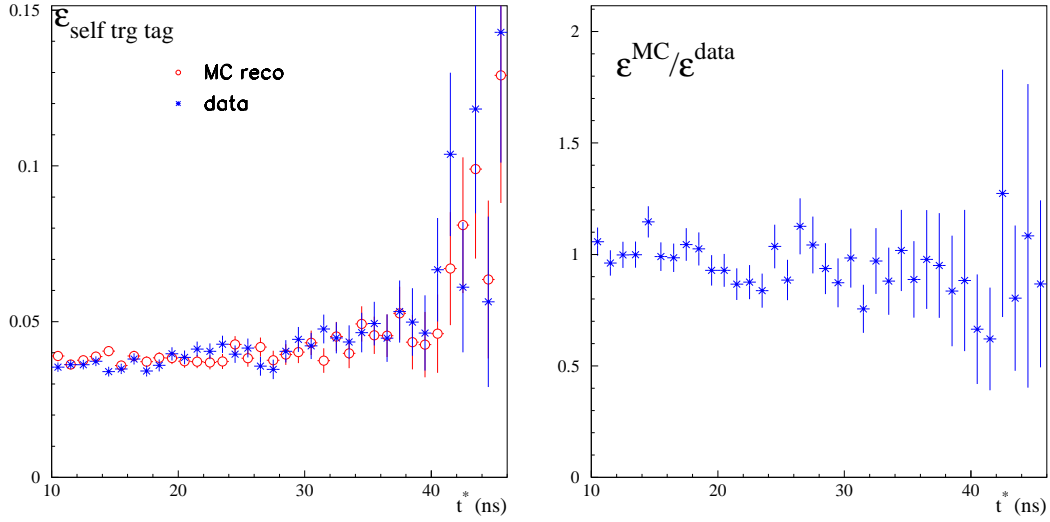
Figure 5.5: Left. Self-triggering tag efficiency evaluated using the double tag events on data (blue) and on MC datalike (red). Right. Ratio of the self-triggering tag efficiency evaluated and data over the one evaluated on MC datalike, using the double tag events.

for a charged kaon track, the signal kaon track, defined by the following requests:

$$R_{PCA} < 10 \text{ cm} \qquad \text{where} \quad R_{PCA} = \sqrt{x_{PCA}^2 + y_{PCA}^2}, \qquad (5.9)$$

$$|Z_{PCA}| < 20 \text{ cm}, \qquad (5.10)$$

$$70 < P_K < 130 \text{ MeV/c}. \qquad (5.11)$$

where $X_{PCA}, Y_{PCA}, Z_{PCA}$ are the coordinates of the Point of Closest Approach of the kaon track to the IP. Using the extrapolation of the tagging kaon track to the IP, the ϕ−meson momentum measured from Bhabha scattering events and imposing momentum conservation, we can evaluate the momentum of the signal kaon at the IP and build the path of the signal kaon up to the DC (helix reconstruction). This allows us to apply further cuts on differences between the signal kaon track and the signal kaon helix, namely:

- the difference between the momenta evaluated at the first hit has to be less than 20 MeV/c;

- the distance between the signal kaon track and the signal kaon path, extrapolated until the first hit, has to be less than 20 cm, see figure 5.6.

The next step is to look for the charged kaon decay vertex. We select the vertex which connects the signal kaon track with another track different from the tag kaon
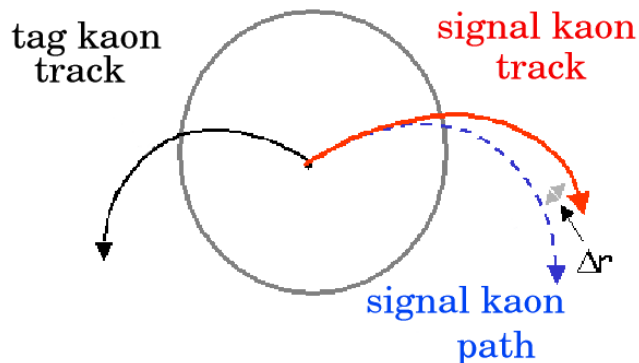
Figure 5.6: Exempli of the difference between signal kaon track and the reconstructed kaon path.

track. The vertex coordinates have to satisfy the following request:

$$40 \text{ cm} < R_{VTX} < 150 \text{ cm} \qquad \text{where} \quad R_{VTX} = \sqrt{x_{VTX}^2 + y_{VTX}^2}, \quad (5.12)$$

$$|Z_{VTX}| \leq 150 \text{ cm}, \tag{5.13}$$

The charged kaon proper time, t^*, for a kaon with path length l is defined as:

$$t^* = \frac{\sqrt{1 - \beta^2}}{\beta} l. \tag{5.14}$$

Therefore we have to account for the changes of the β value of the kaon due to energy losses in the DC. For this reason we divide the signal kaon track in small steps of 5 mm, Δl_i, and we evaluate the energy loss and each step using the Bethe-Bloch formula. We calculate the charged kaon β and obtain the proper time of the kaon for every step:

$$\Delta t_i^* = \frac{\sqrt{1 - \beta^2}}{\beta} \Delta l_i. \tag{5.15}$$

The sum of Δt_i^* gives the charged kaon proper time:

$$t^* = \sum_i \Delta t_i^*, \tag{5.16}$$

its distribution is shown in figure 5.7. This distribution has to be corrected, bin by bin, for its reconstruction efficiency and for its resolution effects. The shoulder visible in the region between 30 and 40 ns is due to events in which the kaon decay vertex has been wrongly reconstructed. This background has been evaluated and studied using the MonteCarlo simulation.
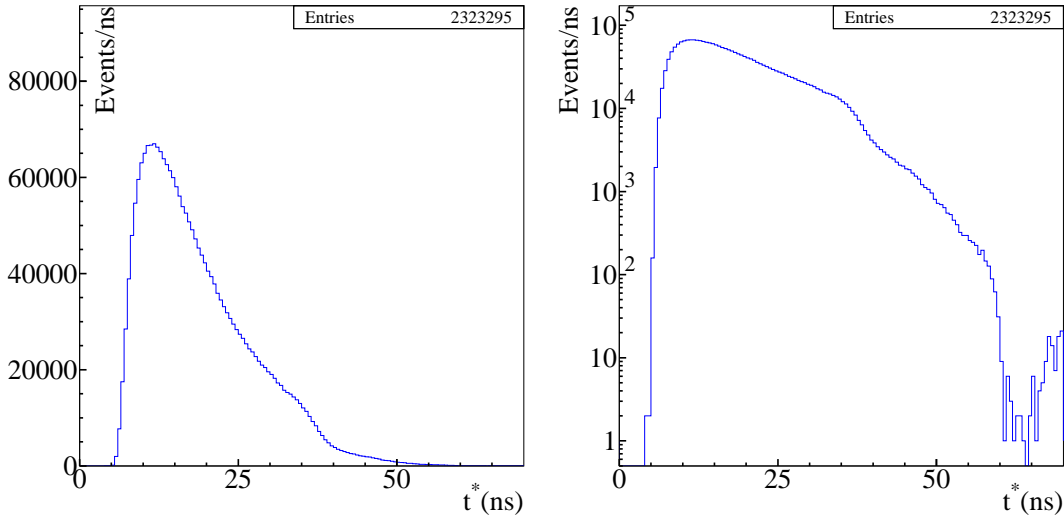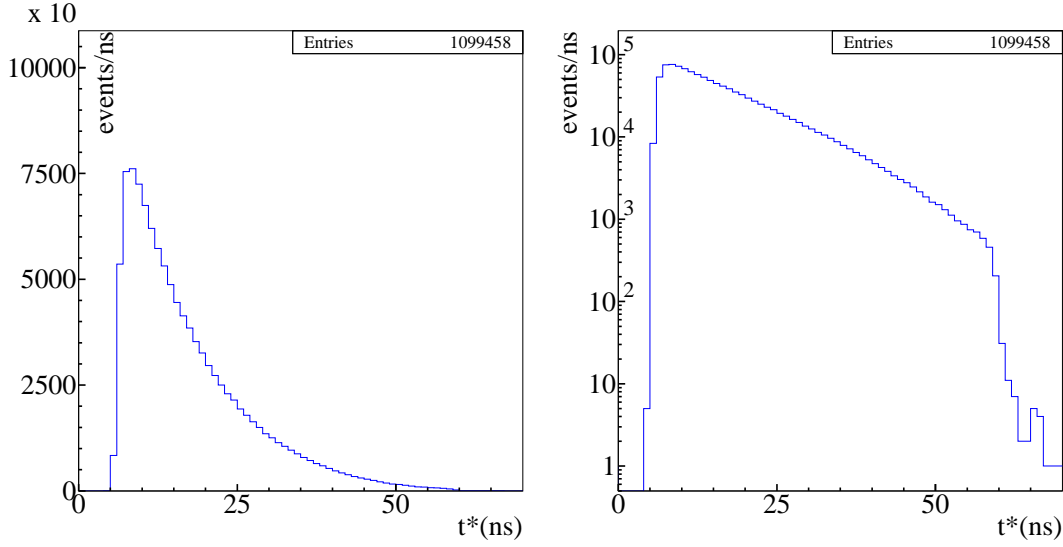
Figure 5.7: Charged kaon proper time distribution in linear and logarithmic scale evaluated on data, for the first method.

Background evaluation

The charged kaon proper time distribution shown in figure 5.7 is composed by four families:

1. correctly reconstructed vertices, about 69.1%,

2. kaon decays in pion which early decays in muons; the pions hits are associated to the muon track, about 1.4%,

3. wrongly reconstructed vertices, in which some hits of the kaon track are associated to the secondary track, about 20.6%,

4. wrongly reconstructed vertices, in which some hits of the secondary track are associated to the kaon track, about 5.2%,

5. vertices obtained from kaon broken tracks, about 3.7%, see figure 5.8.

The vertices not obtained from kaon track are less than 0.02% and are given by electron, muon or pion tracks reconstructed as kaon tracks.
In figure 5.9 the different contributions to the proper time distribution given by the above listed families are shown.
It is possible to see, in logarithmic scale, that the first four families have the same slope and that the last one has a peak in the region between 30 and 40 ns. In figure 5.10 the distributions of the resolution on the charged kaon proper time for the different families, evaluated using MonteCarlo, are shown.
The measured proper times for the first four families have a small shifts with respect to the "true" proper time (and much smaller than the bin size we use in the fit, 1 ns).

Figure 5.8: Vertex obtained by a kaon broken track.

.
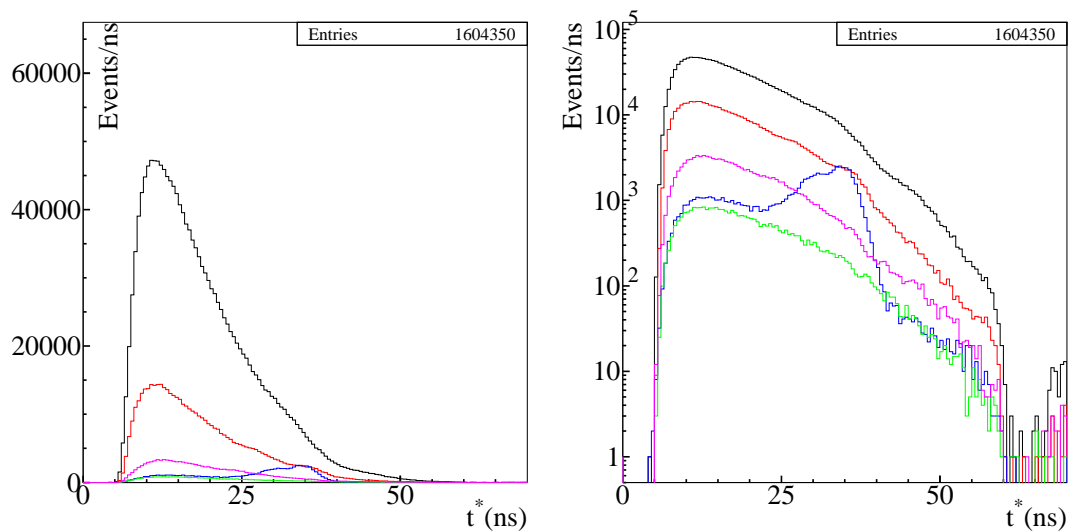
Figure 5.9: Different contributions to the proper time distribution in linear and logarithmic scale. Five families are described and listed in the text: 1. (black); 2. (green); 3. (red); 4. (pink); 5. (blue).

These effects can thus just be taken into account by measuring the resolution function. The fifth family must be rejected in order to not spoil the lifetime measurement.

Background rejection

In order to cut this background we can use the momentum of the charged secondary particle (p_K^*) evaluated in the kaon rest frame, using the kaon mass hypothesis. For the vertices obtained from kaon broken tracks, we expect this variable to be very small, of the order of a few MeV/c.
The distribution of p_K^* is shown in figure 5.11. The peak in blue is given by the events in which the decay vertices come from kaon broken tracks.
Using the cut $p_K^* > 100$ MeV/c we lose about 5.6% of signal but we discard about 73.5% of this background. The charged kaon proper time distribution obtained applying this cut is shown in figure 5.12: the shoulder between 30 and 40 ns disappeared.

5.5.2   Second method: charged kaon decay time

For the second method we measure the kaon decay time obtained using EMC information. The kaon decay time reconstruction efficiency is evaluated using a control sample given by DC information only.

Charged kaon proper time distribution

Given a charged kaon fulfilling the self-triggering tag requirements our signal is given by an opposite charged kaon decay reconstructed using EMC information only.
To do this we have developed the $\pi^0 \to \gamma\gamma$ vertex technique [48] based on events in which the kaon has a π^0 in the final state:

$$K^\pm \to \pi^0 X^\pm. \tag{5.17}$$

The π^0 is identified using the $\pi^0 \to \gamma\gamma$ decay vertex and the calorimetric information of the photon clusters. The kaon decay vertex coincides with the decay vertex of the π^0, the $\pi^0 \to \gamma\gamma$ vertex.
First of all we build the helix of the signal kaon as previously described in 5.5.1. In the EMC we look for clusters not associated to tracks in the DC, according to the KLOE track-to-cluster algorithm [46]. Among these we select the two (or three, if there are) most energetic clusters with:

$$24° < \alpha_{cl} < 156° \tag{5.18}$$

$$t_\phi < t_{cl} < t_\phi + 70 \text{ ns} \tag{5.19}$$

where α_{cl} is the polar angle, the angle between the direction of the cluster and the z axis, t_{cl} is the time of the cluster, and t_ϕ is the ϕ decay time evaluated considering
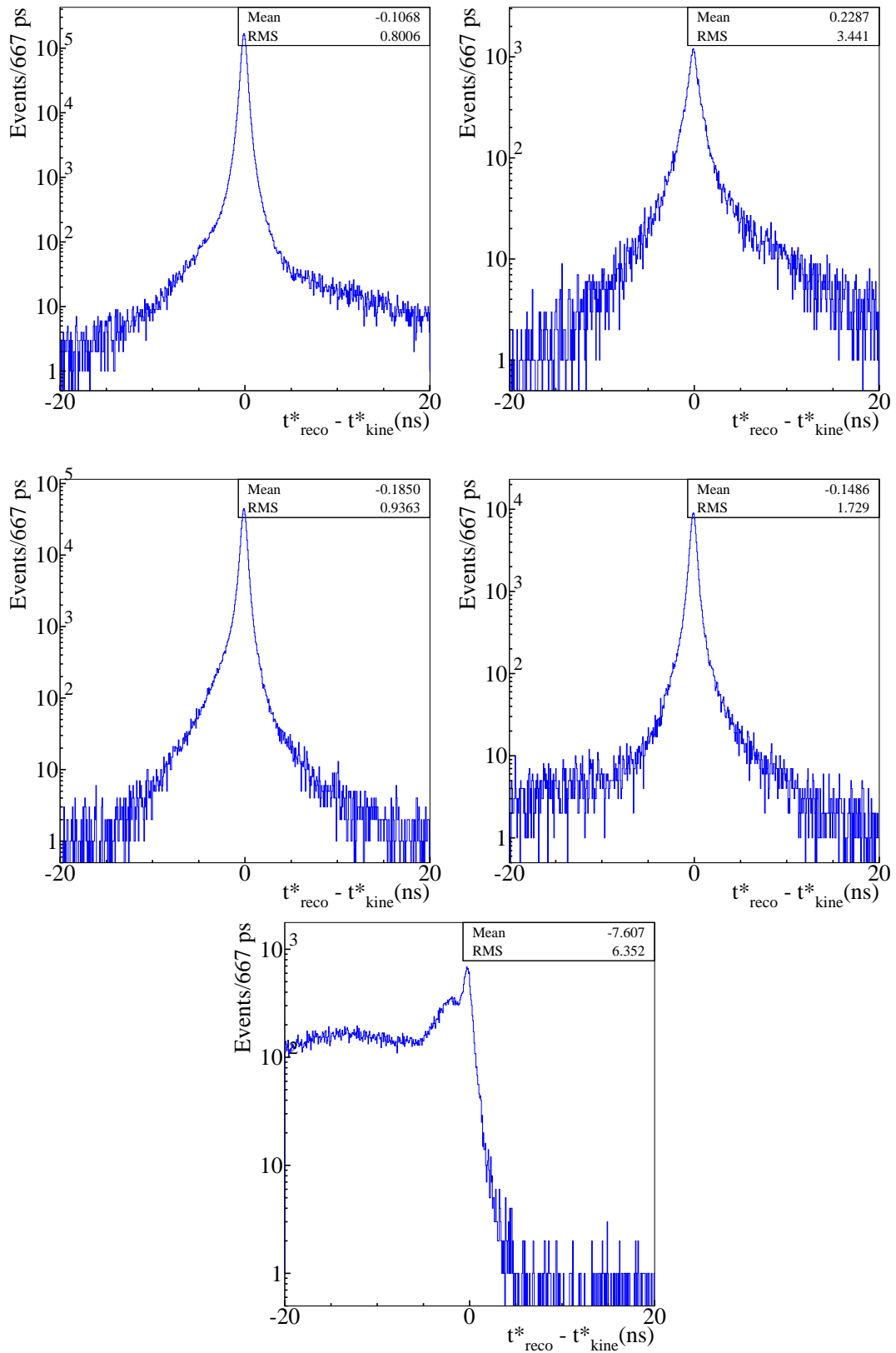
Figure 5.10: From top left, to bottom: resolution curves for the five families described in the text.
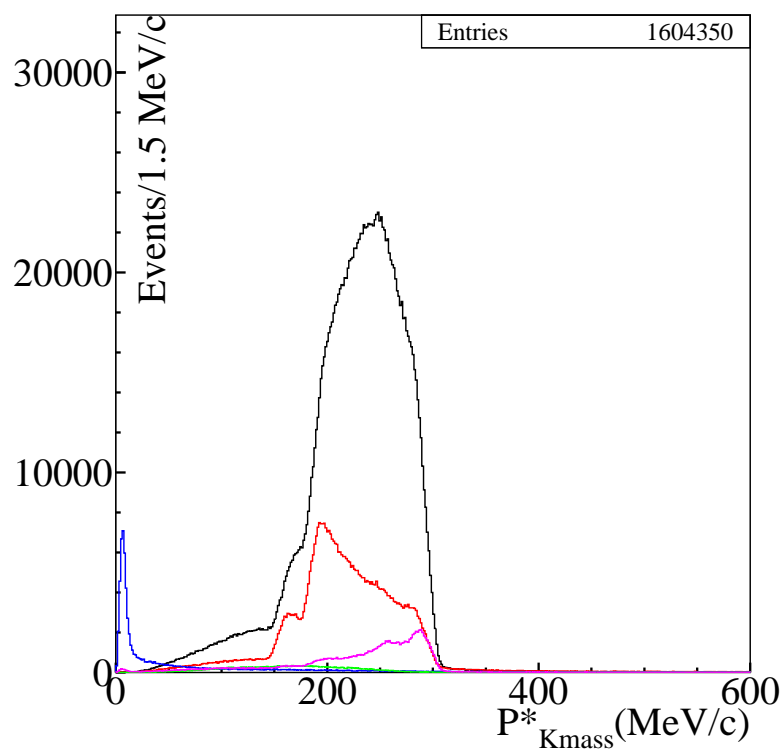
Figure 5.11: P_K^* for the five families described in the text. Colors are the same as in fig. (5.9).
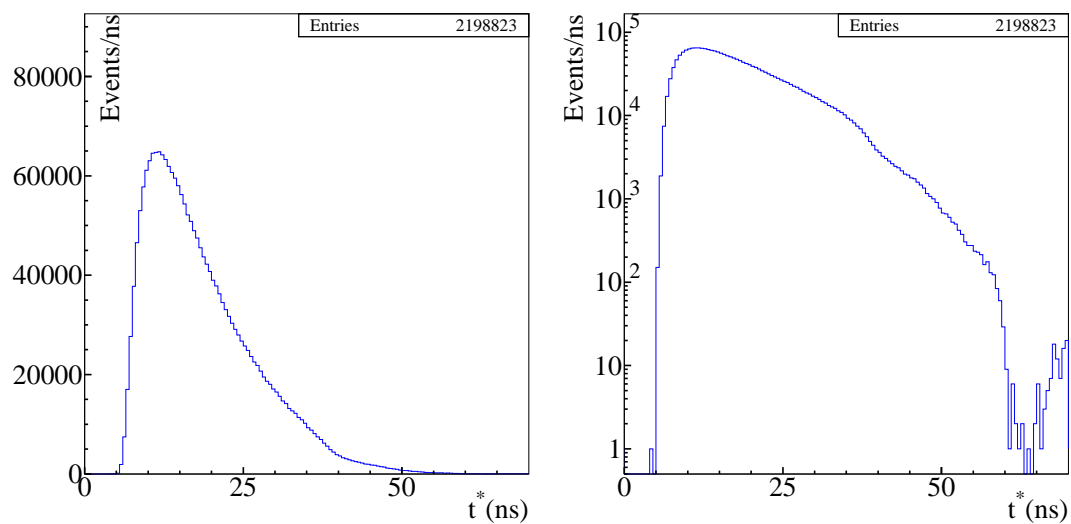
Figure 5.12: Charged kaon proper time distribution, in linear and in logarithmic scale, after the cut on p_K^*.

the $K_{\mu 2}$ decay chain on the tagging side. These cuts are used to remove the machine background. The request of three neutral clusters allows us to select also the events with the track of the charged decay particle not associated to its calorimeter clusters. Then we move along the path of the signal kaon helix with a step of 5 mm and we look for $\pi^0 \to \gamma\gamma$ decay vertex identified by minimizing a least square function obtained using the following quantities:

1.
$$(\Delta M_{\pi^0})^2 = (\sqrt{2E_{cl1}E_{cl2}(1-cos\theta)} - m_{\pi^0})^2 \tag{5.20}$$

where θ is the angle between the directions of the two photons given by π^0 decay, E_{cl1} and E_{cl2} are the energies of the neutral clusters fired by the photons and m_{π^0} is the π^0 mass (134.98 MeV). The direction of the photons is defined as the vector going from the candidate kaon decay vertex to the centroid of the selected neutral cluster in the EMC.

2.
$$(\Delta t)^2 = [(t_{cl_1} - \frac{\Delta x_1}{c}) - (t_{cl_2} - \frac{\Delta x_2}{c})]^2. \tag{5.21}$$

where t_{cl_i} is the time of the i-th cluster and Δx_i is the distance between the neutral cluster and the candidate kaon decay vertex.

3. The difference between the time of flight of the charged kaon, measured along the kaon trajectory, tof_K^{decay}, and the time of flight of the charged kaon measured using the EMC information of the two neutral clusters, tof_{cl}^{decay}:

$$(\Delta tof)^2 = (tof_K^{decay} - tof_{cl}^{decay})^2 \tag{5.22}$$

The first one, tof_K^{decay}, is measured taking into account the energy loss in the different materials given by the Bethe-Bloch formula;
the second one, tof_{cl}^{decay}, is obtained from the selected neutral clusters weighting their time differences $(t_{cl_i} - \frac{\Delta x_i}{c})$ with the time resolution $\sigma_{t_{cl_i}}$:

$$\sigma_{t_{cl_i}} = 140 \ ps \oplus \frac{57 \ ps}{\sqrt{E_{cl_i}(GeV)}}. \tag{5.23}$$

We define a χ^2-like variable which is:

$$\chi^2 = \frac{(\Delta M_{\pi^0})^2}{\sigma_{M_{\pi^0}}^2} + \frac{\Delta t^2}{(\sigma_{\Delta t})^2} + \frac{(\Delta tof)^2}{\sigma_{t_{decay}}^2} \tag{5.24}$$

where $\sigma_{M_{\pi^0}}$ is the resolution on the π^0 mass, of about of 17 MeV. $\sigma_{t_{decay}}$ is the uncertainty on the kaon decay time obtained from the selected neutral clusters and on the kaon decay time obtained from the kaon path, of the order of few hundreds ps.

In case three clusters have been selected we choose the pair with the best χ^2. The position along the signal kaon helix that gives the minimum value of the χ^2 defines the $\pi^0 \to \gamma\gamma$ vertex position. It is also required:

$$\chi^2 < 30, \tag{5.25}$$

$$80\,MeV/c^2 < M_{\pi^0} < 200\,MeV/c^2, \tag{5.26}$$

$$\left|\frac{\Delta t}{\sqrt{\sigma_{t_{cl_1}}^2 + \sigma_{t_{cl_2}}^2}}\right| < 5, \tag{5.27}$$

$$40(cm) < R_{\pi^0} < 150\text{cm} \qquad \text{where} \quad R_{\pi^0} = \sqrt{x_{\pi^0}^2 + y_{\pi^0}^2}, \tag{5.28}$$

$$|Z_{\pi^0}| \leq 150 \text{ cm}, \tag{5.29}$$

where $X_{\pi^0}, Y_{\pi^0}, Z_{\pi^0}$ are the coordinates of the $\pi^0 \to \gamma\gamma$ vertex. Using this procedure
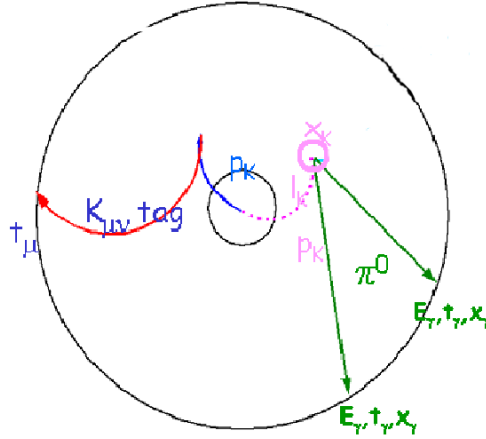
Figure 5.13: The procedure to search the $\pi^0 \to \gamma\gamma$ vertex along the signal kaon path.

we obtain the χ^2 distribution shown in figure 5.14. Once the charged kaon decay vertex has been found we can estimate the kaon proper time:

$$t^* = tof_{cl}^{decay} \cdot \sqrt{1 - \beta^2} \qquad \text{where} \quad \beta = (\beta^{IP} + \beta^{VTX})/2 \tag{5.30}$$

where tof_{cl}^{decay} is signal kaon time of flight, obtained from the selected neutral clusters in the laboratory frame, while β^{IP} and β^{VTX} are the β values of the signal kaon at the interaction point and at the decay vertex, respectively. The kaon β changes due to the energy loss in the different materials and we have estimated that, with the approximation in equation(5.30), we have a systematic underestimate of the order of .65% on the proper time. The beta of the kaon is scaled by a factor 1.0065 according to what has been said in section 5.4.3

We obtain the distribution shown in the figures 5.15 and 5.16. It has to be corrected bin by bin for its reconstruction efficiency and for resolution effects.
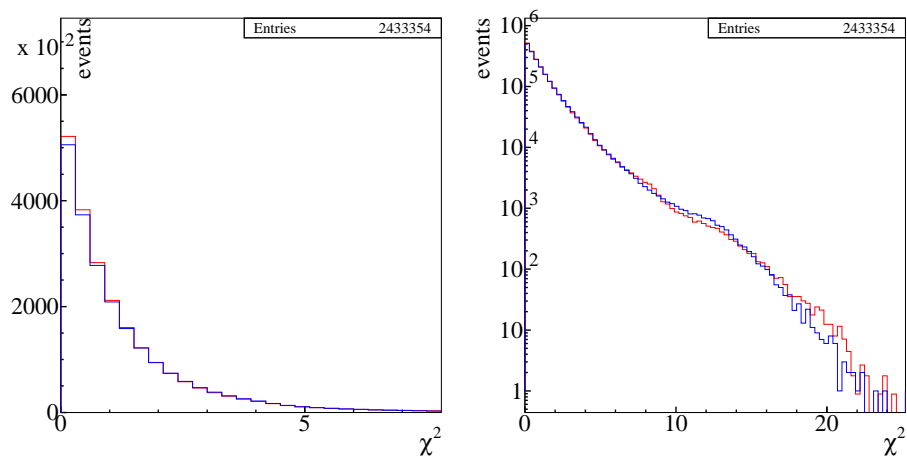
Figure 5.14: χ^2 distribution for data (blue) and for MonteCarlo (red) in linear and in logarithmic scale.
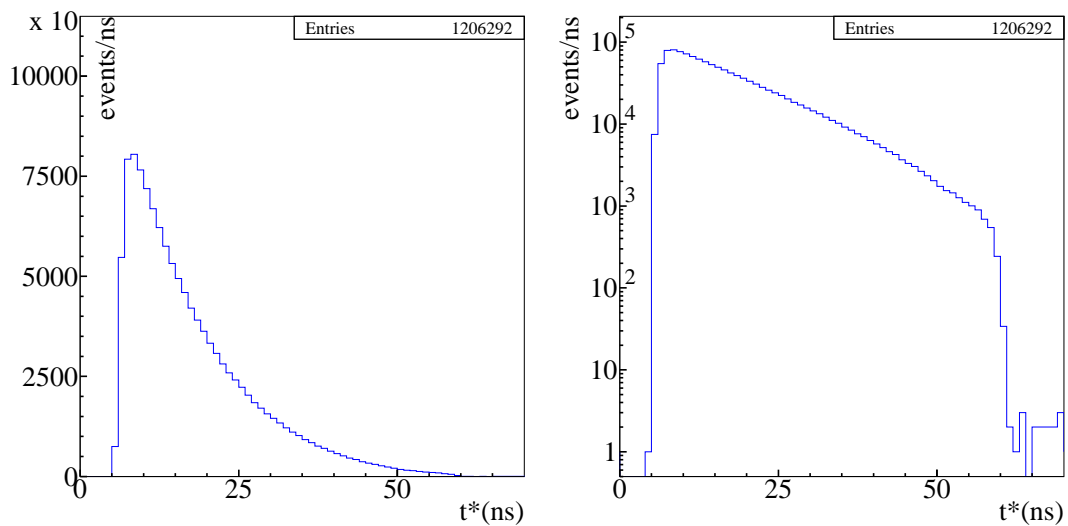
Figure 5.15: Charged kaon proper time distribution in linear and in logarithmic scale, evaluated on MonteCarlo, for the second method.

Figure 5.16: Charged kaon proper time distribution in linear and in logarithmic scale, evaluated on data, for the second method.

Background evaluation

The events used for the evaluation of the charged kaon proper time distribution belong to four families:

1. correctly reconstructed vertices, about 95.5%,

2. vertices reconstructed using photons from different π^0's, ($K^{\pm} \to X \ \pi^0 \ \pi^0$ events), about 2.6%,

3. vertices reconstructed with at least one cluster from a charged particle, about 1.3%,

4. vertices reconstructed with one photon which doesn't come form π^0 decay, about 0.6%.

In figure 5.17 the distributions of the resolution on the charged kaon proper time for the different families, evaluated using MonteCarlo simulation are shown. The main effect of the "backgrounds" is taken into account by properly correcting for the smearing in to the fit.

5.6   Efficiency evaluation

Our purpose is to measure directly on data the reconstruction efficiency of the kaon decay (vertex), as a function of the charged kaon proper time, for both the techniques. In order to do this, as control sample, we use for the first method, in
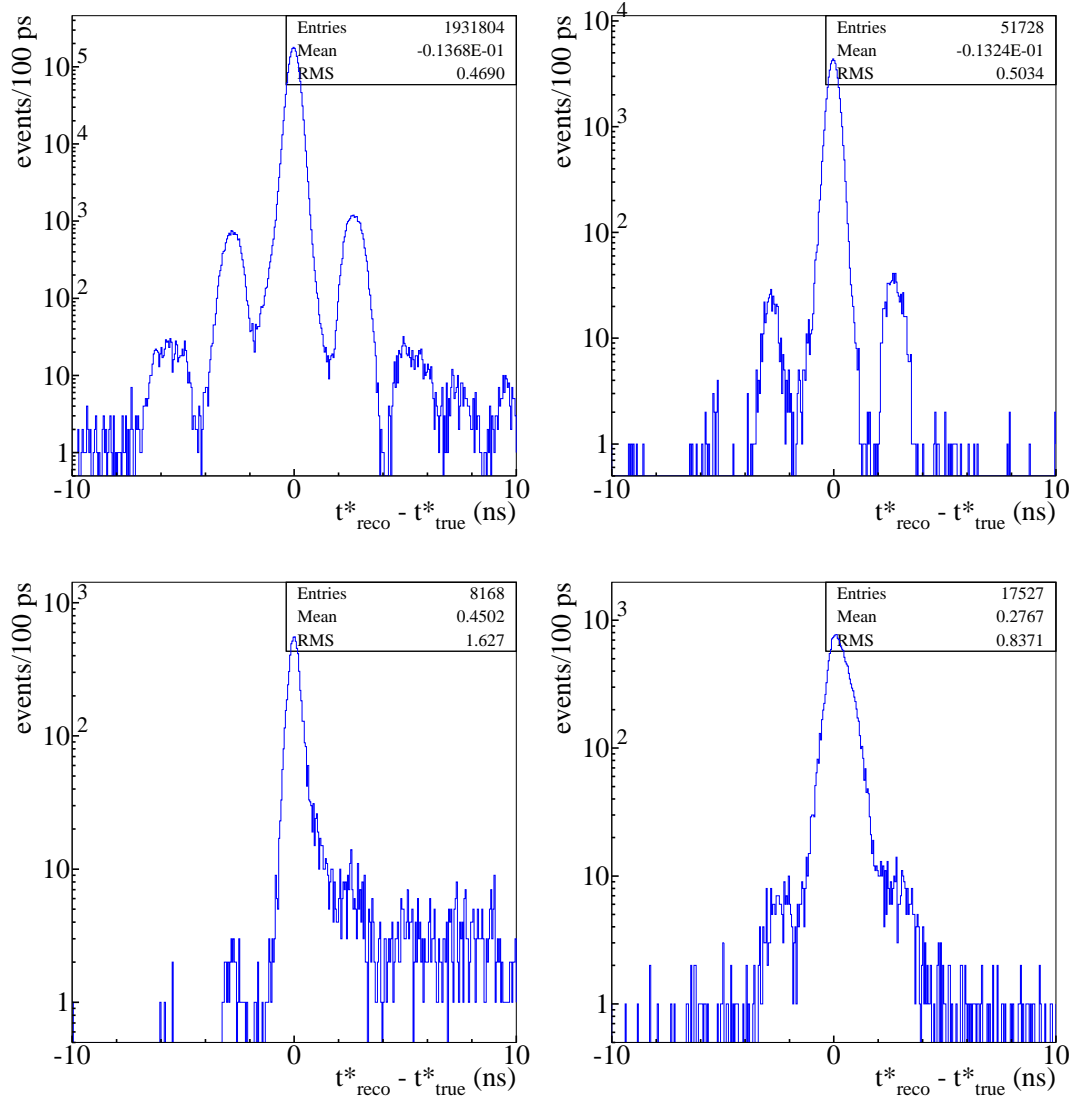
Figure 5.17: Resolution functions for the four families. Above on the left: correctly reconstructed vertices. Above on the right vertices reconstructed using photons from different π^0. Below on the left vertices reconstructed with at least one cluster from a charged particle. Below on the right vertices reconstructed with one photon which doesn't come form π^0 decay.

which the signal is given by events obtained by DC information only, the signal of the second method, obtained using EMC information only; for the second method, in which the signal is given by events obtained by EMC information only, our control sample is given by the signal of the first method.

5.6.1   First method: DC efficiency evaluation

The total reconstruction efficiency of the kaon decay vertex in the DC is given by the product of the reconstruction efficiencies of the charged kaon track, of the charged secondary particle track and of the decay vertex given the two tracks.
Two techniques to evaluate the total reconstruction efficiency can be used. The reconstruction efficiency can be obtained either evaluating the global efficiency (kaon track + secondary track + vertex), or evaluating each separately and then multiplying them. In any case only information from the EMC and from the tagging hemisphere are used and the normalization sample is given by events with a $\pi^0 \to \gamma\gamma$ vertex.

Global kaon decay vertex efficiency

The *global* kaon decay reconstruction efficiency, the global reco efficiency, is defined as:

$$\varepsilon_{\mathrm{reco}}^{\mathrm{G}} = \frac{N_{\pi^0 \& \mathrm{cv}}}{N_{\pi^0}}. \tag{5.31}$$

where N_{π^0} are the events in which a $\pi^0 \to \gamma\gamma$ vertex has been reconstructed and $N_{\pi^0 \& \mathrm{cv}}$ are the events in which a $\pi^0 \to \gamma\gamma$ vertex and a charged vertex, a vertex in the DC, have been reconstructed.
The procedure used to select the normalization sample has been described in the section 5.5.2.
Within the normalization sample we look for a signal kaon track and its decay vertex applying p_K^* cut the previously discussed, see sec 5.5.1.
The efficiency has to be evaluated as a function of the signal kaon proper time, measured along the signal kaon path going from the IP to the $\pi^0 \to \gamma\gamma$ vertex position and accounting for the energy loss in the beam pipe, in the air, in the DC wall and in the DC.
This has been done measuring the efficiency on a MonteCarlo sample treated like data (data-like) of about $175 \ pb^{-1}$ and using a bin size of 1 ns, see picture 5.18.
In order to check the reliability of the method, the efficiency has to be compared with the one obtained using the MonteCarlo simulation, the global true efficiency:

$$\varepsilon_{\mathrm{true}}^{\mathrm{G}} = \frac{\mathrm{N_{cv}}}{\mathrm{N_{Tag}}}. \tag{5.32}$$
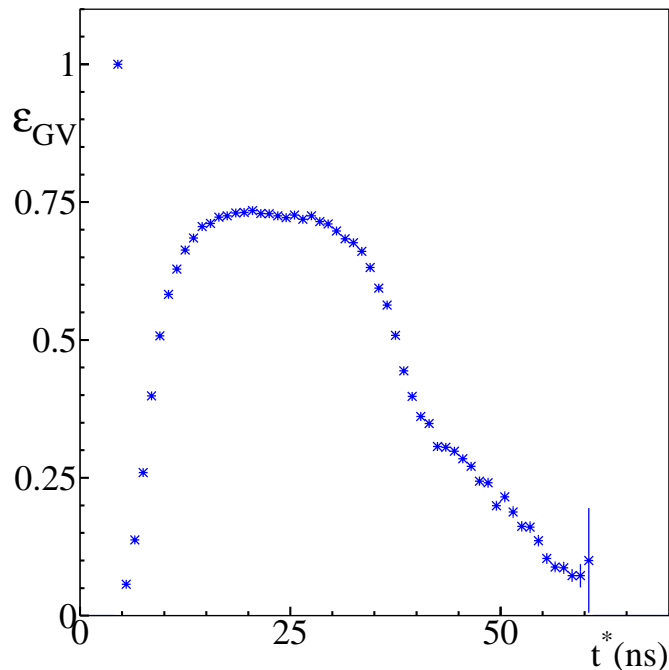
Figure 5.18: Global reco reconstruction efficiency as function of the charged kaon proper time.

where N_{Tag} are the $\phi \to K^+ K^-$ self-triggering tag events and N_{cv} are the events with a reconstructed charged vertex.

In this case the efficiency is measured as a function of the true proper time, defined in section 5.4.3 The distributions of the two efficiencies as a function of the proper time of the kaon are shown in figure 5.19. There is a good agreement between the two distributions. The ratio of the two efficiencies is flat (see fig. 5.20). A linear fit to this ratio, in the region between 12 and 40 ns, gives the following values for the intercept, a_G, and slope, b_G:

$$a_G = (104.4 \pm 0.3) \times 10^{-2}, \tag{5.33}$$
$$b_G = (2.7 \pm 1.4) \times 10^{-4}. \tag{5.34}$$

These two values show an agreement with a residual slope of the order of 10^{-4} for a region of about 30 ns, corresponding to two lifetimes

If we make a linear fit in the region between 15 and 35 ns we obtain the following values (see figure 5.21):

$$a_G = (105.4 \pm 0.4) \times 10^{-2}, \tag{5.35}$$
$$b_G = (-0.8 \pm 1.9) \times 10^{-4}. \tag{5.36}$$
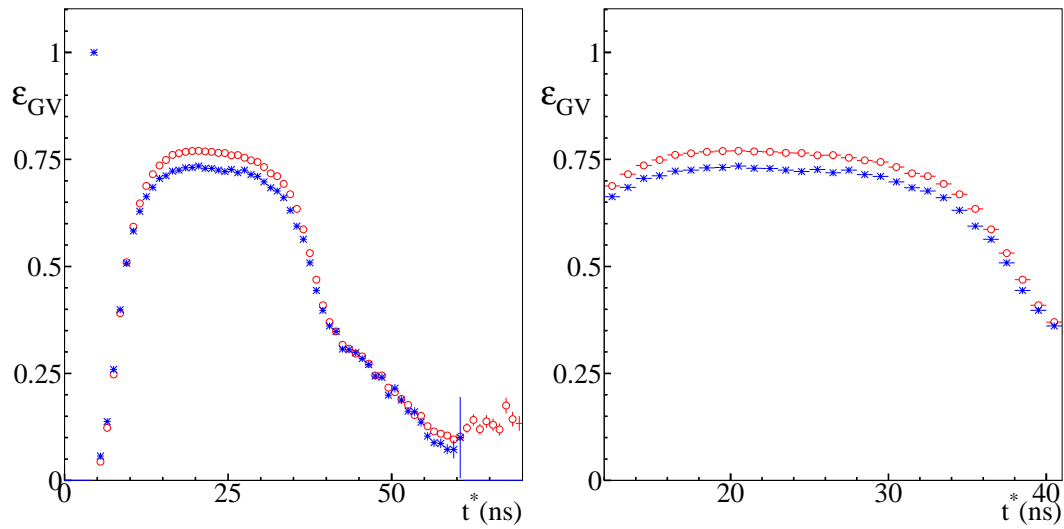
Figure 5.19: Comparison the global reco efficiency (blue) and the global true efficiency (red) as function of the charged kaon proper time.
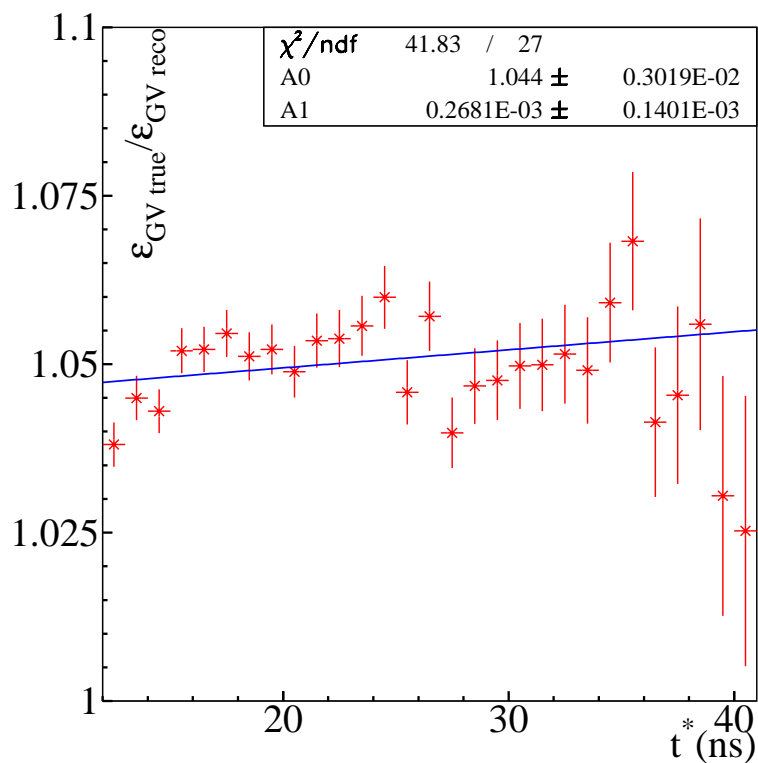
Figure 5.20: Ratio of the global true efficiency over the global reco efficiency as function of the charged kaon proper time between 12 and 40 ns.
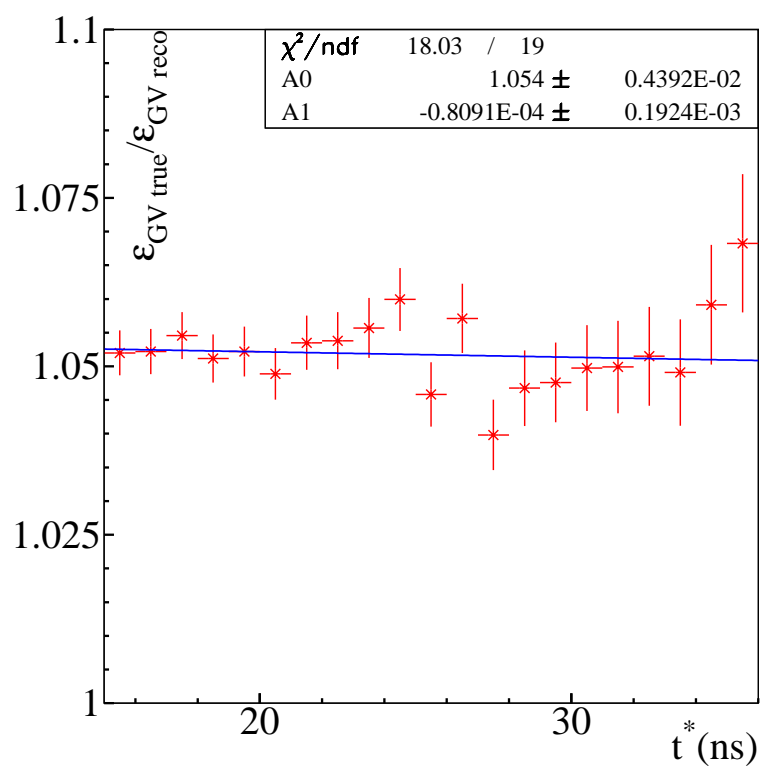
Figure 5.21: Ratio of the global true efficiency over the global reco efficiency, as function of the charged kaon proper time, between 15 and 35 ns.

The 5% underestimate of the reconstruction efficiency is due to the cut in p_K^*; its effect on $K^\pm \to \mu^\pm \overset{(-)}{\nu}_\mu$ events is not properly evaluated using the $\pi^0 \to \gamma\gamma$ vertex technique. Restricting ourselves to events with a π^0 in the final state the two efficiency are in perfect agreement see fig. 5.22 and 5.23.   Anyhow the ratio of the
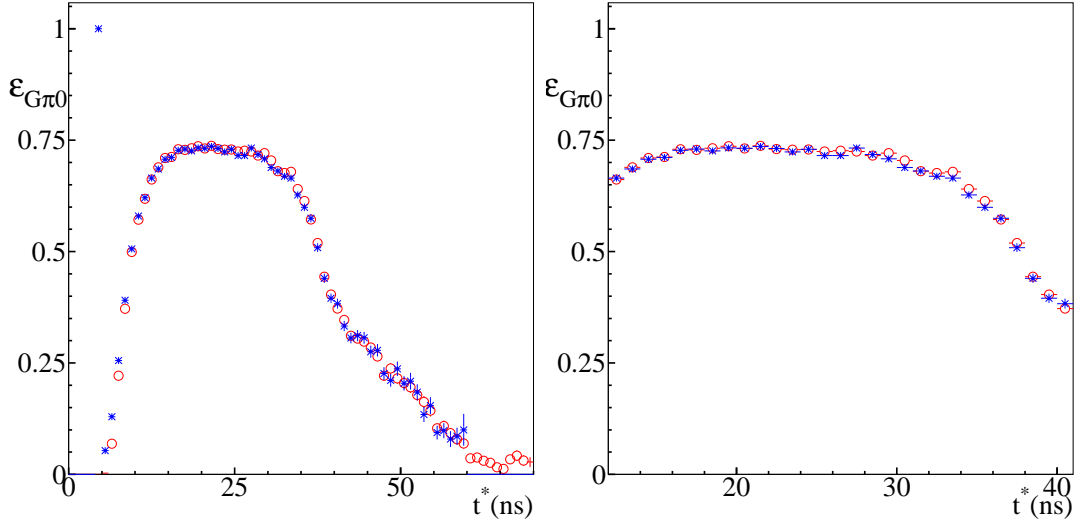
Figure 5.22: Comparison the global reco efficiency (blue) and the global true efficiency (red) as function of the charged kaon proper time, normalized to events in which the kaon decay with a π^0 in the final state.
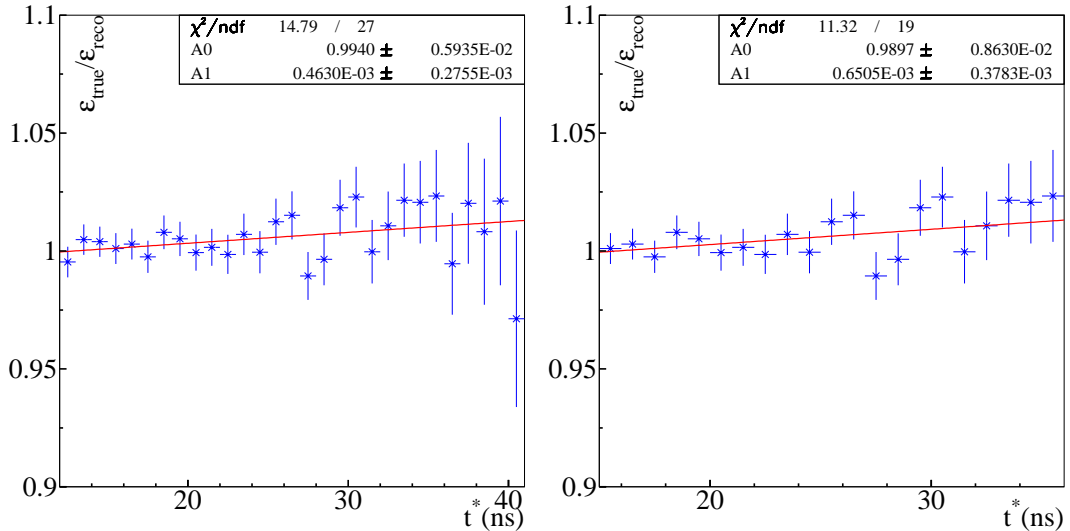
Figure 5.23: Ratio of the global true efficiency over the global reco efficiency of reconstructing the decay vertex of the charged kaon, as function of the charged kaon proper time, normalized to events in which the kaon decay with a π^0 in the final state.

efficiencies is important for the measurement because only the shape of the efficiency is relevant.

Once the reliability of this method has been checked on MC, it is possible to measure the efficiency on data. Using a sample of about of 210 pb^{-1} we obtain the distribution shown in figure 5.24.

The agreement between the efficiency evaluated on data and the efficiency evaluated
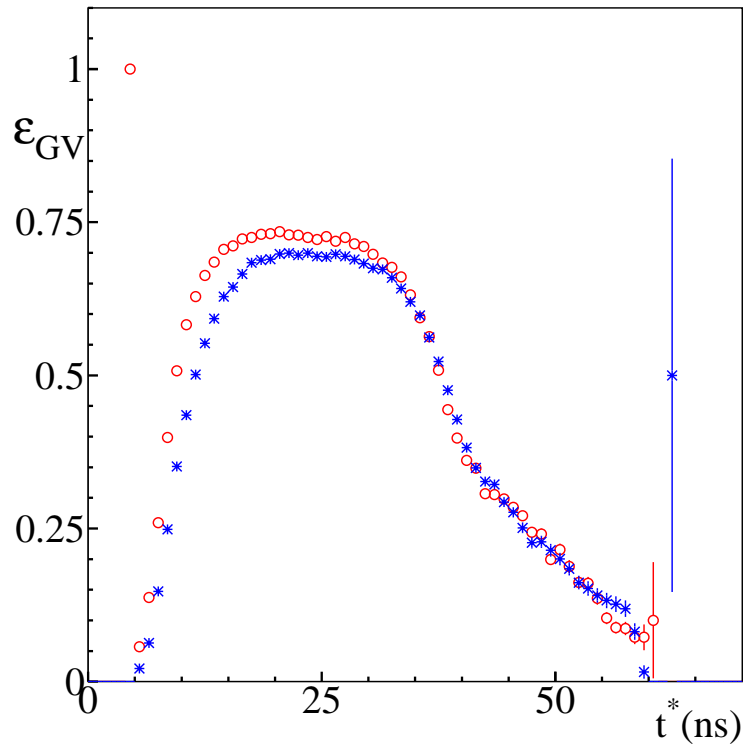
Figure 5.24: Comparison between the global reco efficiency of reconstructing the decay vertex of the charged kaon evaluated on data (blue) and on MonteCarlo data-like (red) as function of the charged kaon proper time.

on MonteCarlo data-like is good except for the region between 8 and 20 ns. This is due to imperfect simulation of the so-called correlated background in the first cells of the DC. In the first 12 layers of the DC a charged kaon loses so much energy that it fires more than a single cell. This sort of background is not well simulated and gives problems in the measurement of the reconstruction efficiency of the kaon track. This effect is shown when we measure the efficiency of reconstruct the track of the charged kaon, see section 5.6.1.

Separated *tracking* **and** *vertexing* **efficiency**

The second technique is based on the evaluation of each efficiency (the reconstruction efficiency of the charged kaon track, *tracking* efficiency, and the reconstruction

efficiency of the charged kaon decay vertex given the kaon track, *vertexing* efficiency) separately. The product of these two efficiencies gives the reconstruction efficiency of the charged kaon decay vertex.

Tracking **efficiency**

The kaon *tracking* efficiency, the tracking reco efficiency, is defined as:

$$\varepsilon_{\text{reco}}^{\text{Trk}} = \frac{N_{\pi^0 \& \text{Trk}}}{N_{\pi^0}}. \tag{5.37}$$

where $N_{\pi^0 \& \text{Trk}}$ are the events in which a $\pi^0 \to \gamma\gamma$ vertex and the signal kaon track have been reconstructed.
The π^0 decay is identified as described in section 5.5.2. The signal kaon track is identified as described is section 5.5.1.
The tracking efficiency is evaluated on a MC data-like sample of about 175 pb^{-1} using a bin size of 1 ns.
Also the method has been validated after the comparison with the true tracking efficiency, defined as:

$$\varepsilon_{\text{true}}^{\text{Trk}} = \frac{N_{\text{Trk}}}{N_{\text{TAG}}}. \tag{5.38}$$

where N_{Trk} are the events in which the kaon track has been reconstructed. The agreement between these two efficiencies is remarkable (see fig. 5.25) as can be seen also in the ratio of the true and reco efficiencies (see fig. 5.26). A linear fit to the ratio, in the region between 12 and 40 ns, gives the following values for the intercept, a_{Trk}, and slope, b_{Trk}:

$$a_{Trk} = (99.62 \pm 0.13) \times 10^{-2}, \tag{5.39}$$
$$b_{Trk} = (-0.3 \pm 5.4) \times 10^{-5}. \tag{5.40}$$

The agreement is very good with a residual slope of the order of 10^{-5} for a region of 30 ns (more than two lifetimes). In the region between 15 and 35 ns we obtain (see figure 5.27):

$$a_{Trk} = (100.0 \pm 0.2) \times 10^{-2}, \tag{5.41}$$
$$b_{Trk} = (-0.13 \pm 0.08) \times 10^{-3}. \tag{5.42}$$
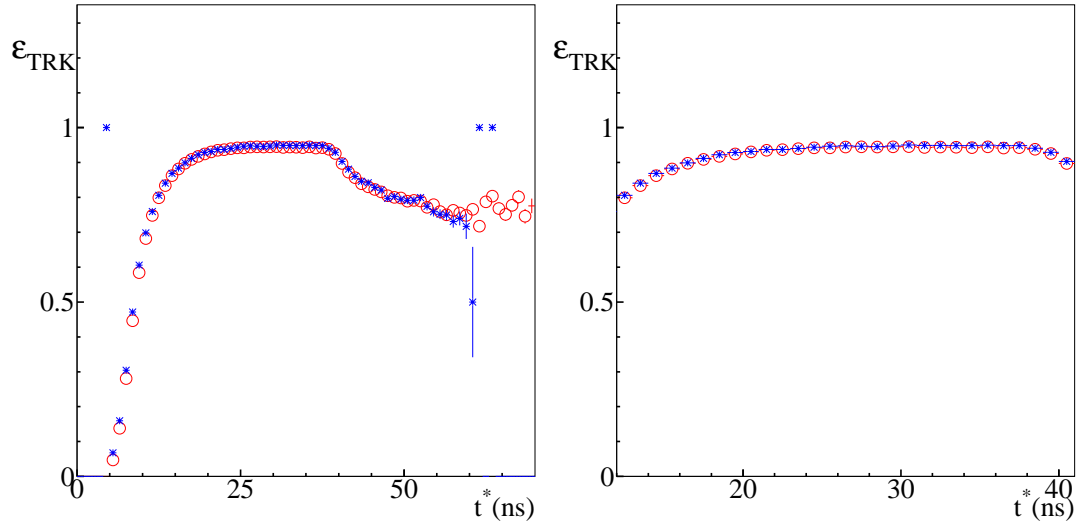
Figure 5.25: Comparison the tracking reco efficiency (blue) and the tracking true efficiency (red) as function of the charged kaon proper time.
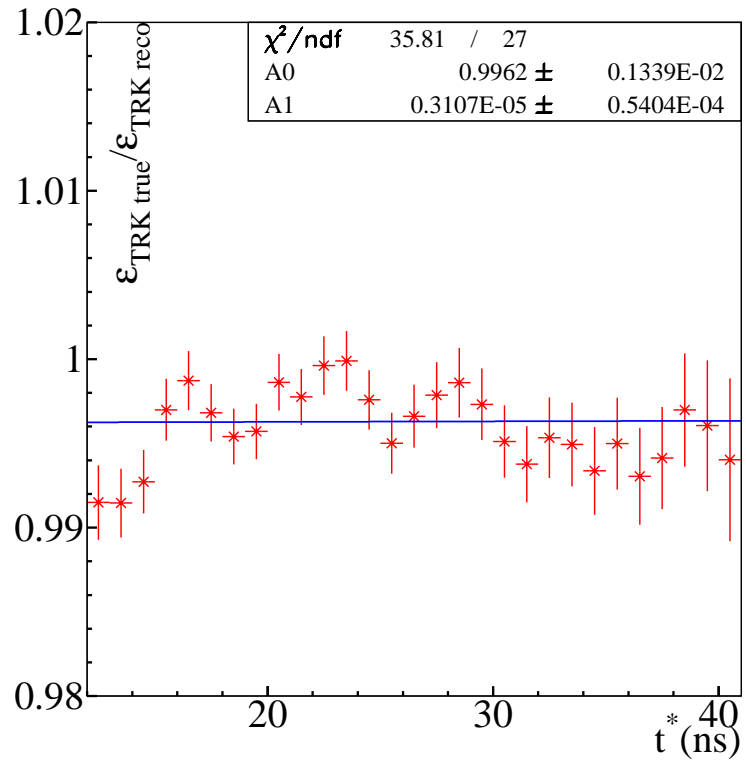
Figure 5.26: Ratio of the tracking true efficiency over the tracking reco efficiency, as function of the charged kaon proper time, between 12 and 40 ns.
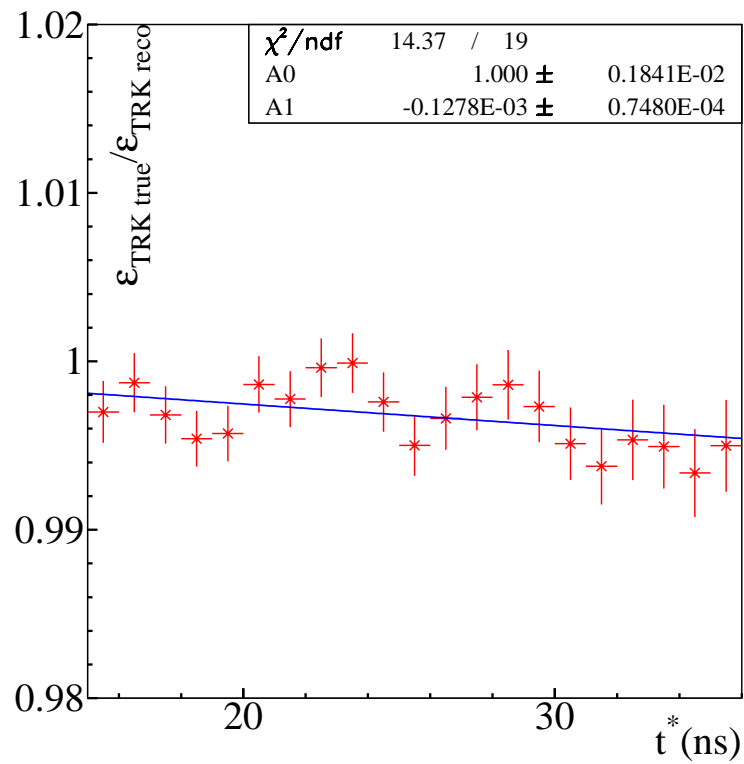
Figure 5.27: Ratio of the tracking true efficiency over the tracking reco efficiency, as function of the charged kaon proper time, between 15 and 35 ns.
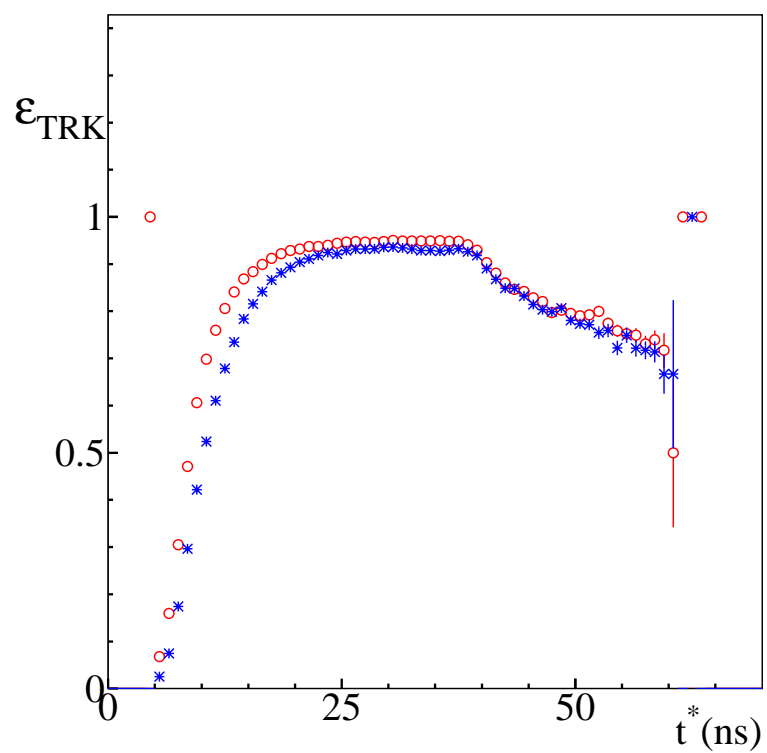
Figure 5.28: Comparison between tracking reco efficiency evaluated on data (blue) and on Monte-Carlo data-like (red) as function of the charged kaon proper time.

This garantees the reliability of the method, and allows its use on data.
Using a sample of about 210 pb^{-1} we obtain the distribution shown in figure 5.28.
The agreement between the efficiency evaluated on data and the efficiency evaluated
on MonteCarlo data-like is good, except for the region between 8 and 20 ns. The
reason for this discrepancy is the same of the analogous discrepancy for the global
efficiency and has been discussed at the end of section 5.6.1.

Vertexing **efficiency**

For the measurement of the reconstruction efficiency of the kaon decay vertex we
have to relay on the DC for the determination of the kaon track. This is the main
difference with respect to the other technique.
The vertexing reco efficiency is defined as:

$$\varepsilon_{\text{reco}}^{\text{Vtx}} = \frac{N_{\pi^0 \& \text{cv}}}{N_{\text{Trk} \& \pi^0}}. \tag{5.43}$$

where $N_{\pi^0 \& \text{cv}}$ are the events in which a $\pi^0 \to \gamma\gamma$ vertex and a charged vertex have
been reconstructed and $N_{\text{Trk} \& \pi^0}$ are the events in which a $\pi^0 \to \gamma\gamma$ vertex and a
charged kaon track have been reconstructed.
For the reconstruction of the $\pi^0 \to \gamma\gamma$ vertex we use the same procedure described in
the section 5.5.2, but we start from the Last Hit of the reconstructed kaon track
instead of starting from the IP. The DC information we use are then the kaon
position and momentum at the Last Hit. We have also to measure the $\text{tof}_K^{\text{decay}}$ for the
π^0 decay reconstruction, then we measure the time of flight of the charged kaon along
the track, from the IP to the Last Hit, $\text{tof}_{F_h L_h}$. Then we extrapolate the signal kaon
track up to a maximum value of one meter, backward and forward, looking for the π^0
decay vertex and using the following relations:

$$tof_K^{decay} = tof_{F_h L_h} - tof_{bwd} \tag{5.44}$$

or

$$tof_K^{decay} = tof_{F_h L_h} + tof_{fwd}. \tag{5.45}$$

We use this $\text{tof}_K^{\text{decay}}$ in eq 5.22 for the search of the $\pi^0 \to \gamma\gamma$ vertex. Since the
efficiency has to be function of the charged kaon proper time, we have to measure the
kaon proper time along the track, from the IP to the Last Hit, $t_{F_h L_h}^*$. Therefore if we
extrapolate the signal kaon track backward or forward, looking for the $\pi^0 \to \gamma\gamma$
vertex, we have:

$$t^* = t_{F_h L_h}^* - t_{bwd}^* \tag{5.46}$$

or

$$t^* = t^*_{F_h L_h} + t^*_{fwd}. \tag{5.47}$$

To evaluate the *vertexing* efficiency we have used a MonteCarlo data-like sample of about 175 pb^{-1}, using a bin size of 1 ns. As usual the efficiency is compared with the one obtained on MC truth.

This is defined as the ratio of the events in which the kaon decay vertex has been reconstructed (N_{Vtx}) over the events in which the kaon track has been reconstructed (N_{Trk}):

$$\varepsilon^{\mathrm{Vtx}}_{\mathrm{true}} = \frac{\mathrm{N_{Vtx}}}{\mathrm{N_{Trk}}}. \tag{5.48}$$

In this case we have evaluated the efficiency as a function of the proper time given by the MonteCarlo simulation, the true proper time.

The comparison between these two efficiencies is shown in figure 5.29. As can be seen
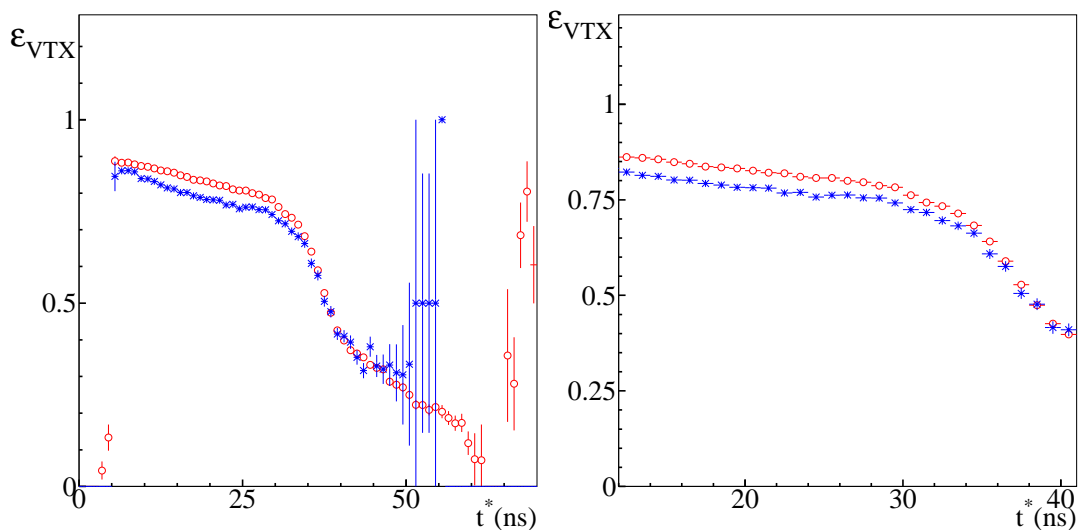
Figure 5.29: Comparison between the vertexing reco efficiency (blue) and the vertexing true efficiency (red) as function of the charged kaon proper time.

from the ratio of these efficiencies, shown in figure 5.30, there is a very satisfactory agreement between the two. Making a linear fit in the region between 12 and 40 ns, the values for the intercept, a_{Vtx}, and slope, b_{Vtx}, are:

$$a_{Vtx} = (106.2 \pm 0.6) \times 10^{-2}, \tag{5.49}$$
$$b_{Vtx} = (-4. \pm 3.) \times 10^{-4}. \tag{5.50}$$
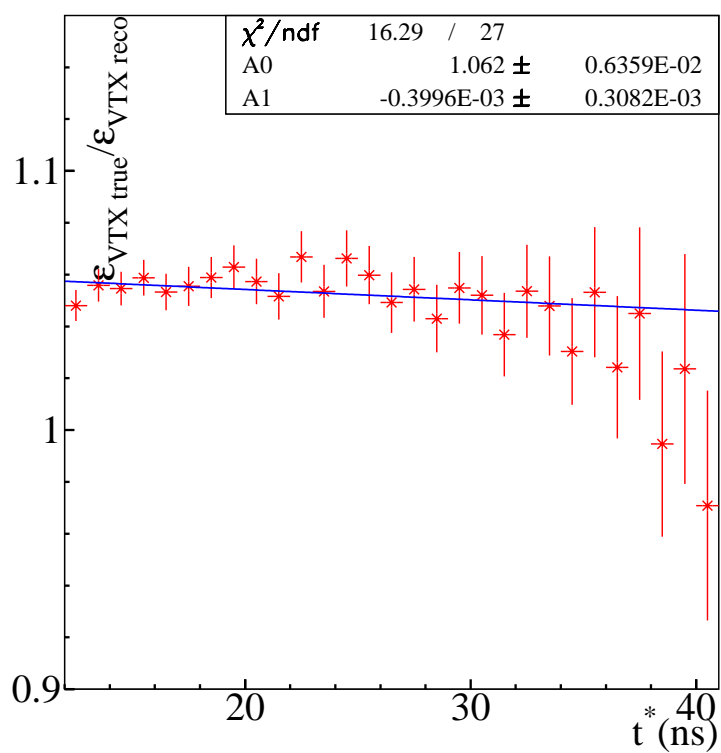
Figure 5.30: Ratio of the vertexing true efficiency over the vertexing reco efficiency, as function of the charged kaon proper time, between 12 and 40 ns.

The agreement is fine with a residual slope of the order of 10^{-4} for a region of 30 ns, more than two lifetimes.

Restricting the linear fit to the region between 15 and 35 ns we obtain (see figure 5.31):

$$a_{Vtx} = (106.8 \pm 1.0) \times 10^{-2}, \tag{5.51}$$

$$b_{Vtx} = (-6. \pm 4.) \times 10^{-4}. \tag{5.52}$$
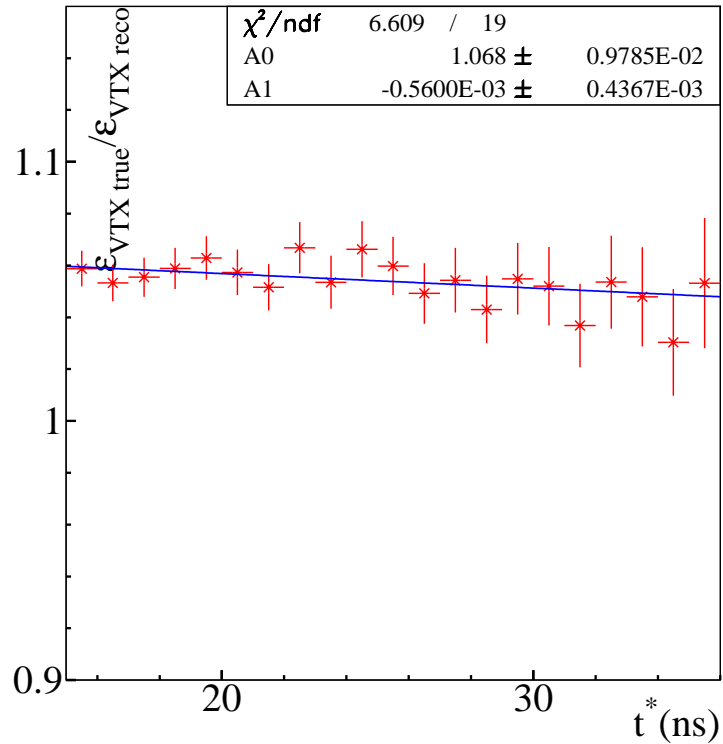
Figure 5.31: Ratio of the vertexing true efficiency over the vertexing reco efficiency, as function of the charged kaon proper time, between 15 and 35 ns.

The next step is the measurement of the vertex efficiency on the data sample. We use a sample of about of 210 pb^{-1} and we obtain the distribution shown in figure 5.32. The agreement between the efficiency evaluated on data and the efficiency evaluated on MonteCarlo data-like is very good, see figure 5.32.

We also made a background analysis with the MonteCarlo simulation and we have estimated that there is a $K^{\pm} \to \mu^{\pm} \overset{(-)}{\nu}_{\mu}$ background in our $\pi^{o} \to \gamma\gamma$ technique of the order of 0.2%. In these events the two clusters selected are due to the machine background. These events do not represent a significant bias for our efficiency measurement.
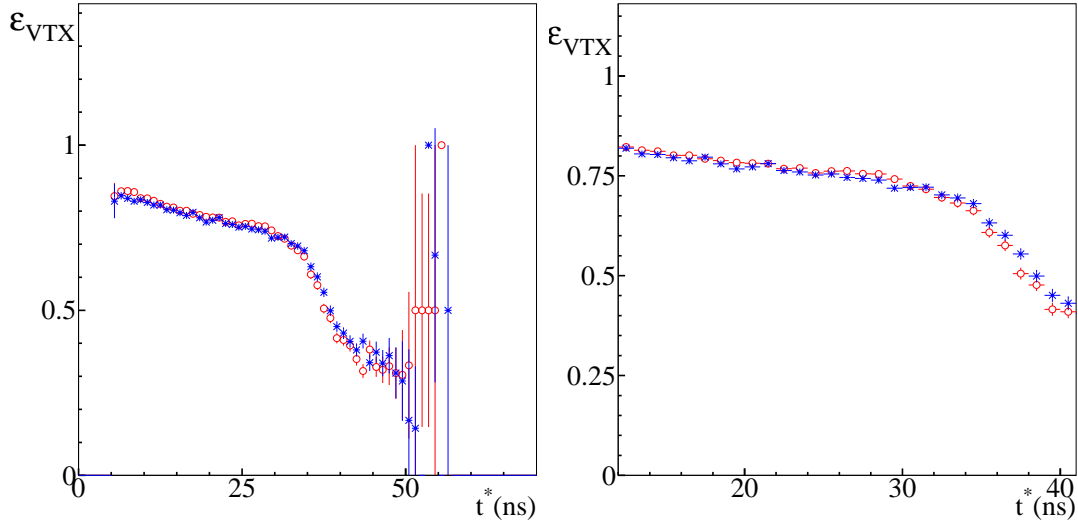
Figure 5.32: Comparison the vertexing reco efficiency evaluated on data (blue) and on MonteCarlo data-like (red) as function of the charged kaon proper time.

Two techniques compared

We compared, on the MonteCarlo data-like sample, the efficiency obtained in the section 5.6.1, the *global* kaon decay vertex efficiency, and the efficiency given by the product of the kaon *tracking* efficiency and kaon *vertexing* efficiency, obtained in section 5.6.1 and 5.6.1 Although the two methods are not completely independent, since both rely on the $\pi^0 \to \gamma\gamma$ technique, it is worth to compare the overall efficiency obtained in the two approaches. For the *global* approach we used only extrapolation of the tagging information in finding the π^0 decay vertex; for the second approach we used the measured track in finding the π^0 decay vertex, and is expected to have a better resolution. The agreement between the two efficiencies is exccelent. This is confirmed by the bin by bin ratio of the two (fig. 5.34) and the result of a linear fit to this ratio in the region between 12 and 42 ns, giving the following values for the intercept, a_G, and slope, b_G:

$$a_G = (99.3 \pm 0.6) \times 10^{-2}, \tag{5.53}$$

$$b_G = (6 \pm .3) \times 10^{-4}. \tag{5.54}$$

Restricting the linear fit to the region between 15 and 35 ns we obtain the following values (see figure 5.34):

$$a_G = (99.4 \pm 1.0) \times 10^{-2}, \tag{5.55}$$

$$b_G = (5. \pm 4.) \times 10^{-4}. \tag{5.56}$$
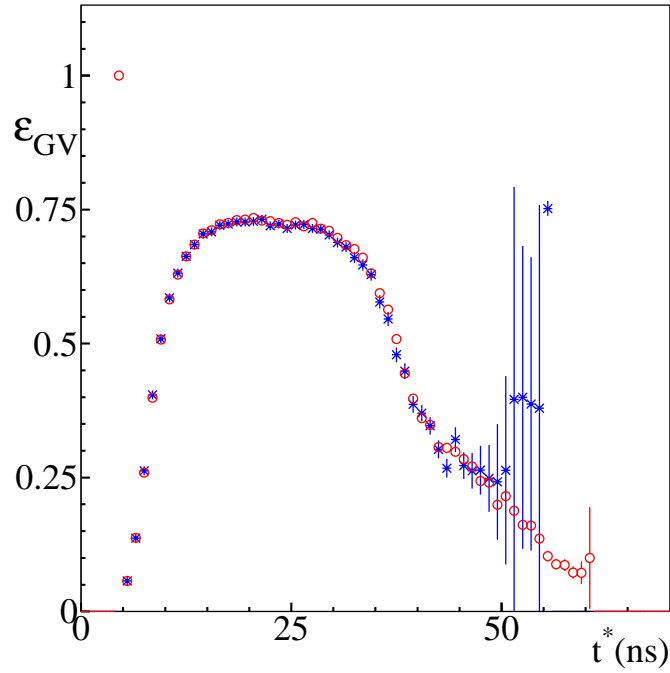
Figure 5.33: Comparison the *global* reco efficiency (blue) and efficiency given by the product of the kaon *tracking* efficiency and kaon *vertexing* efficiency (red) as function of the charged kaon proper time, on MonteCarlo.
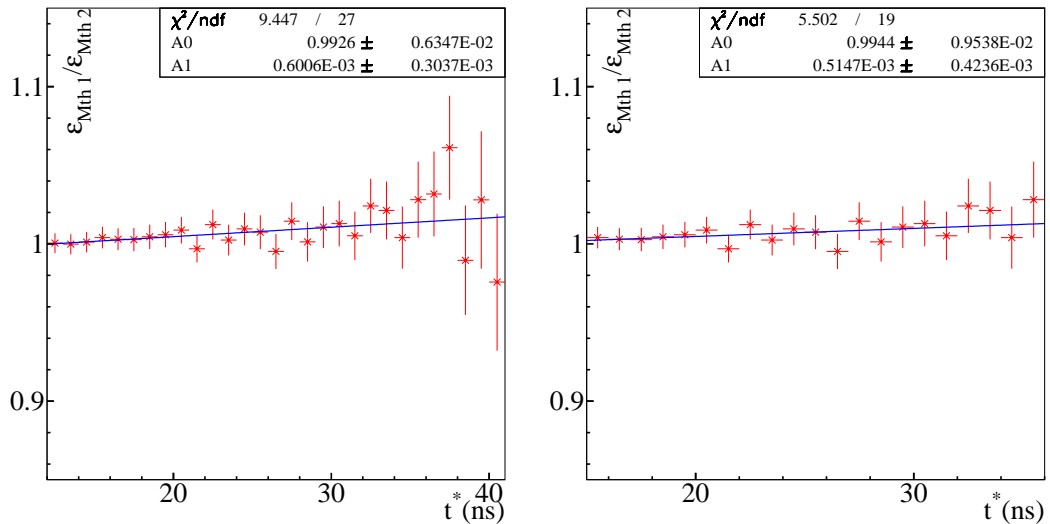
Figure 5.34: Ratio of the global reco efficiency over the efficiency given by the product of the kaon tracking efficiency and kaon vertexing efficiency, as function of the charged kaon proper time, evaluated on MonteCarlo.

We obtained good result also on the data sample, as shown in figure 5.35. It is
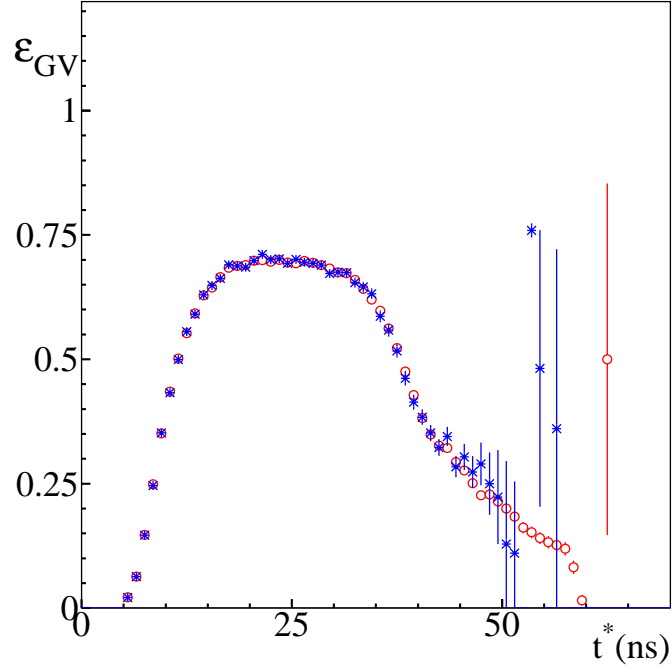
Figure 5.35: Comparison the *global* reco kaon efficiency (blue) and the efficiency given by the product of the kaon *tracking* efficiency and kaon *vertexing* efficiency (red) as function of the charged kaon proper time, on data.

confirmed by the bin by bin ratio of the two (fig. 5.36) and by the result of a linear fit to this ratio in the region between 12 and 40 ns. The linear fit gives the following values for the intercept, a_G, and slope, b_G:

$$a_G = (99.3 \pm 0.7) \times 10^{-2}, \tag{5.57}$$
$$b_G = (2. \pm 3.) \times 10^{-4}. \tag{5.58}$$

While if we make a linear fit in the region between 15 and 35 ns we obtain the following values (see figure 5.35):

$$a_G = (99.3 \pm 1.0) \times 10^{-2}, \tag{5.59}$$
$$b_G = (2 \pm 4.) \times 10^{-4}. \tag{5.60}$$
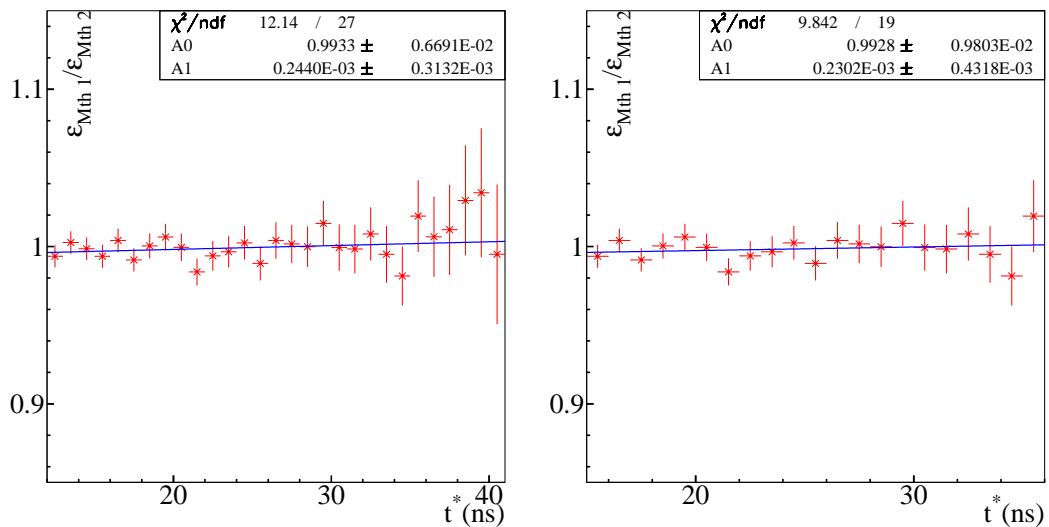
Figure 5.36: Ratio of the global reco efficiency of reconstructing the decay vertex of the charged kaon and efficiency given by the product of the kaon tracking efficiency and kaon vertexing efficiency, as function of the charged kaon proper time, evaluated on the data sample.

5.6.2 Second method: $\pi^0 \to \gamma\gamma$ vertex efficiency evaluation

In order to measure the kaon decay vertex reconstruction efficiency, using EMC information only, the π^0 reco efficiency, we have used as normalization sample the events in which the charged decay vertex, the vertex given by two tracks in the DC, has been reconstructed. The normalization sample is given by the signal sample for the first method, see section (5.5.1).

The π^0 reco efficiency is defined, bin by bin, as the ratio between the number of events with the kaon charged decay vertex (N_{cv}) as denominator and the number of events in which the $\pi^0 \to \gamma\gamma$ vertex has been reconstructed, given the existence of the *charged* vertex, ($N_{cv\&\pi^0}$), as numerator:

$$\varepsilon_{\text{reco}}^{\pi^0} = \frac{N_{\&cv\&\pi^0}}{N_{cv}}. \tag{5.61}$$

In order to check the reliability of the described method, this efficiency has to be compared with the true one defined as the ratio of the events with a reconstructed $\pi^0 \to \gamma\gamma$ vertex, (N_{π^0}) over the $\phi \to K^+ K^-$ self-triggering tag events:

$$\varepsilon_{\text{true}}^{\pi^0} = \frac{N_{\pi^0}}{N_{\text{Tag}}}. \tag{5.62}$$

In this case the efficiency is measured as a function of the true proper time, the proper time given by the MonteCarlo simulation. We measured the $\pi^0 \to \gamma\gamma$
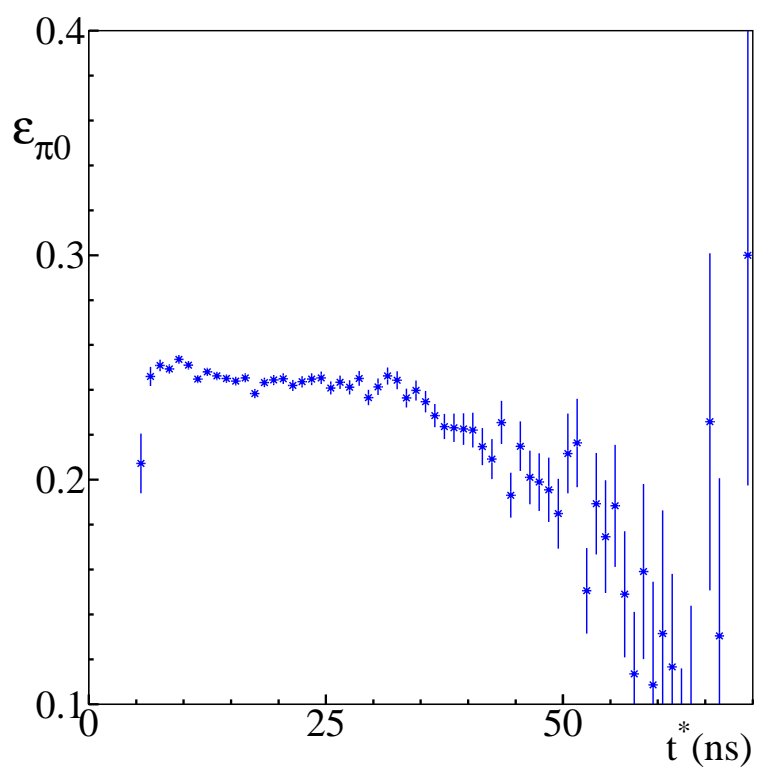
Figure 5.37: π^0 reco efficiency as a function of the charged kaon proper time.

efficiency on a MonteCarlo data-like sample of about 175 pb^{-1} using a bin size of 1 ns. The distributions of the expected and measured efficiencies as a function of the proper time of the kaon are shown in figure 5.38. There is a good agreement between
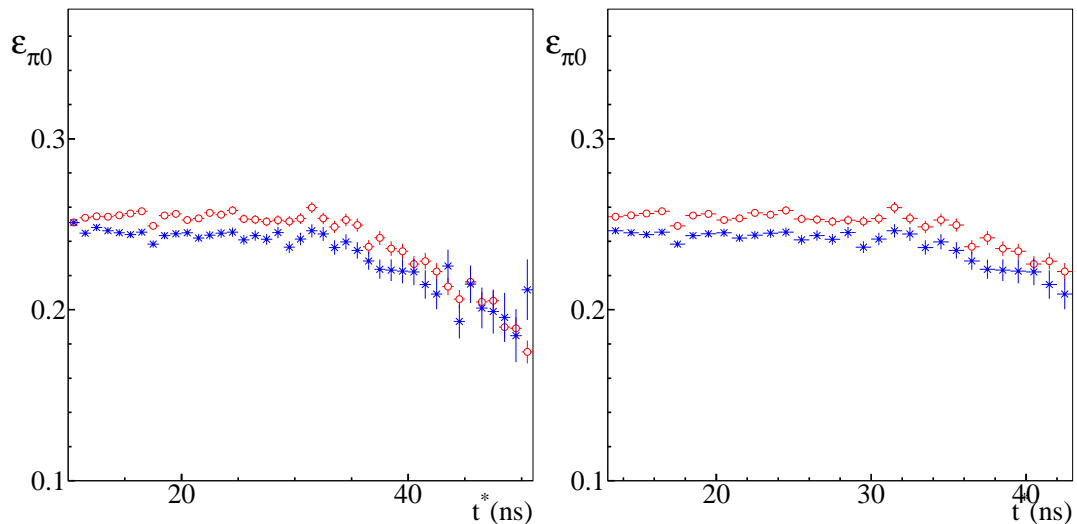
Figure 5.38: Comparison the π^0 reco efficiency of reconstructing the $\pi^0 \to \gamma\gamma$ vertex of the charged kaon (blue) and the π^0 true efficiency of reconstructing the $\pi^0 \to \gamma\gamma$ vertex of the charged kaon (red) as function of the charged kaon proper time. In the figure on the left the two efficiencies are normalized to the unity in the region between 10 and 50 ns, in the figure on the right the two efficiencies are normalized to the unity in the region between 12 and 43 ns

the two efficiencies. It is confirmed by the bin by bin ratio of the two (fig. 5.39) and by the result of a linear fit to this ratio in the region between 10 and 50 ns:

$$a_{\pi^0} = (102.6 \pm 0.7) \times 10^{-2}, \tag{5.63}$$
$$b_{\pi^0} = (7. \pm 3.) \times 10^{-4}. \tag{5.64}$$

The agreement is fine with a residual slope of the order of 10^{-4} for a region of 40 ns, about three lifetimes.
Doing a linear fit between 13 and 42 ns (fig 5.40) we obtain:

$$a_{\pi^0} = (103.7 \pm 1.0) \times 10^{-2}, \tag{5.65}$$
$$b_{\pi^0} = (4. \pm 4.) \times 10^{-4}. \tag{5.66}$$

The agreement is very good with a residual slope of the order of 10^{-4} for a region of about 30 ns, about two lifetime, see figure 5.40. The reason for overestimate of the efficiency is in the normalization used for the reconstructed efficiency: the control
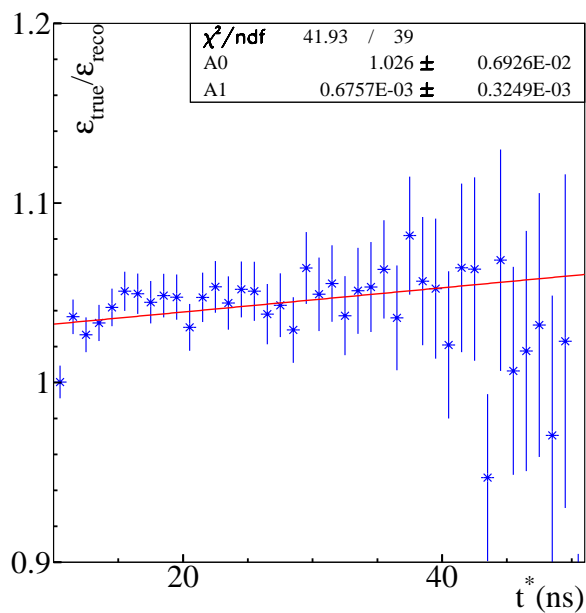
Figure 5.39: Ration of the π^0 true efficiency over the π^0 reco efficiency of reconstructing $\pi^0 \to \gamma\gamma$ decay vertex, as function of the charged kaon proper time, between 10 and 50 ns.
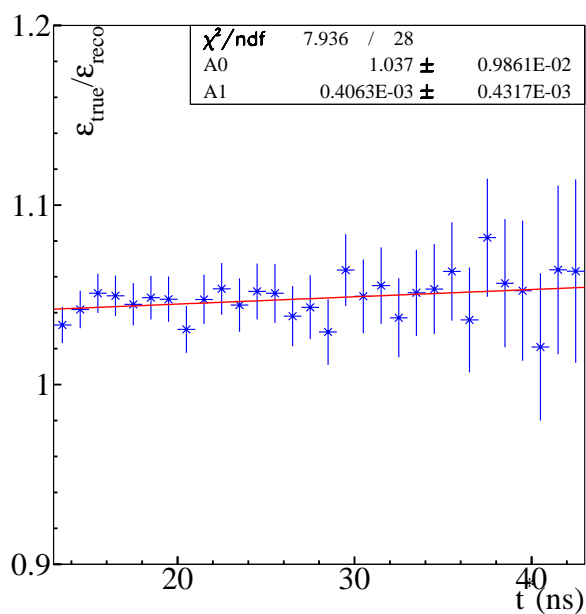
Figure 5.40: Ratio of the π^0 true efficiency over the π^0 reco efficiency of reconstructing the $\pi^0 \to \gamma\gamma$ vertex, as function of the charged kaon proper time, between 13 and 42 ns.

sample is given by the number of events in which a charged vertex has been reconstructed without any information on the particular final state. Indeed restricting ourselves only to events with a π^0 in the final state the two efficiency are in perfect agreement: the shape and the overall scale of the efficiencies are correctly evaluated, see figure 5.41.
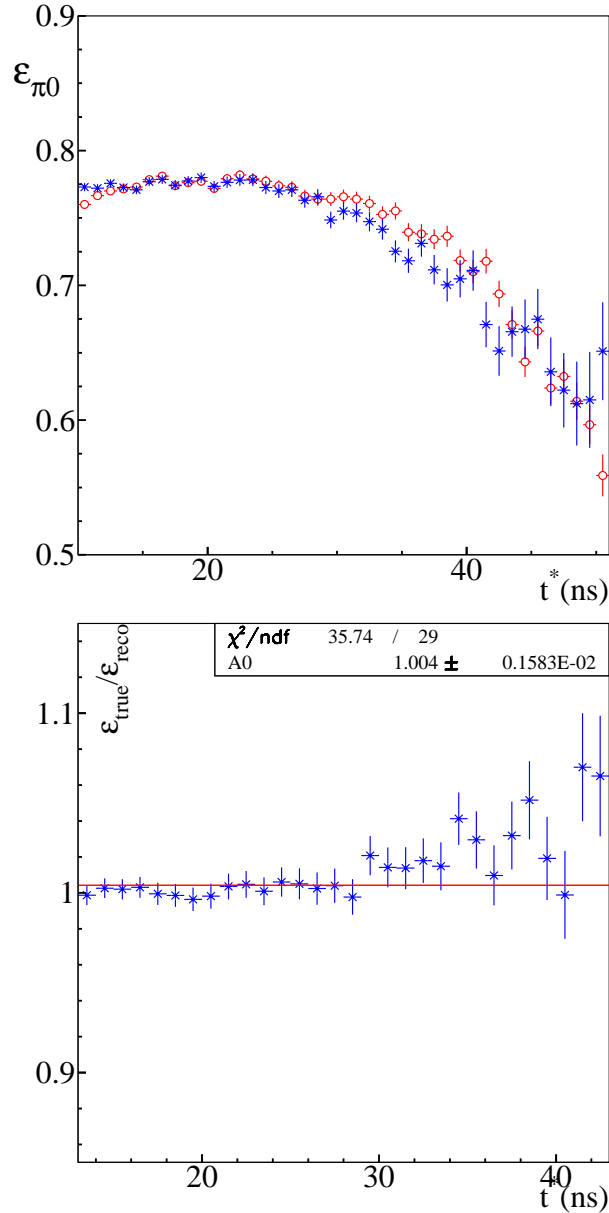
Figure 5.41: Above: the comparison the π^0 reco efficiency (blue) and the π^0 true efficiency (red) as function of the charged kaon proper time, restricting ourselves to events with a π^0 in the final state for the normalizations. Below: the ratio of the π^0 true efficiency over the π^0 reco efficiency, both normalized to events with a π^0 in the final state.

Having demostrated with the MonteCarlo simulation the reliability of this method for measuring the efficiency, we can proceed in measuring it on data. We used a sample of 210 pb^{-1} and we obtain the distribution shown in figure 5.42. The agreement
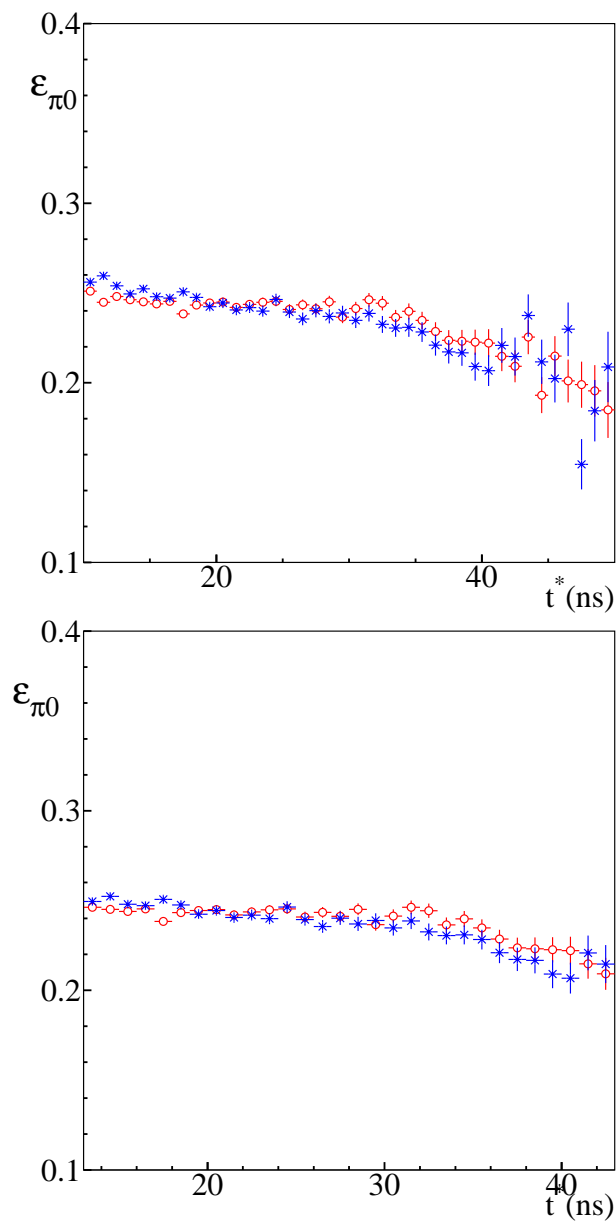
Figure 5.42: Comparison the π^0 reco efficiency of reconstructing the $\pi^0 \to \gamma\gamma$ vertex evaluated on data (blue) and on MonteCarlo data-like (red) as function of the charged kaon proper time.

between the efficiency evaluated on data and the efficiency evaluated on MonteCarlo data-like is good.

5.7 Resolution effects

So far we have obtained the proper time distribution and evaluated the efficiency of reconstructing the kaon decay vertex as function of the proper time, for both the methods. In order to perform the exponential fit to the proper time distribution, we need to take into account the resolution effects. Some events in the proper time distribution are generated with a given value but are reconstructed with another one for resolution effects.

We need to evaluate these resolution effects and then we can perform the fit using a function given by the convolution of the exponential decay behavior and the resolution function.

5.7.1 First method: evaluation of resolution

We have to determine the resolution curves for the signal sample of the first method. These are evaluate with the MonteCarlo simulation and are defined as the difference between the true proper time, see section 5.4.2, and charged kaon proper time. First of all we have to emphasize that also the resolution curves are functions of the charged kaon proper time. For example the resolution curve for charged kaon proper time between 8 and 10 ns is different from the one for charged kaon proper time between 20 and 21 ns, as shown in figure 5.43. In order to be less sensitive to the
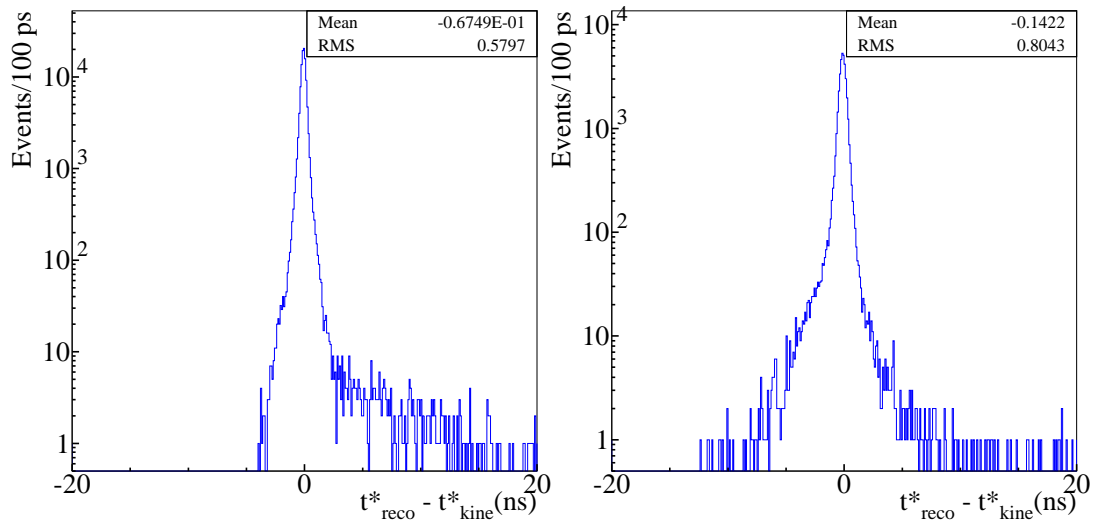
Figure 5.43: Left. Resolution curve for charged kaon proper time between 8 and 10 ns. Right. Resolution curve for charged kaon proper time between 20 and 22 ns.

MonteCarlo simulation, we decided to measure the resolution curves directly on data. This is possible using the point of closest approach (PCA) between the kaon track and the charged particle track. The PCA is found minimizing the distance between

the helixes built starting from the two tracks and accounting for the energy loss in the DC: the kaon helix is built using the kaon last hit position and momentum, the charged secondary helix is built using its last hit position and momentum. To validate this technique we use the MonteCarlo simulation. We can evaluate with this technique the position and momentum of thekaon at the decay vertex and compare these values with the true ones givenby the simulation. As we can see in the figures 5.44 and5.45, we obtain very good results. Therefore we can estimate the charged
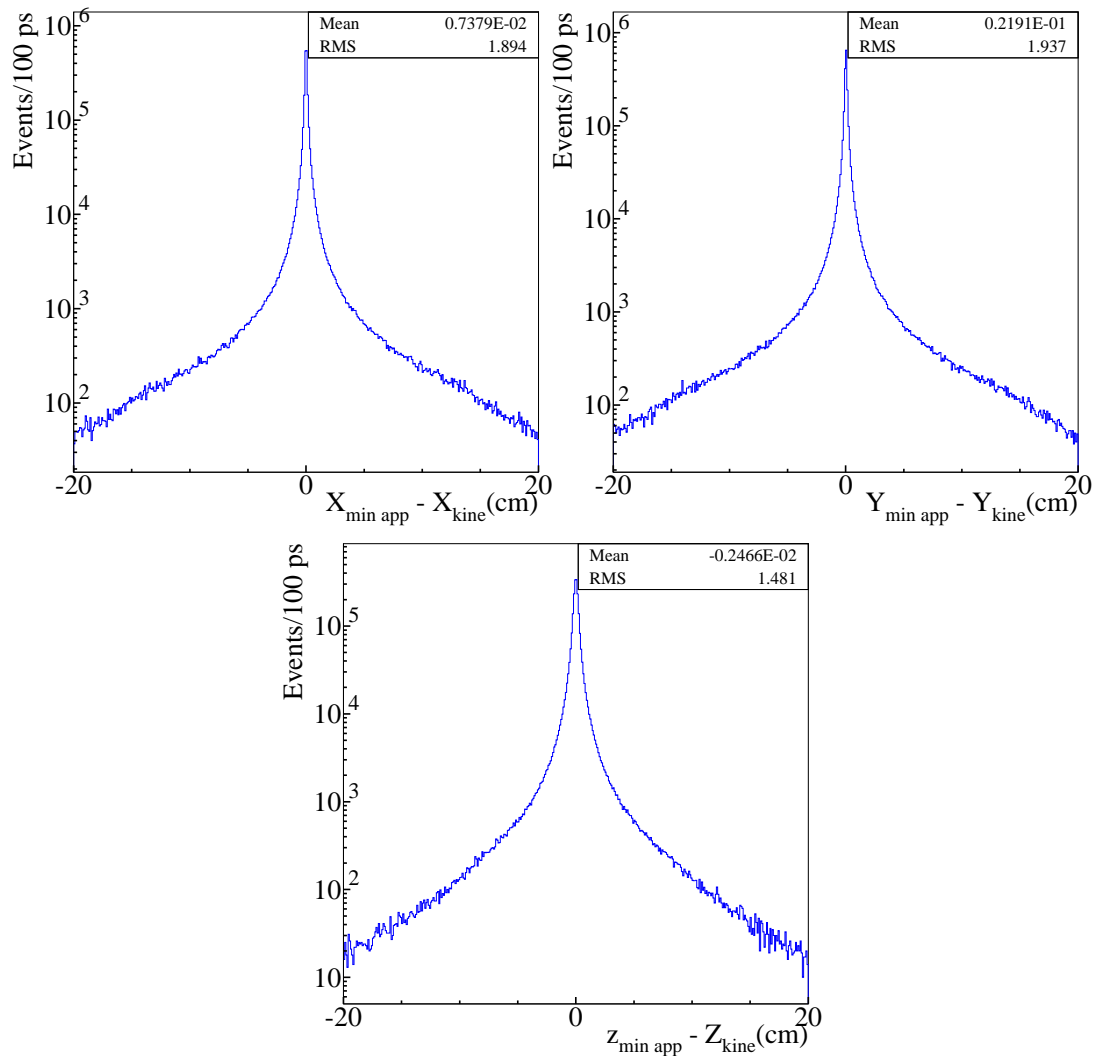
Figure 5.44: Resolution curves given by the minimum approach technique for charged kaon position along the x, y and z axis.

kaon proper time using the stepping procedure, from the IP to the point of closest approach between the kaon and the charged secondary tracks, and taking into account the energy loss given by the Bethe-Bloch formula. The proper time
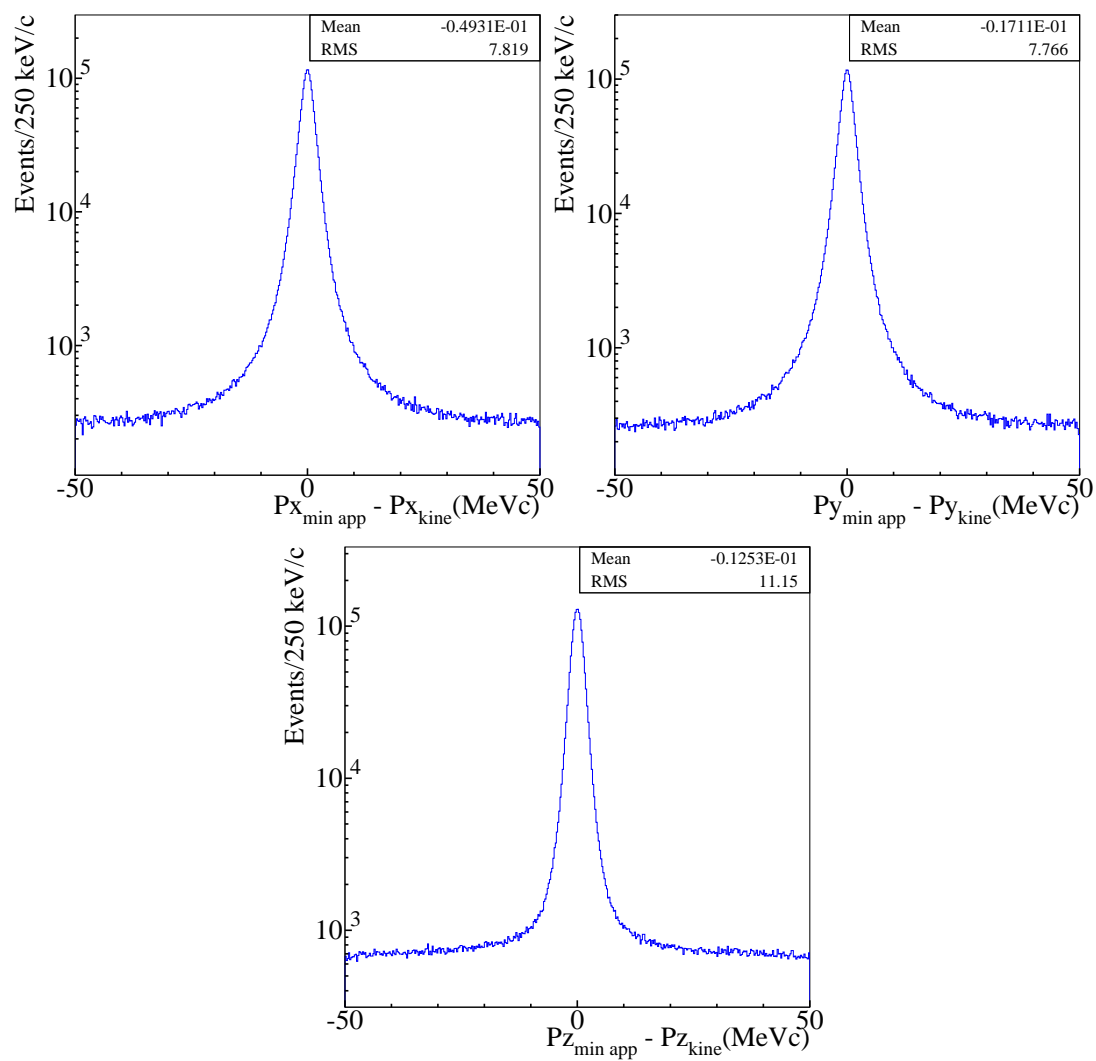
Figure 5.45: Resolution curves given by the minimum approach technique for charged kaon momentum along the x, y and z axis.
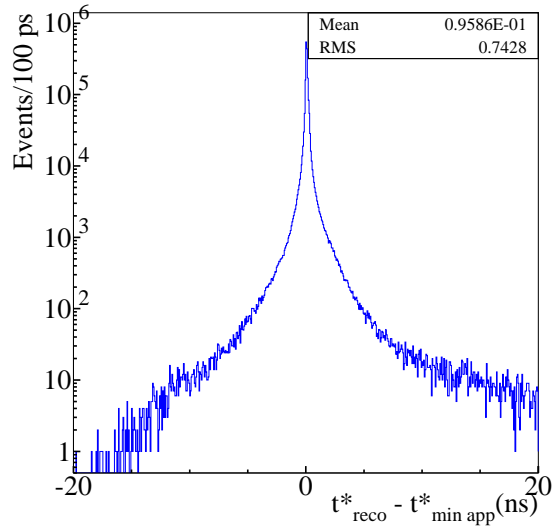
Figure 5.46: Proper time resolution curve given by the minimum approach technique evaluated on MonteCarlo data-like.

resolution curve is then defined as the distribution given by the difference between the charged kaon proper time estimated using the point of closest approach and the one obtained using the reconstructed decay vertex in the DC. We obtain the distribution shown in the figure 5.46. For each bin of the $K^\pm$ proper time a different resolution curve is measured.

It 's important to emphasize that this technique can be used also on data and the obtained distribution is shown in figure 5.47. We can also compare the proper time resolution curves obtained for data and MonteCarlo data-like samples, the results is shown in figure 5.48. For the fit to the proper time distribution we use the true resolution functions corrected by the ratio of the resolution function obtained with the PCA technique evaluated on data and on MC data-like:

$$Res_{\text{data}} = Res_{\text{true}} \times \frac{Res_{\text{PCA}}(data)}{Res_{\text{PCA}}(MC)}. \tag{5.67}$$

5.7.2   Second method: evaluation of resolution

As for the first method the resolution functions depend on the charged kaon proper time, see figure 5.49. The peaks visible at ± 2.7 and ± 5.4 ns are due to wrong determinations of the bunch giving the global T_ϕ^0 of the event, that gives a wrong value of the ϕ meson decay time. Also for this method, in order to be less sensitive to the MonteCarlo simulation, we implemented a technique to smear by data the resolution functions evaluated using the MonteCarlo simulation. We define the $\gamma\gamma$ resolution curves, shown in figure 5.50, as the difference between the charged kaon
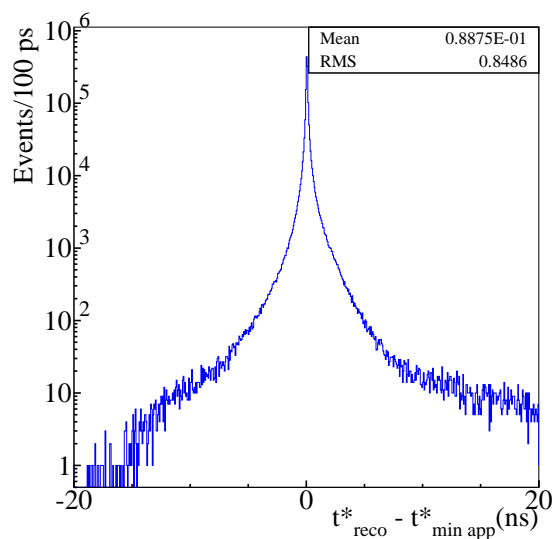
Figure 5.47: Proper time resolution curve given by the minimum approach technique on data.
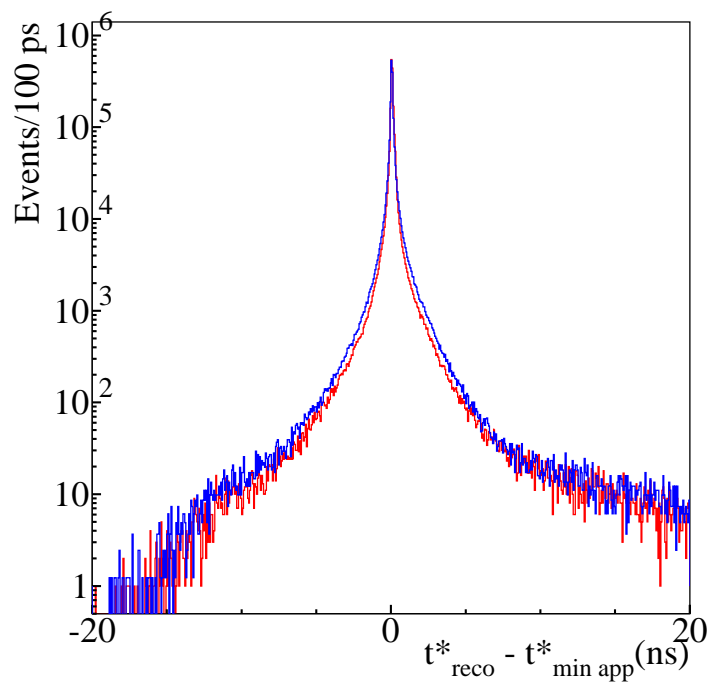
Figure 5.48: Comparison of the proper time resolution curves obtained by the minimum approach technique from data (blue) and from MonteCarlo (red) compared.
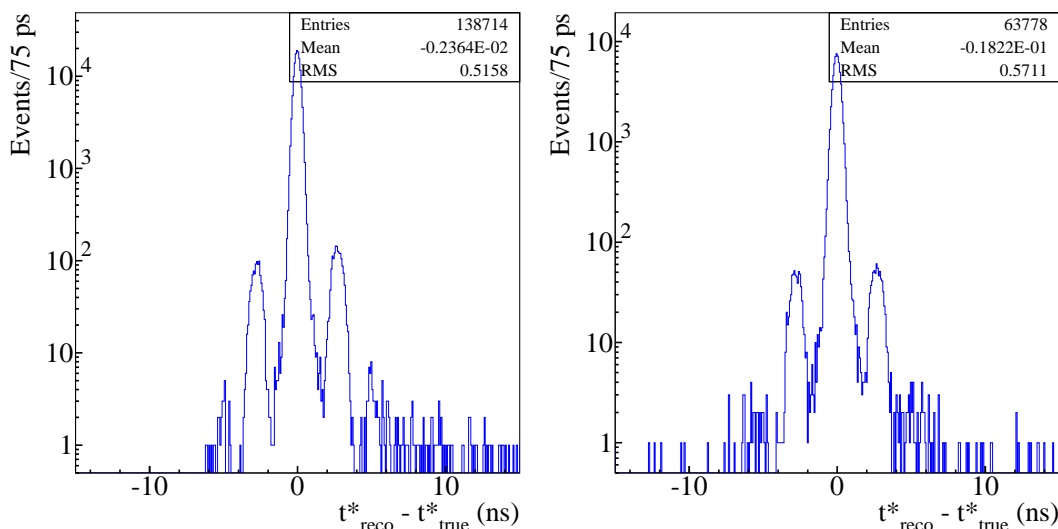
Figure 5.49: Left. Resolution curve for charged kaon proper time between 10 and 12 ns. Right. Resolution curve for charged kaon proper time between 20 and 22 ns.

time of flight given by the two photons:

$$\Delta t = \left(t_{cl_1} - \frac{\Delta x_1}{c}\right) - \left(t_{cl_2} - \frac{\Delta x_2}{c}\right) \tag{5.68}$$

where t_{cl_i} is the time of the cluster and Δx_i is the distance between the neutral cluster and the kaon decay vertex. These resolution functions can be evaluated on MonteCarlo data-like and on data. As it can be seen in figure 5.50, the $\gamma\gamma$ resolution curves are not able to take into account the resolution effects due to a wrong ϕ decay time, which is common to all time measurements in the event and cancels out exactly in the difference.

In order to evaluate also this effect we estimate the difference, $t_{\pi^0}^* - t_{cv}^*$, between the proper time given by the charged vertex technique and the proper time given by the $\pi^0 \to \gamma\gamma$ vertex technique, figure 5.51, on data and on MonteCarlo data-like.

The proper time given by the last technique is obtained from EMC information, which are dependent on the ϕ meson decay time, while the proper time given by the charged vertex technique is obtained from DC information which is not dependent on ϕ decay time.

On data we correct the true resolution functions core by the ratio of the $\gamma\gamma$ resolution curves evaluated on data over the $\gamma\gamma$ resolution curves evaluated on MonteCarlo data-like; we correct the peaks at ± 2.7 and ± 5.4 ns by the ratio of $t_{\pi^0}^* - t_{cv}^*$ resolution curves evaluated on data over $t_{\pi^0}^* - t_{cv}^*$ resolution curves evaluate on MC data-like:

$$Res_{\text{data}} = Res_{\text{true}} \times \frac{Res_{\gamma\gamma}(data)}{Res\gamma\gamma(MC)} + Res_{true}^{t\phi} \times \frac{t_{\pi^0}^* - t_{cv}^*(data)}{t_{\pi^0}^* - t_{cv}^*(MC)}, \tag{5.69}$$

where Res_{true} are the resolution functions given by the MonteCarlo true, defined as
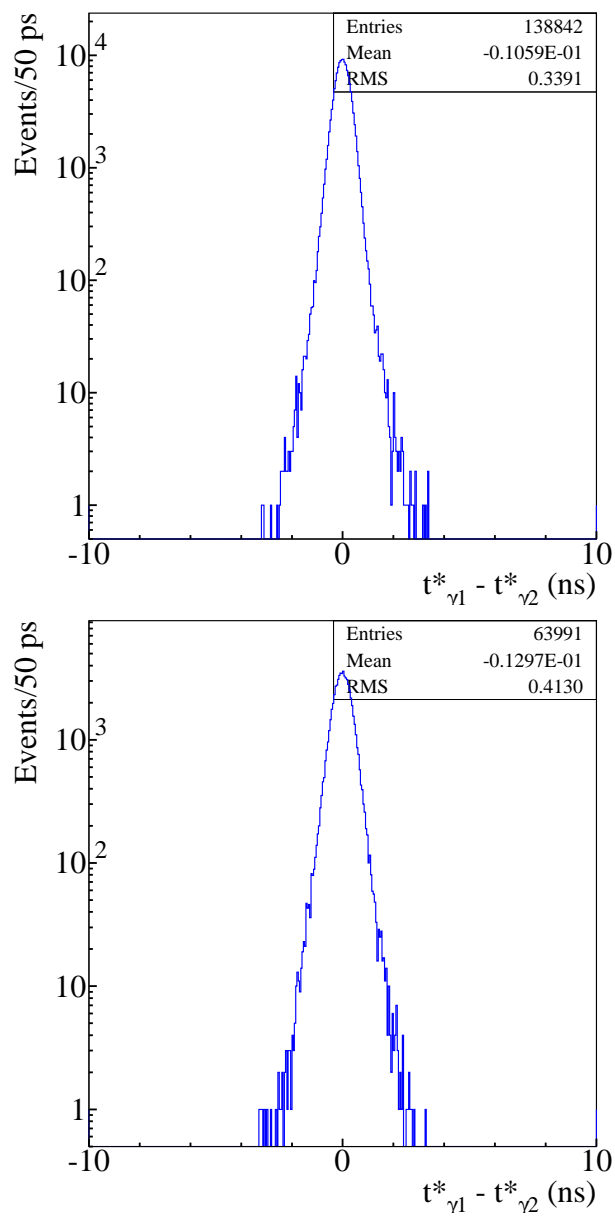
Figure 5.50: Left. $\gamma\gamma$ resolution curve for charged kaon proper time between 10 and 12 ns. Right. $\gamma\gamma$ resolution curve for charged kaon proper time between 20 and 22 ns.
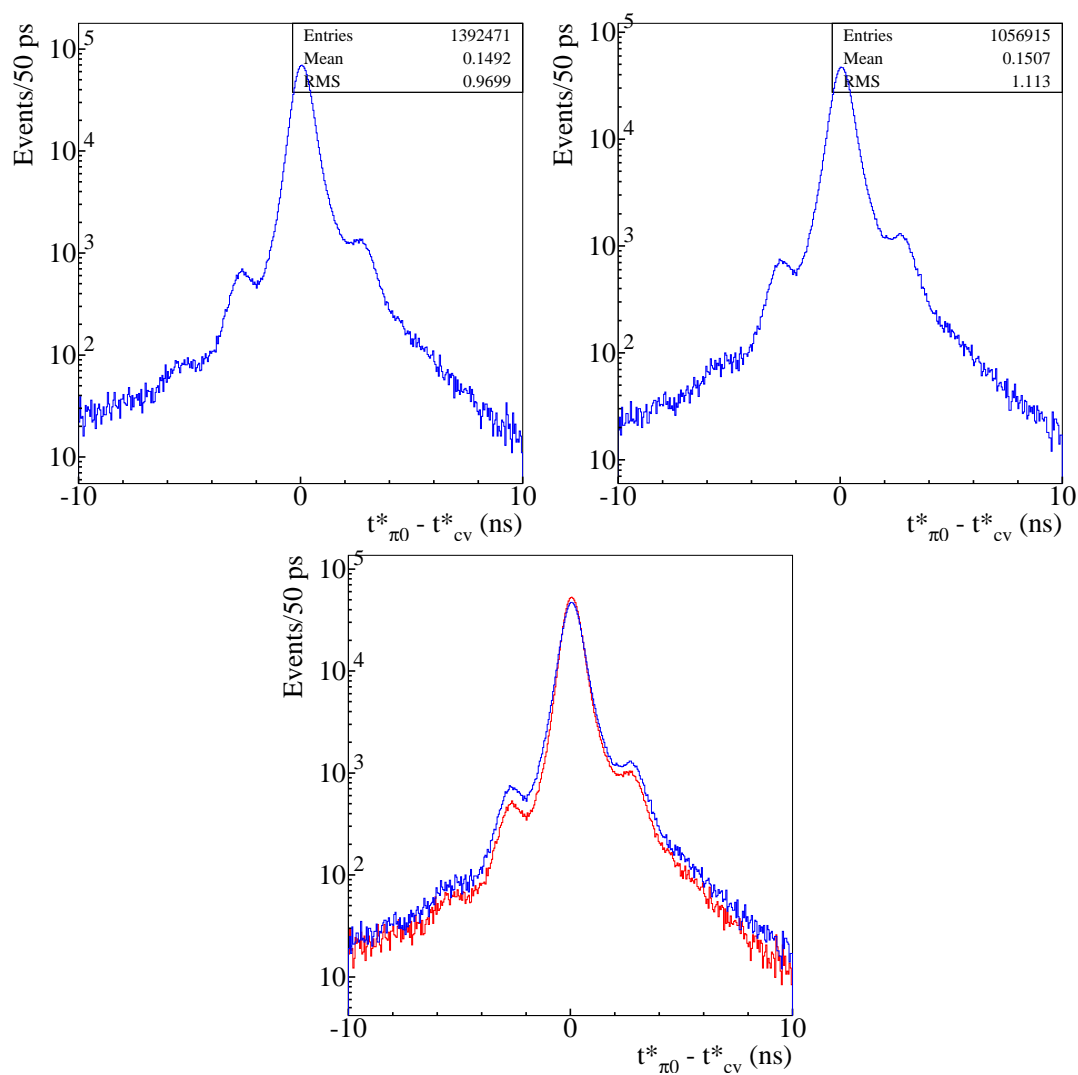
Figure 5.51: $t^*_{\pi^0} - t^*_{cv}$ resolution curves, evaluated on MonteCarlo data-like, above on the left. $t^*_{\pi^0} - t^*_{cv}$, resolution curves evaluated on data, above on the right. Comparison between data (blue) and MonteCarlo (red).

the difference between the charged kaon proper time evaluated on MonteCarlo data-like and the charged kaon proper time given by the MonteCarlo true; $Res_{\gamma\gamma}(data)$ and $Res_{\gamma\gamma}(MC)$ are the $\gamma\gamma$ resolution curves evaluated on data and on MonteCarlo data-like respectively; $t_{\pi^0}^* - t_{cv}^*(data)$ is the difference between the proper time given by the $\pi^0 \to \gamma\gamma$ vertex technique and the proper time given by the charged vertex technique evaluated on data and $t_{\pi^0}^* - t_{cv}^*(MC)$ is the same difference evaluated on MonteCarlo data-like.

5.8 The fit of the proper time distribution

The last step is to obtain the charged kaon lifetime fitting the proper time distribution. For both the methods we use a function given by the convolution of the exponential decay function and the resolution function, estimated bin by bin. We notice anyhow that the measured distributions, corrected bin by bin for the efficiency exhibits a nicely exponential behavior, even with no smearing correction for both the methods (see figures 5.52 and 5.53). To fit to the proper time distribution, obtained on MonteCarlo data-like or on data, we use an histogram, the *expected* histo. This is built in the following way. The number of entries in each bin of the *expected* histo is given by the integral of the exponential decay function, which depends on one parameter only, the lifetime, and corrected for the efficiency curve and for all the corrections to the efficiency curve, self trigger tag efficiency or MonteCarlo true vs MonteCarlo reco correction. Then a smearing matrix accounts for the effect of the resolution. For each bin, j, we obtain a χ^2-like variable which is so defined:

$$\chi_j^2 = \frac{(N_j^{observed} - N_j^{expected})^2}{(\sigma_j^{fit})^2} \qquad (5.70)$$

where $N_j^{observed}$ is the number of entries in the j-th bin of the proper time histogram, $N_j^{expected}$ is the number of entries in the j-th bin of *expected* histo and σ_j^{fit} is the statistic fluctuation in the j-th bin of the *expected* histo. The χ^2 variable to be minimized is:

$$\chi^2 = \sum_{j=1}^{Nbins} \chi_j^2 \ . \qquad (5.71)$$

We can build our *expected* histo in the more convenient range, given by the one in which we have a good agreement between the true and the reco efficiencies. To take into account the resolution effects, we have allowed the migration from/to the bins used in the fit for a slightly larger range.
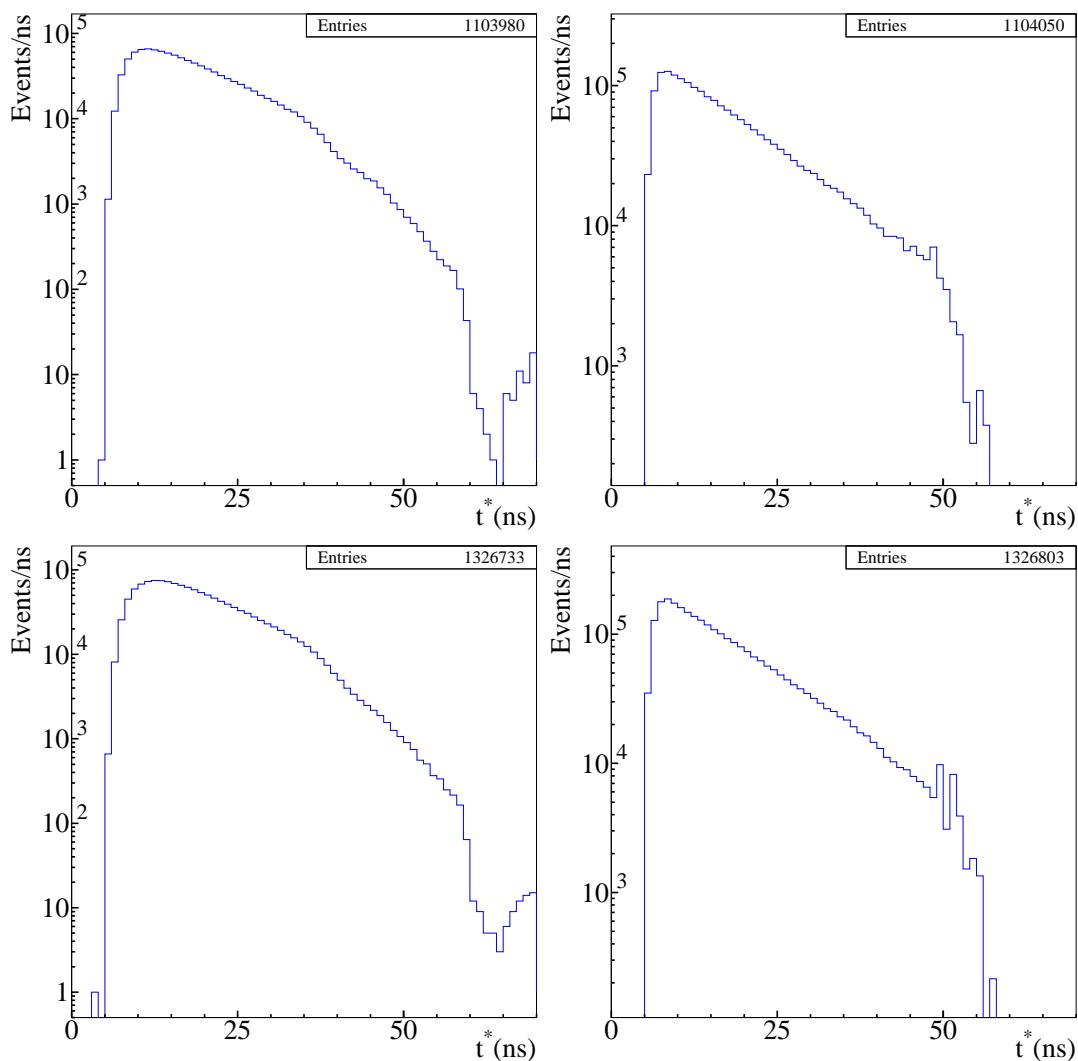
Figure 5.52: First method:above on the left the proper time distribution in logarithmic scale, evaluated on a MonteCarlo data-like; above on the right the same distribution divided, bin by bin, by its efficiency evaluated on a MonteCarlo data-like sample; below on the left the proper time distribution in logarithmic scale, evaluated on a data sample; below on the right the same distribution divided, bin by bin, by its efficiency curve evaluated on a data sample.
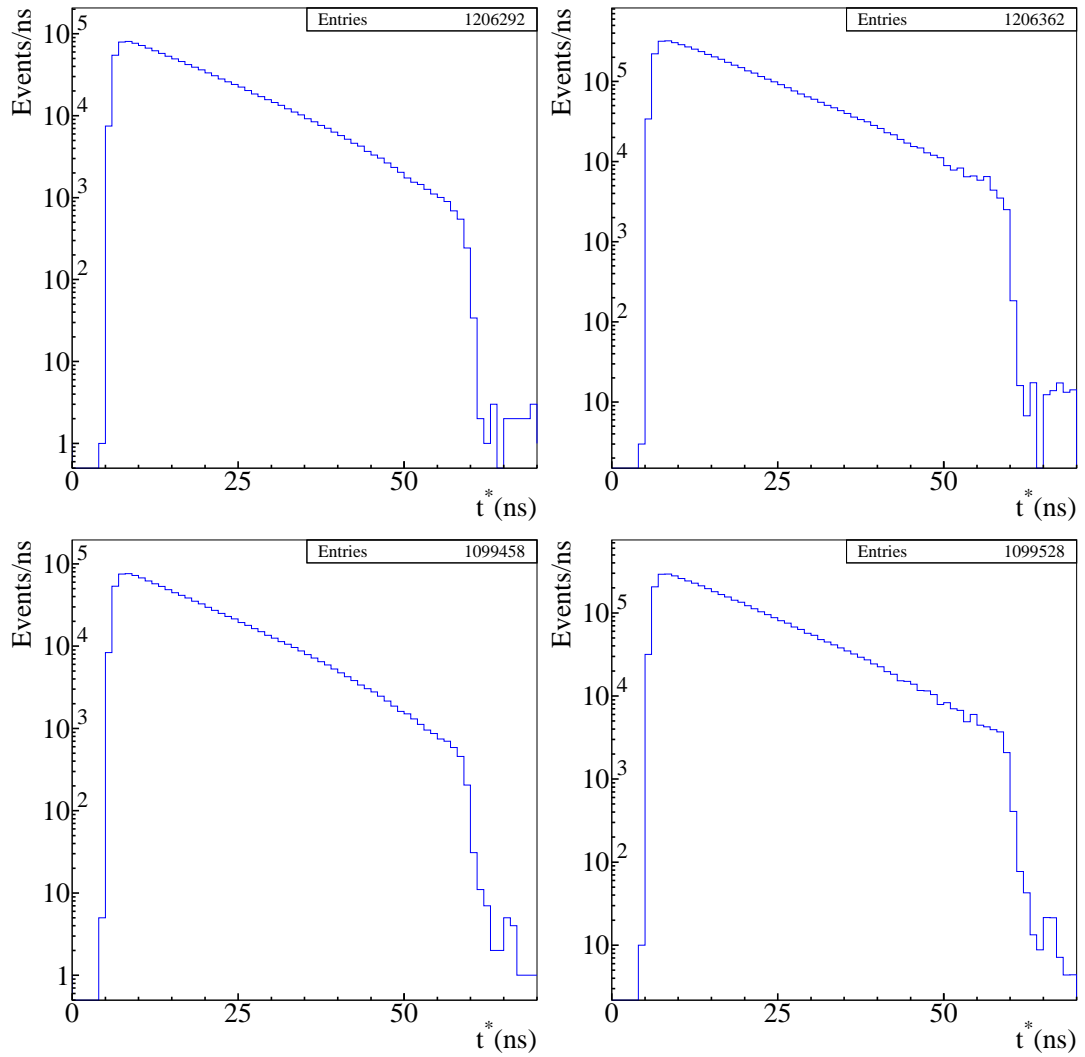
Figure 5.53: Second method:above on the left the proper time distribution in logarithmic scale, evaluated on a MonteCarlo data-like; above on the right the same distribution divided, bin by bin, by its efficiency evaluated on a MonteCarlo data-like sample; below on the left the proper time distribution in logarithmic scale, evaluated on a data sample; below on the right the same distribution divided, bin by bin, by its efficiency curve evaluated on a data sample.

The range have to be divided in slices of the order of few nanoseconds in which we evaluate the resolution functions. The choice of the bin size is done in order to reduce the statistical fluctuation of the resolution measurement.

Using these resolution functions we can build the $n \times n$ smearing matrix, S_{nn}, with n equal to the number of bins in which we have divided the proper time distribution. Each element of S_{nn}, s_{ji}, gives the fraction of events generated in the i-th bin but reconstructed in the j-th bin. Therefore the content of the j-th bin of the *expected* histo, ($N_j^{expected}$), is:

$$N_j^{expected} = \sum_{i=1}^{Nbins} s_{ji} \times \epsilon_i \times \epsilon_i^{corr} \times N_i^{theo}, \tag{5.72}$$

where ϵ_i is the measured reconstruction efficiency and ϵ_i^{corr} the tiny correction of $O(10^{-3})$ to be applied to the efficiency accounting for the ratio between the MonteCarlo data-like and MonteCarlo true efficiencies. The statistical fluctuations of the *expected* histo are given by the sum of the statistical fluctuation of the efficiency, the statistical fluctuation of its correction and the poissonian fluctuation of the *expected* histo:

$$\sigma_j^{fit} = \sqrt{\sum_{i=1}^{Nbins} \left(s_{ji} \times \sigma_{\epsilon_i} \times \epsilon_i^{corr} \times N_i^{theo} \oplus s_{ji} \times \epsilon_i \times \sigma_{\epsilon_i^{corr}} \times N_i^{theo} \right) \oplus \sqrt{N_j^{expected}}}. \tag{5.73}$$

Now we are ready to fit the proper time distribution, for both the methods. We use a bin size of 1 ns in order to reduce the statistical fluctuations and the relative importance of the smearing corrections. We perform the fit on a MonteCarlo data-like sample to check the reliability of the procedure.

5.8.1   Fit of the proper time distribution obtained from the kaon decay length

We build the *expected* histo in the region between 12 and 40 ns.

The fit range has been divided in resolution bins of the order of 1 ns for a total of 28 different resolution functions.

On MonteCarlo data-like we made the fit in the region between 15 and 35 ns and we obtained:

$$\tau^+ = (12.39 \pm 0.04) \text{ ns} \qquad \chi^2/\text{ndf} = 0.46 \qquad \text{P}_{\text{chi2}} = 97.5\% \ . \tag{5.74}$$

For the K^-, in the region between 15 and 35 ns, we obtained:

$$\tau^- = (12.36 \pm 0.04) \text{ ns} \qquad \chi^2/\text{ndf} = 0.85 \qquad P_{\text{chi}^2} = 63.5\% . \qquad (5.75)$$
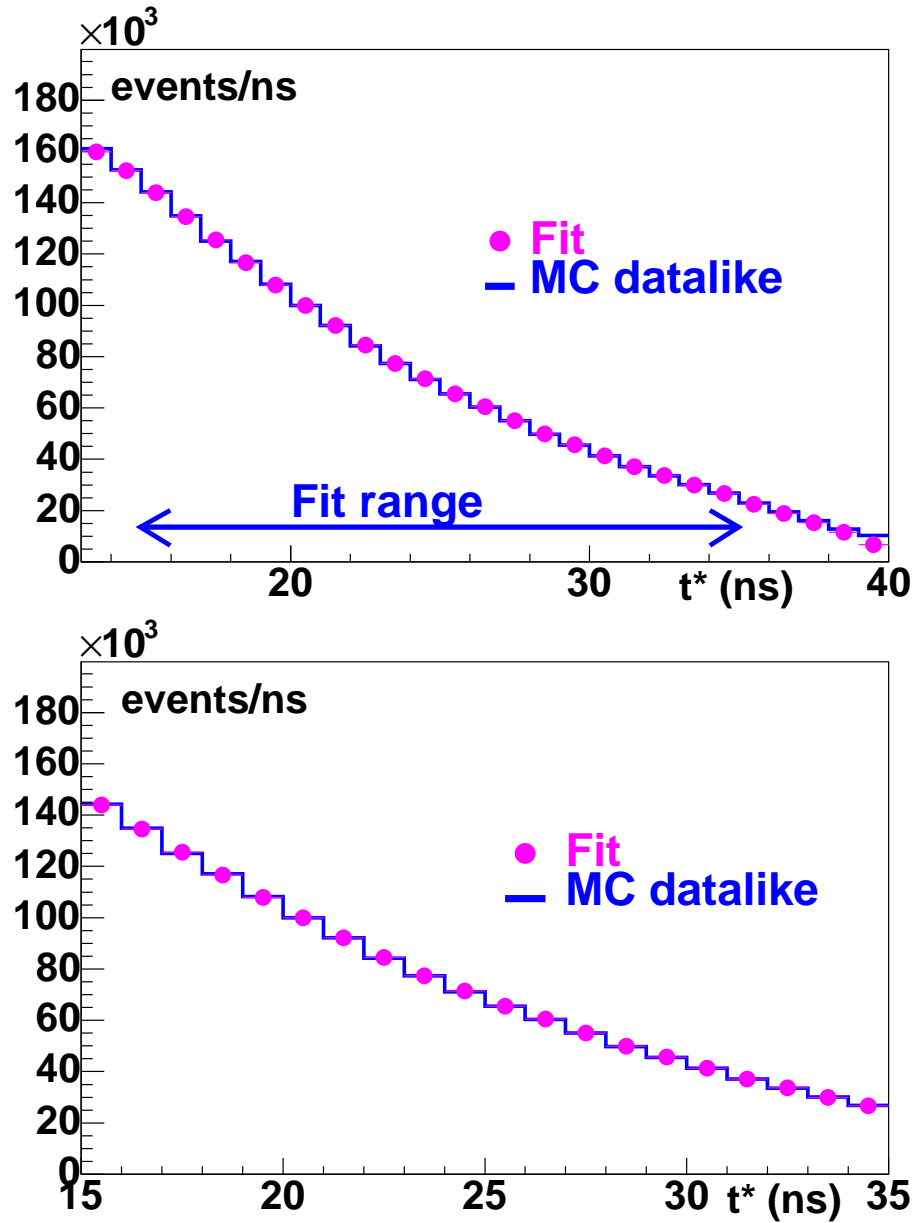
Figure 5.54: Fit to the K^+ proper time distribution: in blue the MonteCarlo data-like distribution, in pink the *expected* histo distribution.

These values have to be compared with the one used by the simulation $\tau^\pm = 12.36$ ns. As shown in the previous figures 5.54 and 5.55 the agreement between data-like
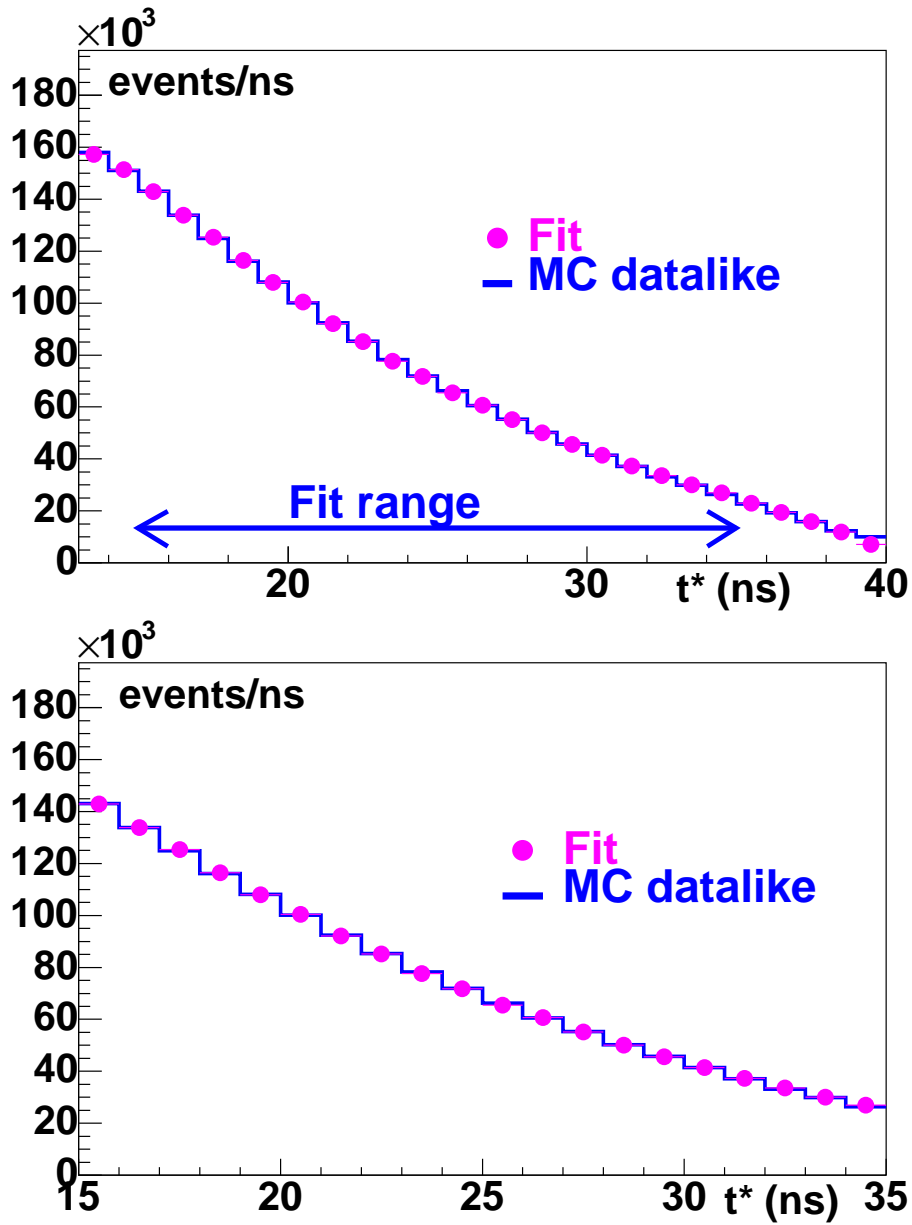
Figure 5.55: Fit to the K^- proper time distribution: in blue the MonteCarlo data-like distribution, in pink the *expected* histo distribution.

distribution and *expected* histo distribution is very good for both the charges and the values obtained are in agreement with the MonteCarlo simulation input.

It is interesting to look at the plot of the residuals and of the normalized residuals, fig 5.56. The first ones are defined as the bin by bin differences between the entries of the proper time histogram and the entries of *expected* histo, the second ones are the residuals divided by σ^{fit}. As shown in the previous figures 5.56 and 5.57, fitting the
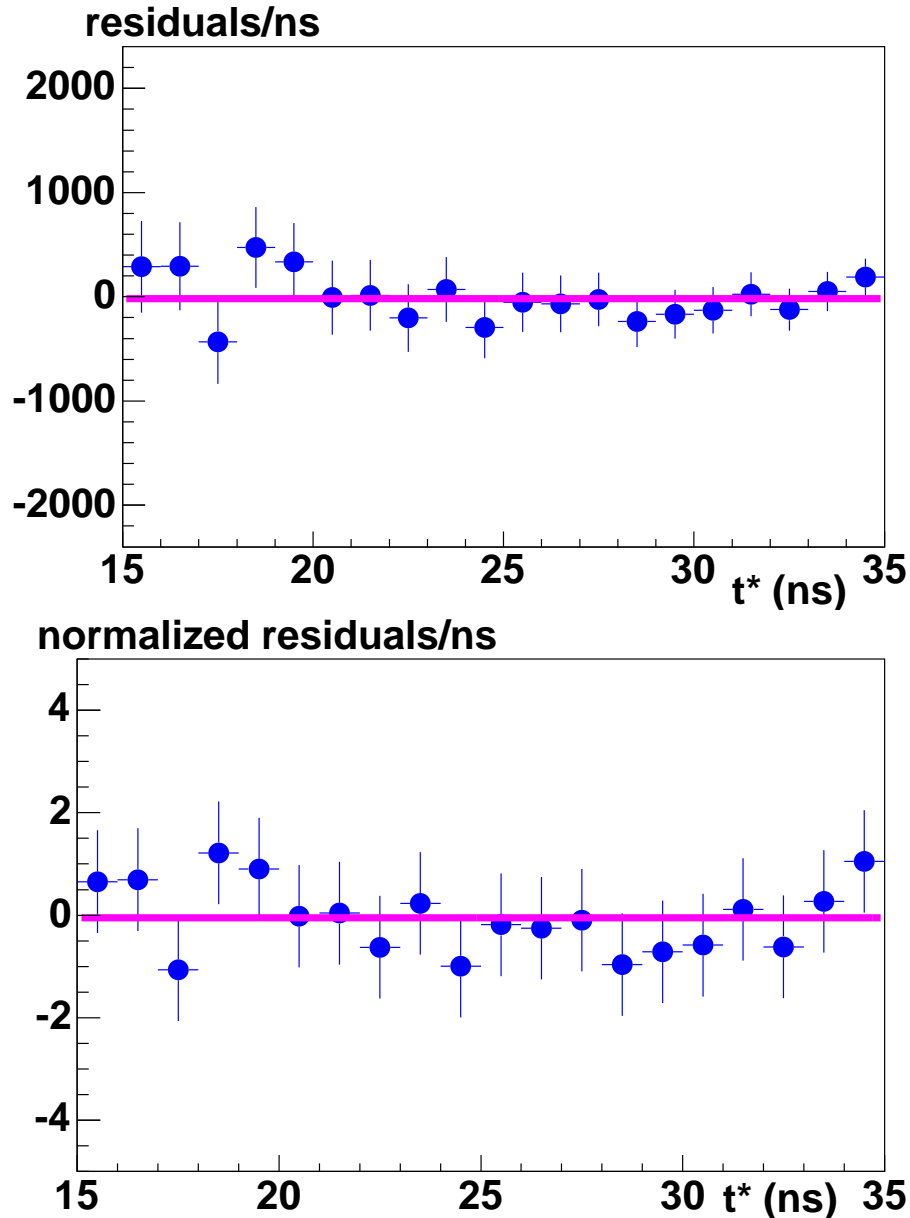
Figure 5.56: K^+ residuals and the normalized residuals, in the region between 15 and 35 ns, fitted with a constant, are shown.
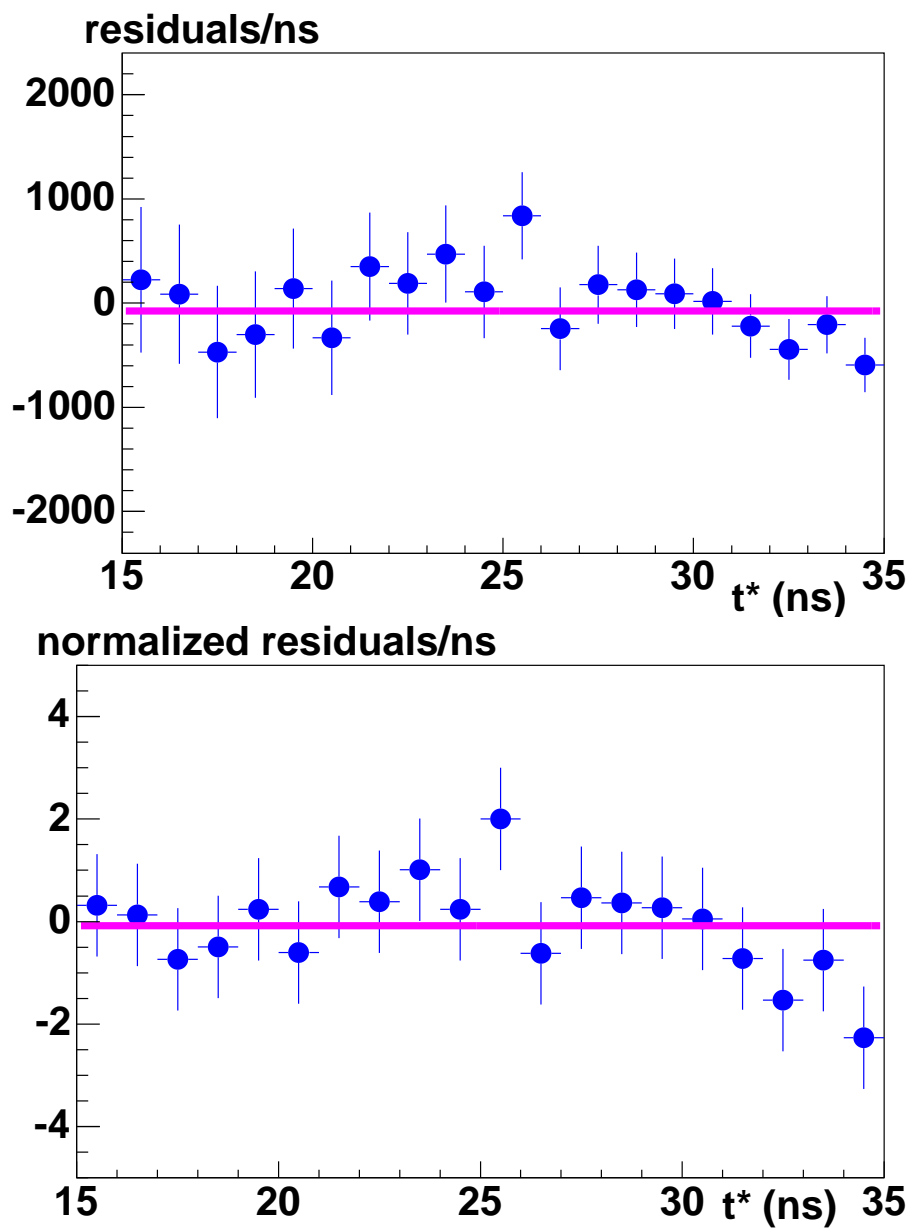
Figure 5.57: K^- residuals and the normalized residuals, in the region between 15 and 35 ns, fitted with a constant are shown.

residuals and the normalized residuals plots with a constant function we obtain a value compatible with zero:

$$const_{\text{res}}^{+} = -19. \pm 60. \qquad P_{\chi^2} = 97\% \qquad (5.76)$$

$$const_{\text{norm res}}^{+} = -0.05 \pm 0.22 \qquad P_{\chi^2} = 97\% \qquad (5.77)$$

$$const_{\text{res}}^{-} = -75. \pm 88. \qquad P_{\chi^2} = 68\% \qquad (5.78)$$

$$const_{\text{norm res}}^{-} = -0.08 \pm 0.22 \qquad P_{\chi^2} = 64\%. \qquad (5.79)$$

$$(5.80)$$

We also use a toy MonteCarlo to generate data with different lifetimes for both the charges. In particular we generate about 60 pb$^-$1 of MonteCarlo data-like with lifetimes equal to 11, 12, 13 and 14 ns.
Fitting the histograms obtained with these MonteCarlo data-like samples, the results are:

$$\tau_{11}^{+} = (10.98 \pm 0.08) \text{ ns} \qquad (5.81)$$

$$\tau_{11}^{-} = (11.02 \pm 0.08) \text{ ns} \qquad (5.82)$$

$$\tau_{12}^{+} = (11.98 \pm 0.09) \text{ ns} \qquad (5.83)$$

$$\tau_{12}^{-} = (12.02 \pm 0.09) \text{ ns} \qquad (5.84)$$

$$\tau_{13}^{+} = (12.97 \pm 0.09) \text{ ns} \qquad (5.85)$$

$$\tau_{13}^{-} = (13.02 \pm 0.09) \text{ ns} \qquad (5.86)$$

$$\tau_{14}^{+} = (13.97 \pm 0.10) \text{ ns} \qquad (5.87)$$

$$\tau_{14}^{-} = (14.01 \pm 0.10) \text{ ns} \qquad (5.88)$$

$$(5.89)$$

These are indicator of the goodness of our method and make us confident about its application for the fit of the proper time distribution obtained on data. On data, concerning the K^+ lifetime, we made the fit in the region between 15 and 35 ns and we obtained:

$$\tau^{+} = (12.338 \pm 0.042) \text{ ns} \qquad \chi^2/\text{ndf} = 1.01 \qquad P_{\chi^2} = 44.7\% \ . \qquad (5.90)$$

While for the K^- we fit in the range between 15 and 35 ns and we obtained:

$$\tau^{-} = (12.395 \pm 0.045) \text{ ns} \qquad \chi^2/\text{ndf} = 1.42 \qquad P_{\chi^2} = 10.8\% \ . \qquad (5.91)$$

As shown in the previous figures 5.58 and 5.59 the agreement between data distribution and *expected* histo distribution is very good for both the charges.
For both the charges the distribution of residuals and of the normalized residuals is very good and compatible with a constant function equal to zero. As shown in the
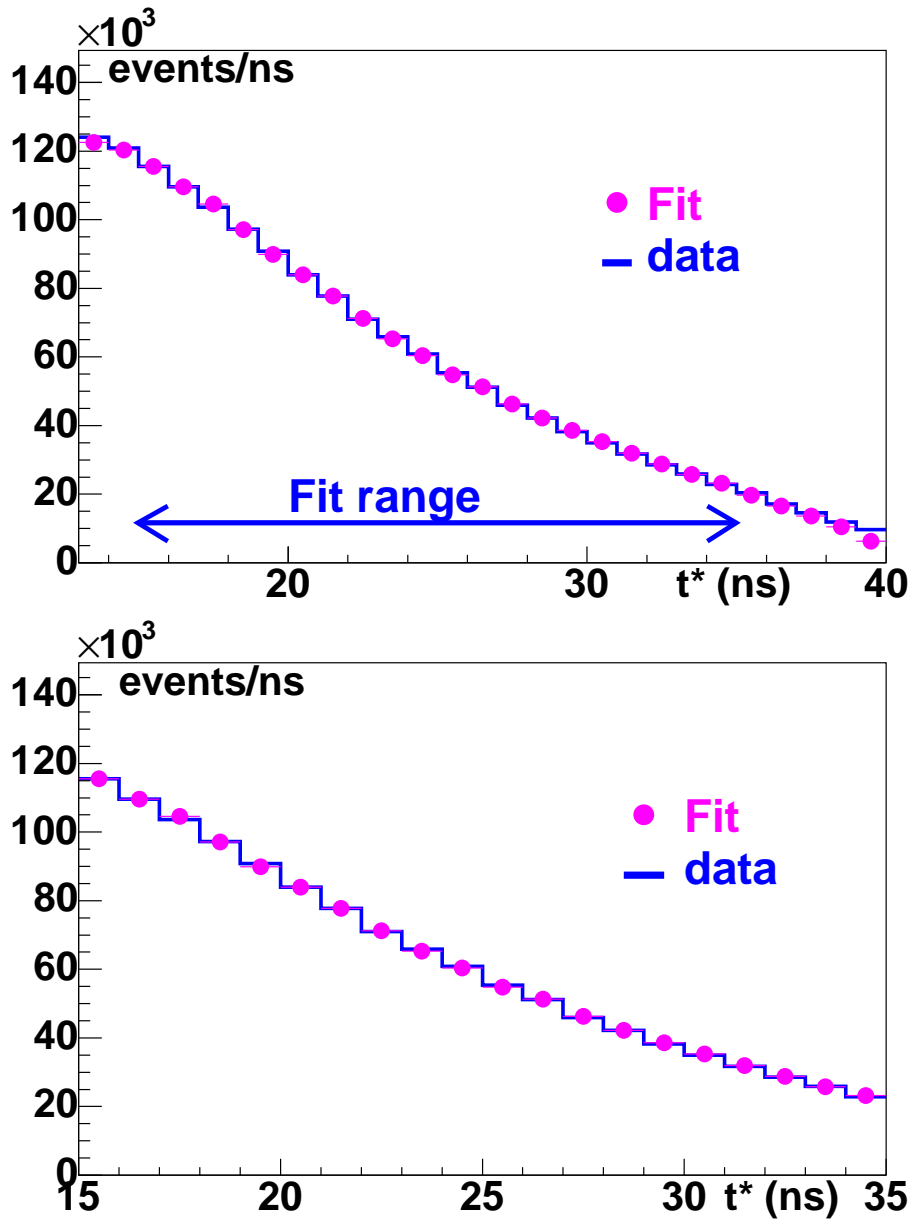
Figure 5.58: Fit to the K^+ proper time distribution: in blue the data distribution, in pink the *expected* histo distribution.
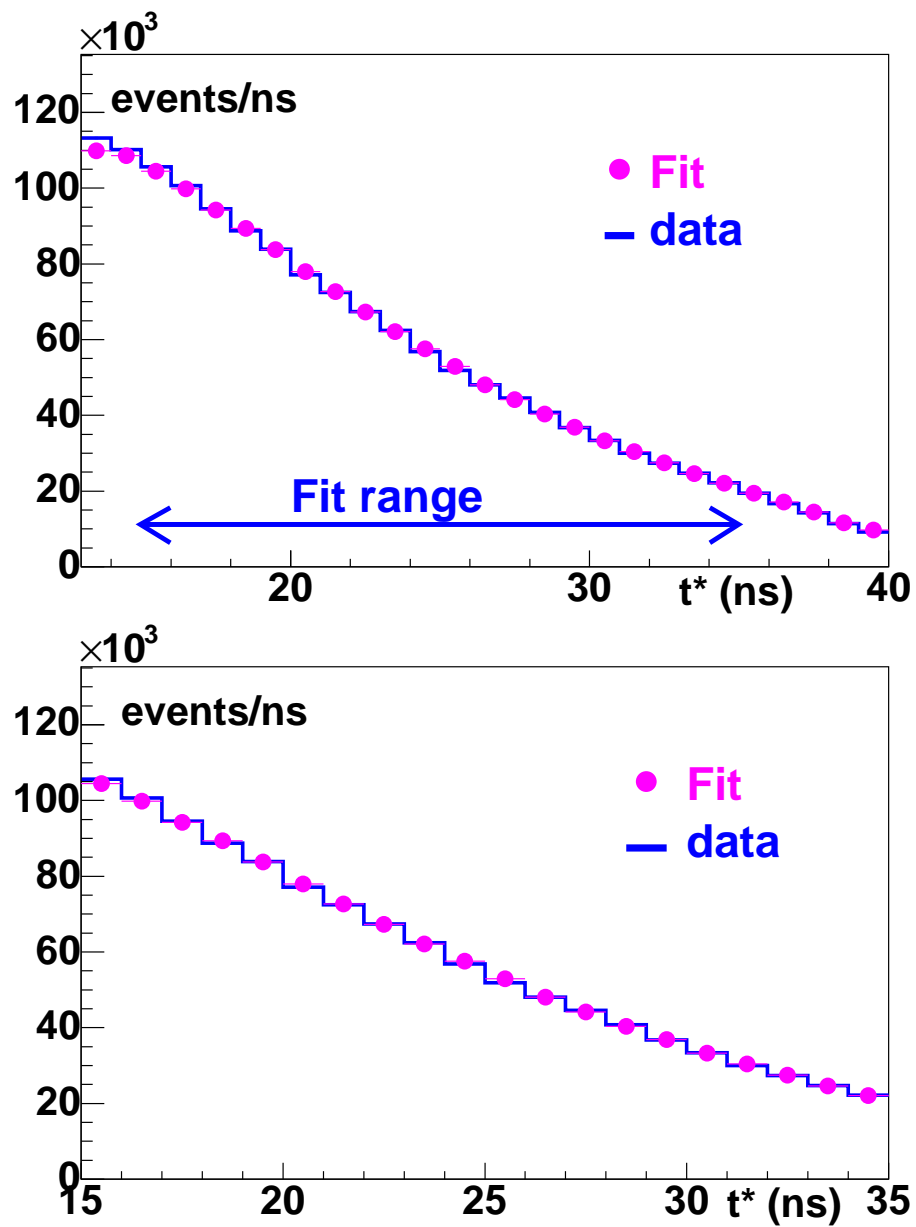
Figure 5.59: Fit to the K^- proper time distribution: in blue the data distribution, in pink the *expected* histo distribution.
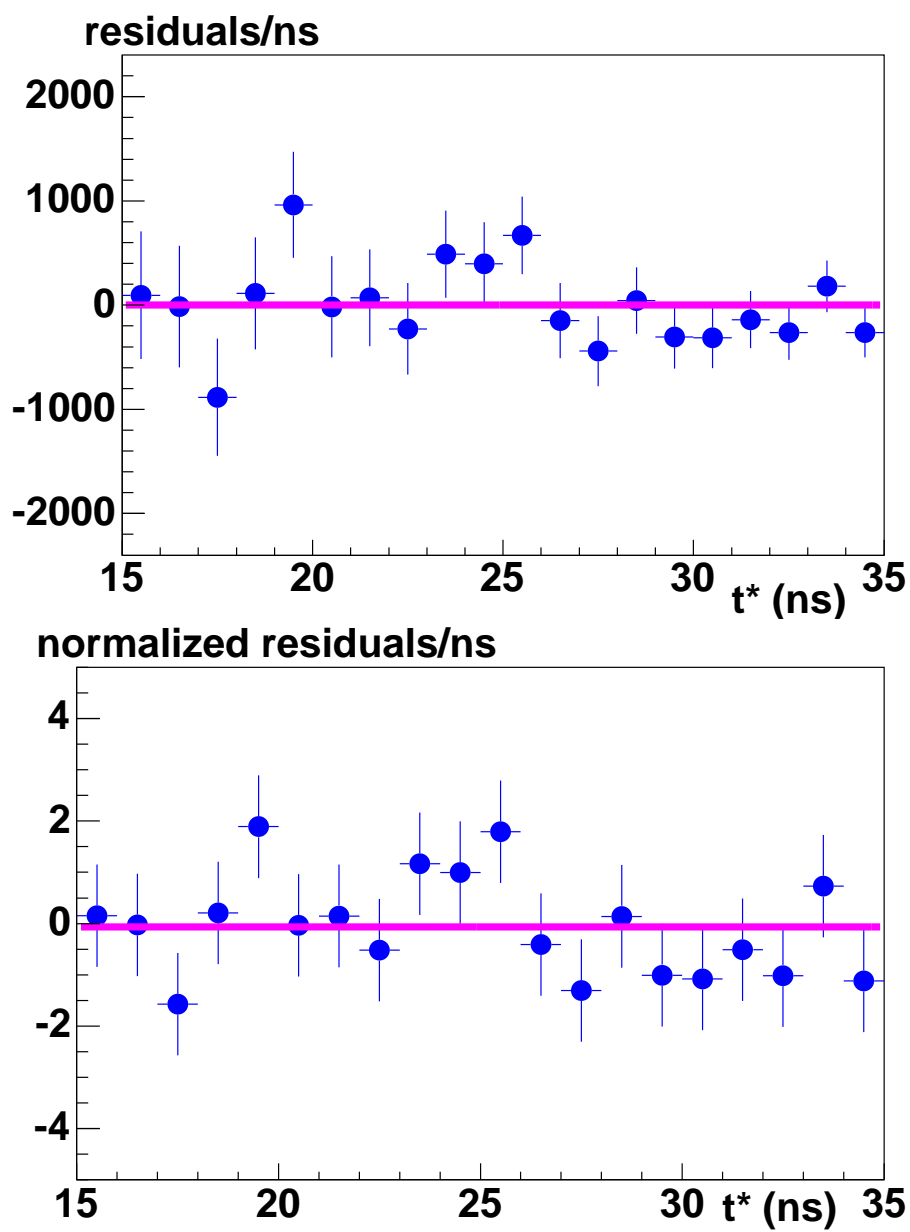
Figure 5.60: K^+ residuals and the normalized residuals, in the region between 15 and 35 ns, fitted with a constant.
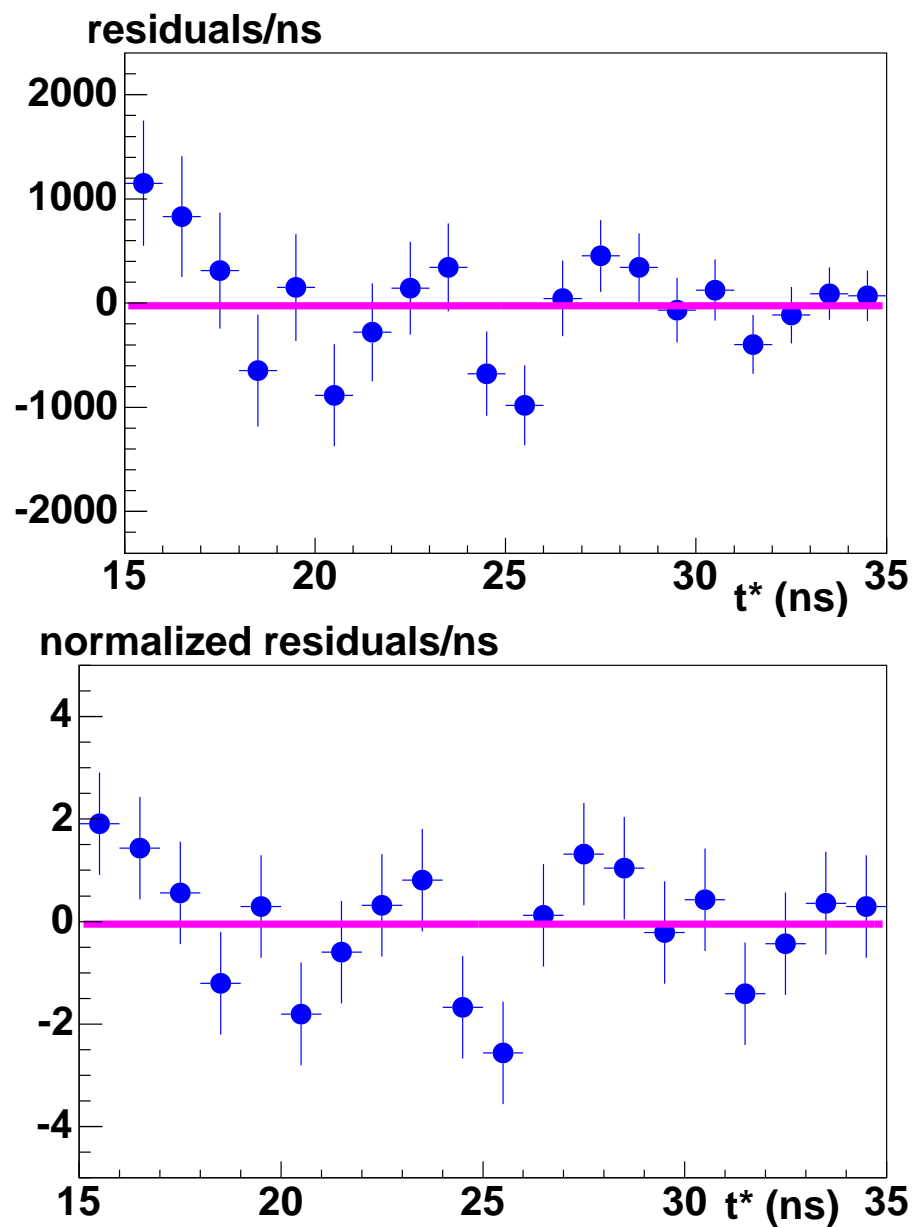
Figure 5.61: K^- residuals and the normalized residuals, in the region between 15 and 35 ns, fitted with a constant.

previous figures, fitting the residuals and the normalized residuals with a constant the values obtained are in agreement with zero:

$$const_{\text{res}}^{+} = 0.0 \pm 1.4 \qquad\qquad P_{\chi^2} = 45.\% \qquad\qquad (5.92)$$

$$const_{\text{norm res}}^{+} = -0.06 \pm 0.22 \qquad\qquad P_{\chi^2} = 45.\% \qquad\qquad (5.93)$$

$$const_{\text{res}}^{-} = -25. \pm 80. \qquad\qquad P_{\chi^2} = 11.\% \qquad\qquad (5.94)$$

$$const_{\text{norm res}}^{-} = -0.05 \pm 0.22 \qquad\qquad P_{\chi^2} = 11.\%. \qquad\qquad (5.95)$$

$$(5.96)$$

The measurements obtained for the different charges are in agreement with each other. Their weighted mean is:

$$\tau = (12.364 \pm 0.031) \text{ ns}. \qquad\qquad (5.97)$$

5.8.2 Fit to the proper time distribution obtained from the kaon decay time

We build the *expected* histo in the region between 10 and 50 ns.

The fit range has been divided in bins of the order of few nanoseconds for a total of 17 different resolution functions. In particular the interval between 10 and 40 ns has been divided in bins of 2 ns. The last two resolution functions have been obtained in the intervals between 40 and 45 ns and between 45 and 50 ns.

On MonteCarlo data-like we made the fit in the region between 13 and 40 ns and we obtained as best value:

$$\tau^{+} = (12.39 \pm 0.04) \text{ ns} \qquad \chi^2/\text{ndf} = 0.43 \qquad P_{\chi^2} = 99.4\%. \qquad (5.98)$$

For the K^-, in the region between 12 and 40 ns, we obtain as best value:

$$\tau^{-} = (12.30 \pm 0.04) \text{ ns} \qquad \chi^2/\text{ndf} = 0.81 \qquad P_{\chi^2} = 73.\%. \qquad (5.99)$$

As shown in the previous figures 5.62 and 5.63 the agreement between data-like distribution and *expected* histo distribution is very good for both the charges and the values obtained are in agreement with the MonteCarlo simulation input, $\tau^{\pm} = 12.36$ ns.
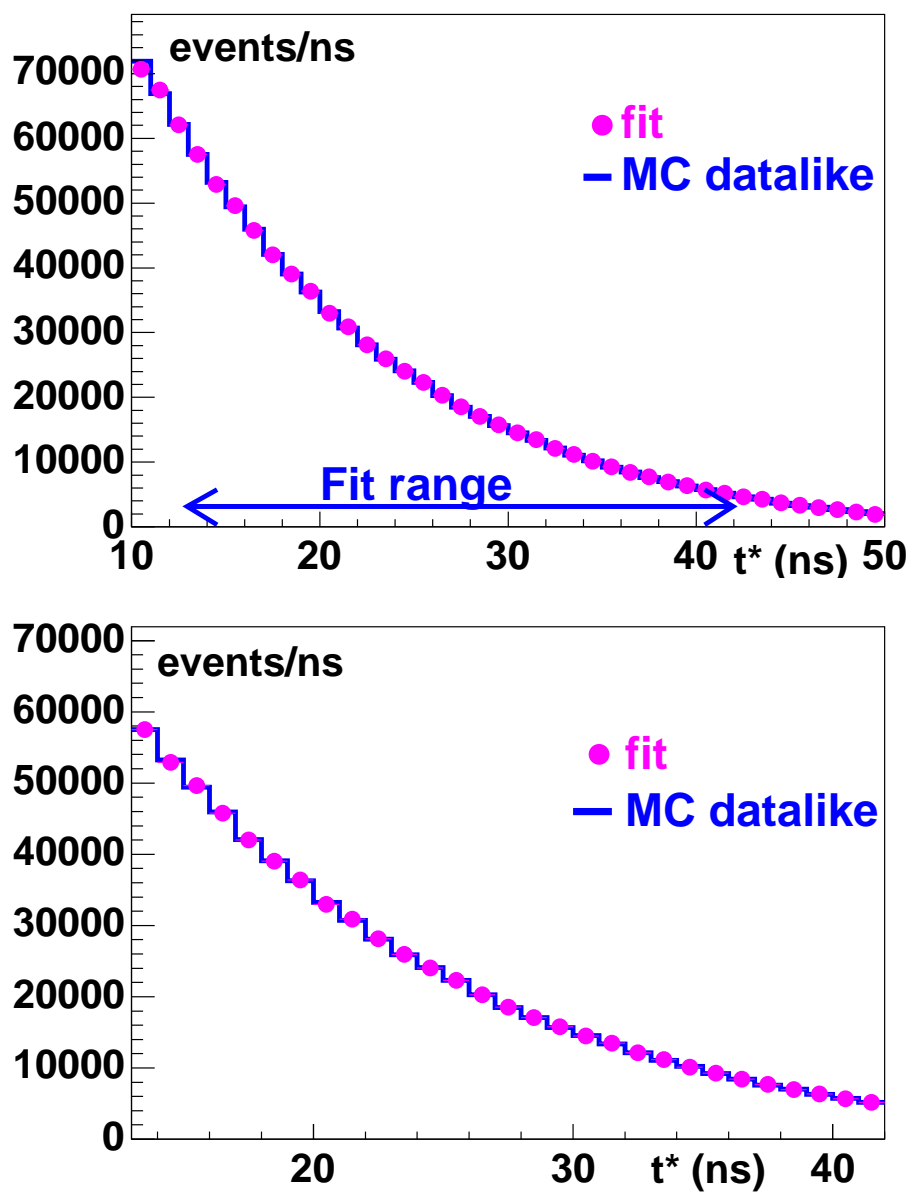
Figure 5.62: In the picture the fit to the K^+ proper time distribution is shown: in blue the MonteCarlo data-like distribution, in pink the *expected* histo distribution.
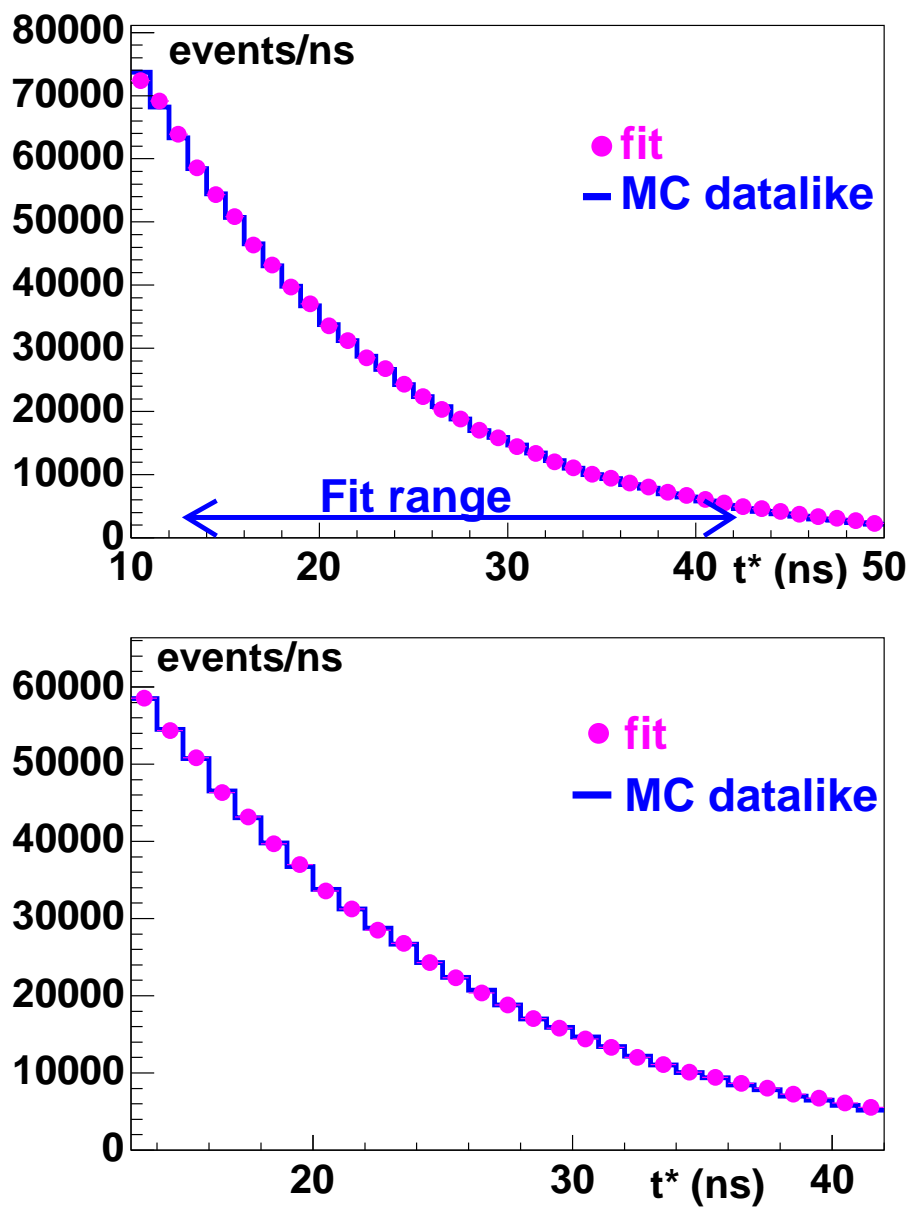
Figure 5.63: In the picture the fit to the K^- proper time distribution: is shown in blue the MonteCarlo data-like distribution, in pink the *expected* histo distribution.

Fitting with a constant the residuals and the normalized residuals, figures 5.64 and 5.65, we obtain values compatible with zero:

$$const_{\text{res}}^{+} = -15. \pm 28. \qquad P_{\chi^2} = 99.\% \qquad (5.100)$$

$$const_{\text{norm res}}^{+} = -0.06 \pm 0.19 \qquad P_{\chi^2} = 99.\% \qquad (5.101)$$

$$const_{\text{res}}^{-} = -37. \pm 39. \qquad P_{\chi^2} = 77.\% \qquad (5.102)$$

$$const_{\text{norm res}}^{-} = -0.08 \pm 0.19 \qquad P_{\chi^2} = 73.\%. \qquad (5.103)$$

$$(5.104)$$

Also for this method, looking at the MonteCarlo data-like results, we are confident about its application for the fit of the proper time distribution obtained on data. On data, concerning the K^+ lifetime we made the fit in the region between 13 and 42 ns and we obtained:

$$\tau^{+} = (12.315 \pm 0.042) \text{ ns} \qquad \chi^2/\text{ndf} = .98 \qquad P_{\chi^2} = 49.\%. \qquad (5.105)$$

Also for the K^- we fit in the range between 12 and 42 ns and we obtain as best value:

$$\tau^{-} = (12.360 \pm 0.043) \text{ ns} \qquad \chi^2/\text{ndf} = 0.85 \qquad P_{\chi^2} = 69.\%. \qquad (5.106)$$

As shown in the figures 5.66 and 5.67 the agreement between data distribution and *expected* histo distribution is very good for both the charges.

For both the charges the distributions of residuals and of the normalized residuals is very good and compatible with a constant function equal to zero. Fitting the residual plots and the normalized residual plots with a constant the value obtained are in agreement with zero:

$$const_{\text{res}}^{+} = (0. \pm 7.) \times 10^{-7} \qquad P_{\chi^2} = 49.\% \qquad (5.107)$$

$$const_{\text{norm res}}^{+} = -0.07 \pm 0.18 \qquad P_{\chi^2} = 50.\% \qquad (5.108)$$

$$const_{\text{res}}^{-} = -19. \pm 32. \qquad P_{\chi^2} = 70.\% \qquad (5.109)$$

$$const_{\text{norm res}}^{-} = -0.06 \pm 0.12 \qquad P_{\chi^2} = 69.\%. \qquad (5.110)$$

$$(5.111)$$

The measures obtained for the different charges are in agreement with each other. Their weighted mean is:

$$\tau = (12.337 \pm 0.030) \text{ ns}. \qquad (5.112)$$
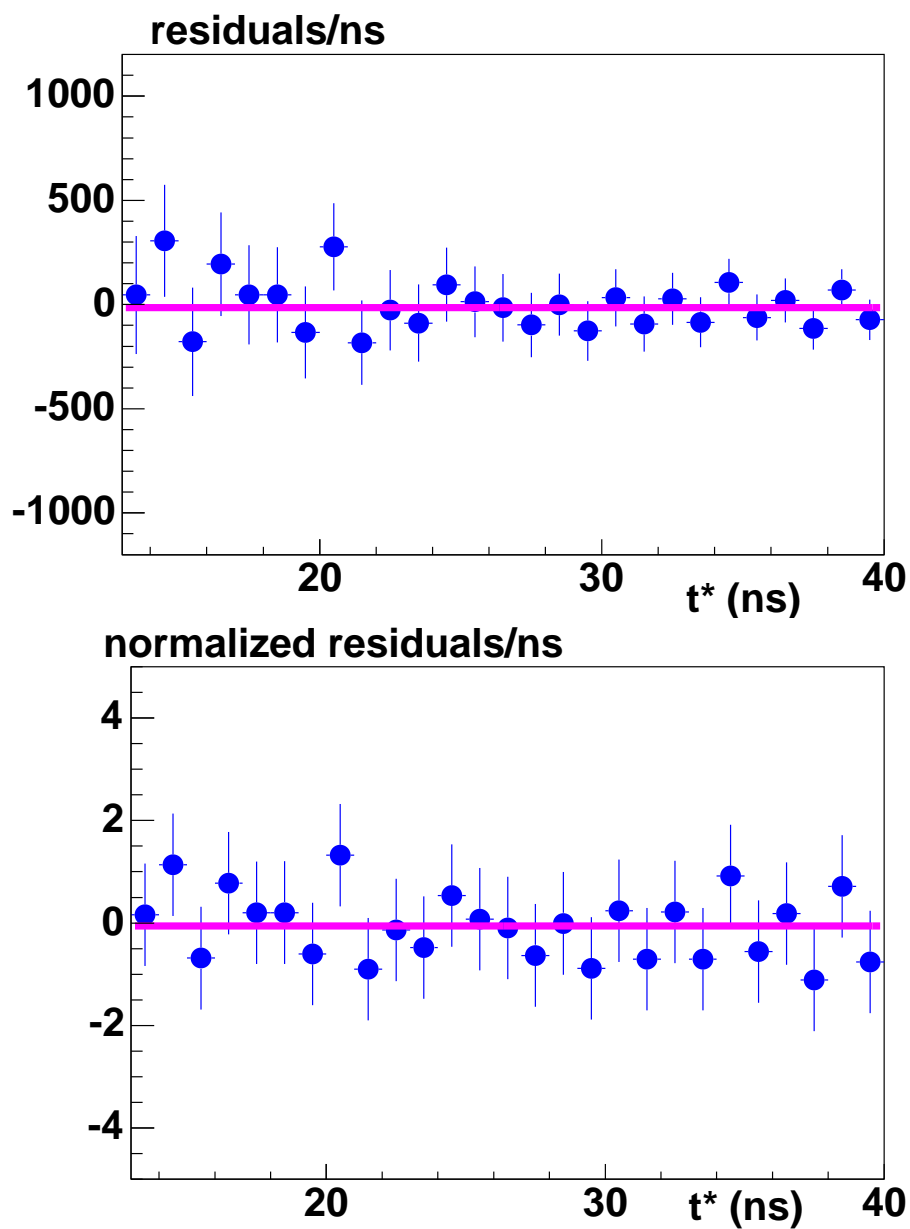
Figure 5.64: The K^+ residuals and the normalized residual plots, in the region between 13 and 40 ns, fitted with a constant are shown.
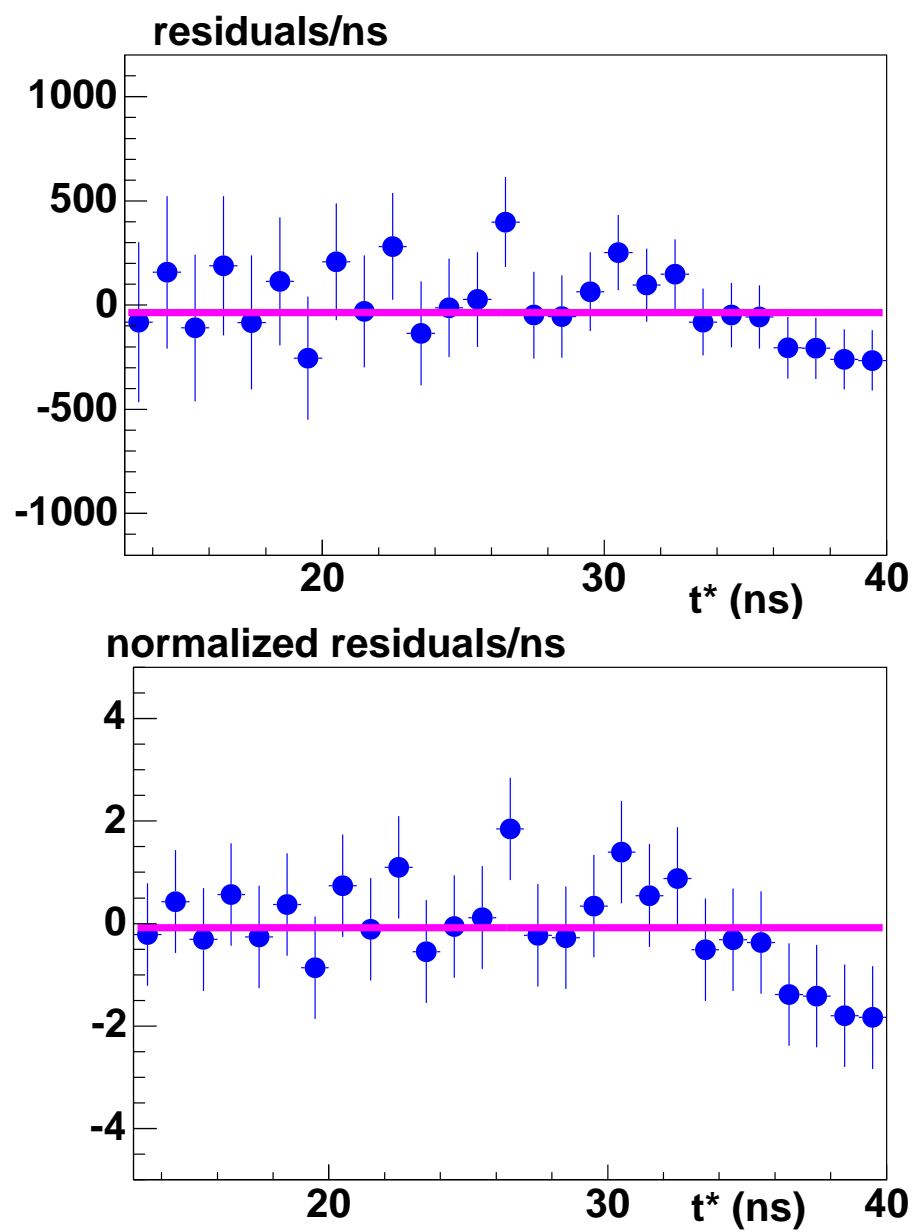
Figure 5.65: The K^- residuals and the normalized residuals, in the region between 13 and 40 ns, fitted with a constant are shown.
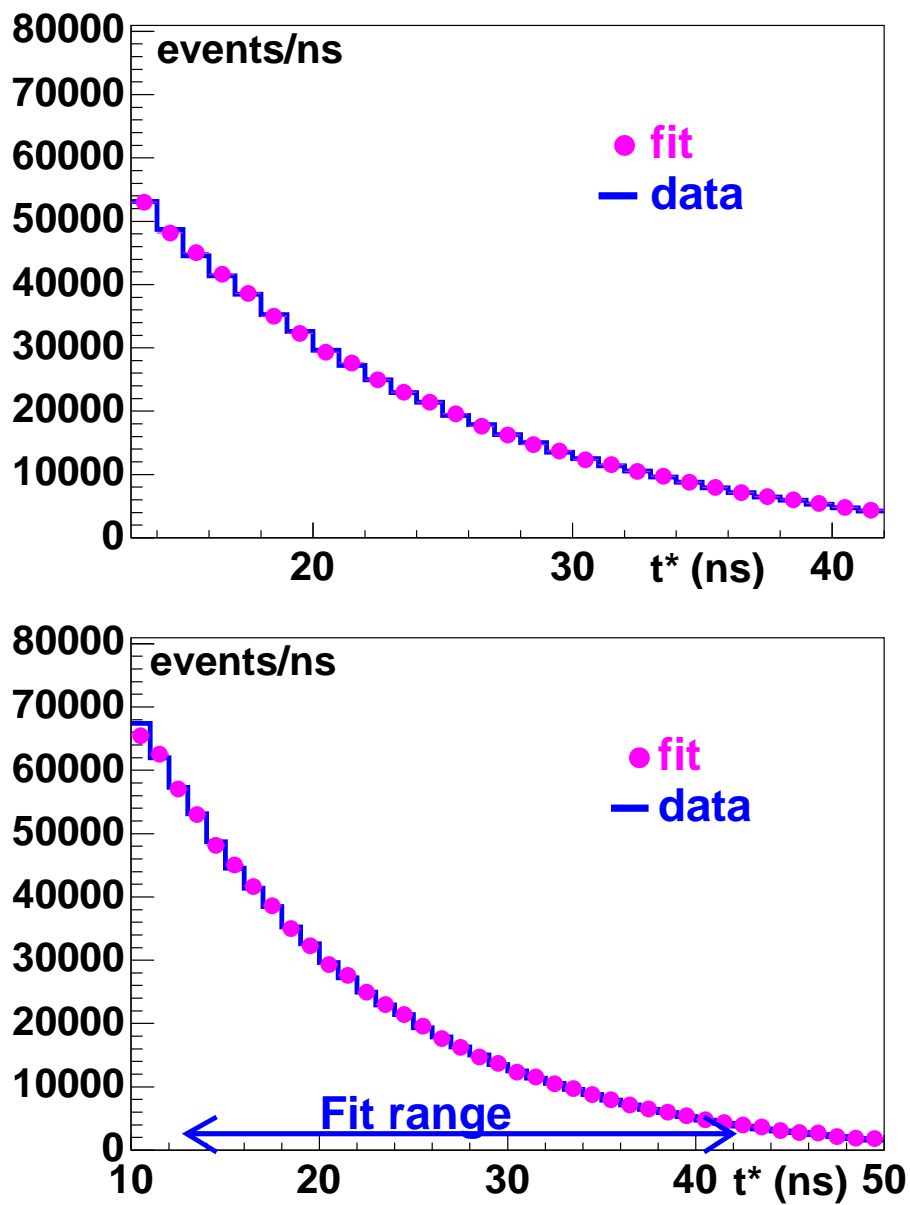
Figure 5.66: Fit to the K^+ proper time distribution: in blue the data distribution, in pink the *expected* histo distribution.
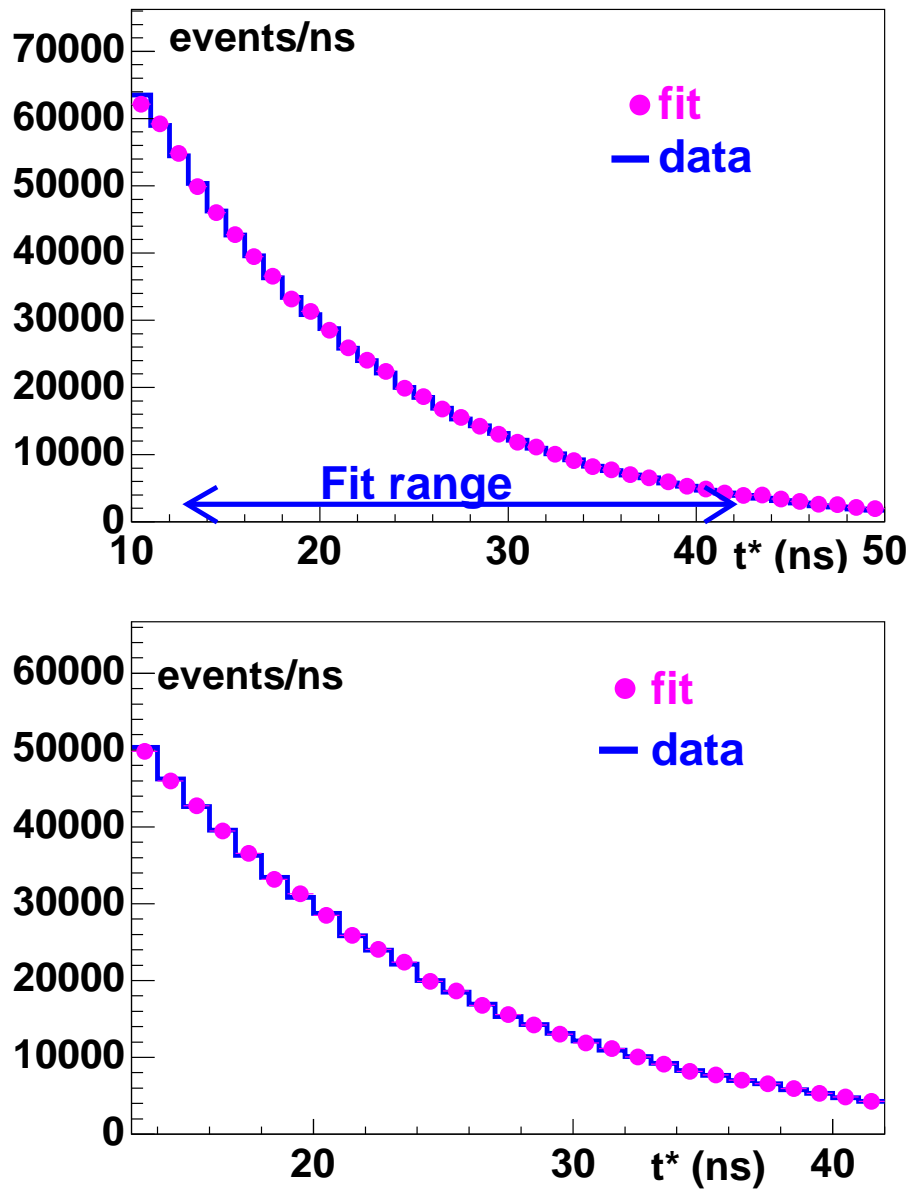
Figure 5.67: Fit to the K^- proper time distribution: in blue the data distribution, in pink the *expected* histo distribution.
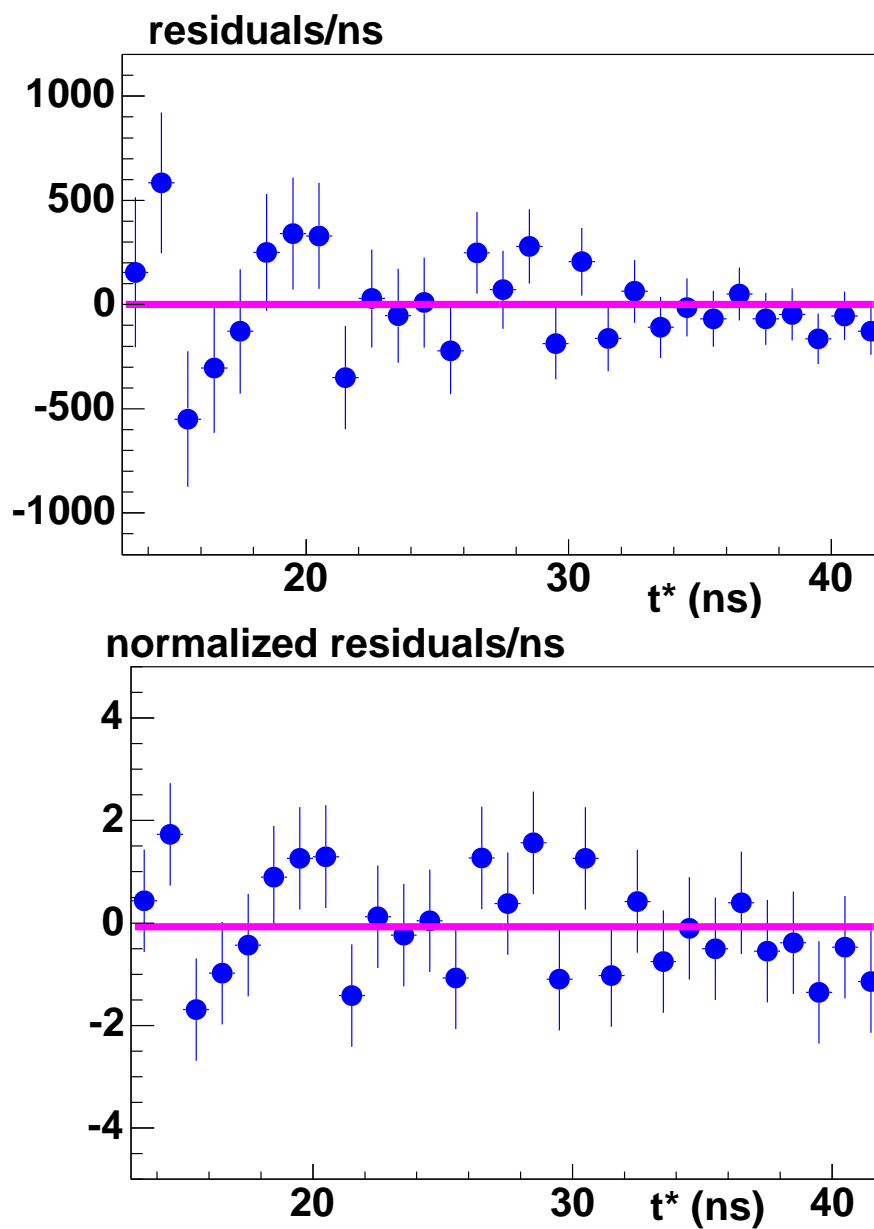
Figure 5.68: K^+ residuals (up) and the normalized residuals (down), in the region between 12 and 42 ns, fitted with a constant.
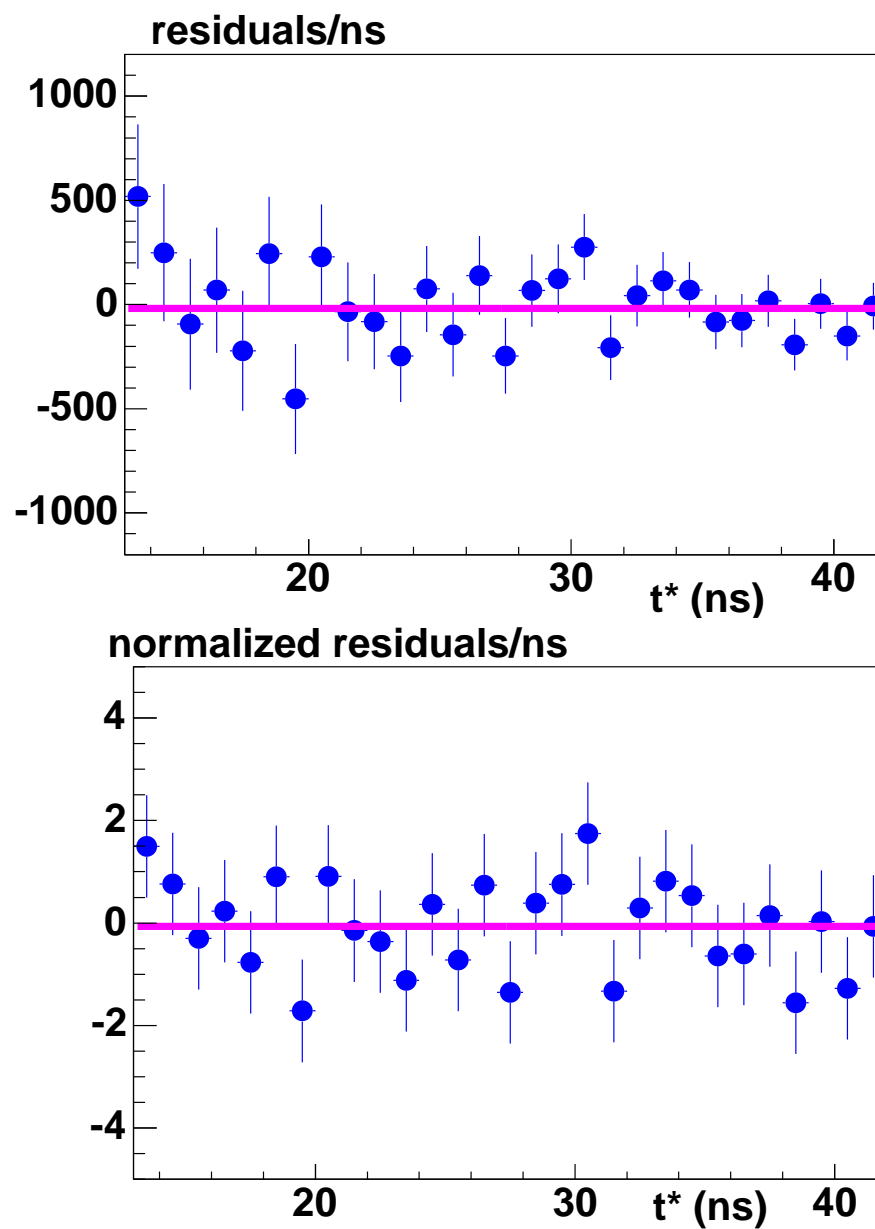
Figure 5.69: K^- residuals (up) and the normalized residuals (down), in the region between 12 and 42 ns, fitted with a constant.

5.9 Study of the systematics

For both the methods we used the same data sample for the evaluation of the reconstruction efficiency of the kaon decay vertex and for the evaluation of the proper time distribution. In order to determinate any possible correlation between the measurement of the efficiency and the proper time distribution we divided the data sample into two subsamples. For both these subsamples we evaluate the reconstruction efficiency of the kaon decay vertex and the proper time distribution. We measured the charged kaon lifetime for the four possible combinations (1-1, 1-2, 2-1, 2-2) for the two different methods. Results do not change using the proper time distribution evaluated in the first (second) subsample and the efficiency evaluated in the same subsample or in the other.
We can say that no one correlation is introduced by the use of the same data sample for the evaluation of the reconstruction efficiency of the kaon decay vertex and for the evaluation of the proper time distribution.
In order to check the goodness of the equation 5.73, used for the evaluation of the statistical fluctuations of the *expected* histo, we developed a MonteCarlo toy. For each bin j we generate poissionian random numbers with mean given by:

$$N_j^{rnd} = \sum_{i=1}^{Nbins} s_{ji} \times \epsilon_i^{rnd} \times \epsilon_i^{corr\ rnd} \times N_i^{theo}, \tag{5.113}$$

where ϵ_i^{rnd} is a random number generated using a gaussian whose mean and sigma are the value of the reconstruction efficiency, ϵ_i, and its error, σ_{ϵ_i}, evaluated in the i-th bin respectively; $\epsilon_i^{corr\ rnd}$ is a random number generated using a gaussian whose mean and sigma are the value of the correction to the reconstruction efficiency, ϵ_i^{corr}, and its error, $\sigma_{\epsilon_i^{corr}}$, evaluated in the i-th bin respectively.
For each bin j the Root Mean Square of the random poissionian numbers generated with mean N_j^{rnd} are used as statistical fluctuations of the *expected* histo. The result of the fit using this formula for the error doesn't change.

5.9.1 Length measurement

We have studied the following sources of systematic uncertainties for the:

1. fit stability as a function of the range used;

2. fit stability as a function of the bin used for the proper time distribution;

3. fit stability as a function of the efficiency correction;

4. correction due to a not correct evaluation of the Beam Pipe and DC walls thicknesses;

5. fit stability as a function of the p_K^* cut.

A more detailed discussion of the systematics studiy follows.

Fit range

We fitted the distribution using various different ranges in the *golden* region between 15 and 35 ns. The maximum fluctuation of the results is about 10 ps, which we take as systematic uncertainty.

Binning

We made the fit also using a bin size of 500 and 250 ps (one half and one third of the nominal bin size respectively). The maximum fluctuation of the result is of the order of 10 ps for both the charges which we take as systematic uncertainty.

Efficiency correction

We made the fit also without the efficiency correction. The maximum fluctuation of the measure is of the order of 15 ps for both the charges. Therefore we conservatively estimate the systematic error given by the efficiency correction to be about 15 ps .

Beam Pipe and DC wall thicknesses

We evaluate the proper time distribution without taking into account the energy loss in the Beam Pipe and in the DC walls. The maximum fluctuation of the result is of the order of 100 ps for the Beam Pipe and 150 ps for the DC walls. But the uncertainty on the Beam Pipe and DC walls thicknesses is about 10%. Therefore we conservatively estimate the systematic error given by uncertainty on the Beam Pipe thickness to be about 10 ps and the one given by uncertainty and DC wall thickness to be about 15 ps.

$\mathbf{P}_K^*$ cut

We made the fit with different p_K^* cuts between 50 and 150 MeV/c. The maximum fluctuation of the measure is of the order of 15 ps for both the charges. Therefore we conservatively estimate the systematic error given by the efficiency correction to be about 15 ps .

5.9.2 Total systematic uncertainty

The total systematic uncertainty evaluated is of the order of 31 ps.

$$\tau = (12.364 \pm 0.031_{stat} \pm 0.031_{syst}) \text{ ns.} \tag{5.114}$$

Sources of systematic uncertainties	Systematic uncertainties (ps)
Fit range	$\pm$ 10
binning	$\pm$ 10
efficiency correction	$\pm$ 15
Beam Pipe thickness	$\pm$ 10
DC wall thickness	$\pm$ 15
P_K^*	$\pm$ 15

Table 5.2: Sources of systematic uncertainties evaluated.

5.9.3   Time measurement

We have studied the following sources of systematic uncertainties on the measured branching ratio:

1. fit stability as a function of the range used;

2. fit stability as a function of the bin used for the proper time distribution;

3. fit stability as a function of the efficiency correction;

4. correction due to a not correct evaluation of the Beam Pipe and DC walls thicknesses;

5. fit stability as a function of the efficiency cuts;

6. fit stability as a function of the T_ϕ^0;

A detailed discussion of the systematic studies follows.

Fit range

We evaluated the fit in the whole region between 13 and 42 ns. The maximum fluctuation of the measure is of the order of 10 ps for both the charges. Therefore we extimate the systematic error given by the range stability to be about 10 ps.

Binning

We made the fit also using a bin size of 2 ns (two times nominal bin size respectively). The maximum fluctuation of the result is of the order of 10 ps for both the charges which we take as systematic uncertainty.

Efficiency correction

We made the fit also without the efficiency correction. The maximum fluctuation of the measure is of the order of 10 ps for both the charges. Therefore we estimate the systematic error given by the efficiency correction to be about 10 ps.

Efficiency cuts

We made the fit applying different p_K^* cuts to the efficiency, between 50 and 150 MeV/c. The maximum fluctuation of the measure is of the order of 10 ps for both the charges. Therefore we conservatively estimate the systematic error given by the efficiency correction to be about 10 ps

Beam Pipe and DC wall thicknesses

We evaluate that the fluctuation of the measurement, if we assume an uncertainty of the order of 10% on the thicknesses of the Beam Pipe and DC walls, is negligible. This uncertainty is a construction parameter.

T_ϕ^0

Using the two different tag, $K \to \mu\nu$ and $K \to \pi\pi^0$, we estimate that fluctuation of the measurement, as a function of the T_ϕ^0 is negligible.

5.9.4 Total systematic uncertainty

The total systematic uncertainties evaluated is of the order of 20 ps.

$$\tau = (12.337 \pm 0.030_{stat} \pm 0.020_{syst}) \text{ ns.} \tag{5.115}$$

Sources of systematic uncertainties	Systematic uncertainties(ps)
Fit range	$\pm\ 10$
binning	$\pm\ 10$
efficiency correction	$\pm\ 10$
Efficiency cuts	± 10

Table 5.3: Sources of systematic uncertainties evaluated.

5.10 Correlation and weighted mean

In order to evaluate the weighted mean between the two methods we calculate the statistical correlation between the two methods. Therefore we divide the data sample into five subsamples. For each subsample, and for each method, we evaluate the proper time distribution and its efficiency.
Then we evaluate, for each subsample and for each method, the value of the charged kaon lifetime, see table 5.4. The correlation is given by:

subsample	length fit(ns)	time fit(ns)
1	12.368	12.307
2	12.393	12.312
3	12.389	12.362
4	12.351	12.301
5	12.330	12.326

Table 5.4: In the table the weighted mean for the different techniques and for the different subsamples are shown.

$$\rho = \frac{1}{N-1} \frac{\sum_{i=1}^{N}(\tau_l - \tau_l^i)(\tau_t - \tau_t^i)}{\sigma_l \sigma_t} \tag{5.116}$$

where N is the number of subsample, τ_l^i is the value of the lifetime for the first method evaluated on the i-th subsample, τ_l is the mean of the values of the lifetime for the first method evaluated on the different subsamples, τ_t^i is the value of the lifetime for the second method evaluated on the i-th subsample, τ_t is the mean of values of the lifetime for the second method evaluated on the different samples, σ_l and σ_t are the standard deviation of the measurements evaluated on the five subsample for the first and the second method respectively.
The value of the statistical correlation is:

$$\rho = 0.307 \ . \tag{5.117}$$

The weighted mean between the two methods and its error is given by following equations:

$$\tau = \frac{\left(\sigma_{t\ tot}^2 - \rho\ \sigma_{t\ stat}\sigma_{l\ stat}\right) \times \tau_l + \left(\sigma_{l\ tot}^2 - \rho\ \sigma_{l\ stat}\sigma_{t\ stat}\right) \times \tau_t}{\sigma_{t\ tot}^2 + \sigma_{l\ tot}^2 - 2\rho\ \sigma_{t\ stat}\sigma_{l\ stat}} \tag{5.118}$$

$$\sigma_\tau = \sqrt{\frac{\sigma_{l\ tot}^2\sigma_{t\ tot}^2 - \rho^2\sigma_{l\ stat}^2\sigma_{t\ stat}^2}{\sigma_{l\ tot}^2 + \sigma_{t\ tot}^2 - 2\rho\ \sigma_{l\ stat}^2\sigma_{t\ stat}^2}} \tag{5.119}$$

where $\sigma_{l\ tot}$ and $\sigma_{t\ tot}$ are the total errors on the length and the time measurement $\sigma_{l\ stat}$ and $\sigma_{t\ stat}$ are the statistical errors on the length and the time measurement, respectively. The corresponding result is:

$$\tau = (12.347 \pm 0.030) \ \text{ns} \tag{5.120}$$

5.11 CPT test

The comparison of K$^+$ and K$^-$ lifetimes is a test of CPT invariance which guarantees the equality of the decay lifetimes for particle and antiparticle.

For the positive kaons the average of the two methods, taking into account the correlation of the statistical errors, and the systematic errors is:

$$\tau^+ = (12.325 \pm 0.038) \text{ ns} \tag{5.121}$$

and for the negative kaons is:

$$\tau^- = (12.374 \pm 0.040) \text{ ns} \tag{5.122}$$

From these we obtain:

$$\tau^- - \tau^+ = (49 \pm 50) \text{ ps} \tag{5.123}$$

$$\frac{\tau^-}{\tau^+} = 1.004 \pm 0.004 \tag{5.124}$$

The result agrees well with CPT invariance at the 4 per mil level.

Chapter 6

Conclusions

We have done a direct measurement of the $K^{\pm}$ lifetime tagged by $K^{\mp} \to \mu^{\mp} \overset{(-)}{\nu}_{\mu}$ events. Using a data sample of 210 pb^{-1} we obtained

$$\tau = (12.347 \pm 0.030) \text{ ns.} \qquad (6.1)$$

The value obtained agrees, within the errors, with the result given by Ott *et al.*, [28]:

$$\tau = (12.380 \pm 0.016) \text{ ns} \qquad (6.2)$$

and with the PDG fit, [26]:

$$\tau = (12.384 \pm 0.024) \text{ ns} \qquad (6.3)$$

For the positive kaons the average of the two methods, taking into account the correlation of the statistical errors, and the systematic errors is:

$$\tau^{+} = (12.325 \pm 0.038) \text{ ns} \qquad (6.4)$$

and for the negative kaons is:

$$\tau^{-} = (12.374 \pm 0.040) \text{ ns} \qquad (6.5)$$

From these measurement we obtain:

$$\tau^- - \tau^+ = (49 \pm 50) \text{ ps} \tag{6.6}$$

$$\frac{\tau^-}{\tau^+} = 1.004 \pm 0.004 \tag{6.7}$$

It has to be compared with the previous measurement made by Lobkowitz *et al.* [27]:

$$\frac{\tau^-}{\tau^+} = 1.0009 \pm 0.0008 \tag{6.8}$$

The result agrees well with CPT invariance at the 0.4% level and with the previous result [27]. If we average this result with the Fitch one [29] and the ones given in eq. 1.23 and 1.22 we obtain:

$$\tau(K^+) = (12.387 \pm 0.018) \text{ ns } . \tag{6.9}$$

The central value is the same one given by the PDG fit [26] with an improvement on the uncertainty of the order of 25% without any scale factor, see fig 6.1.
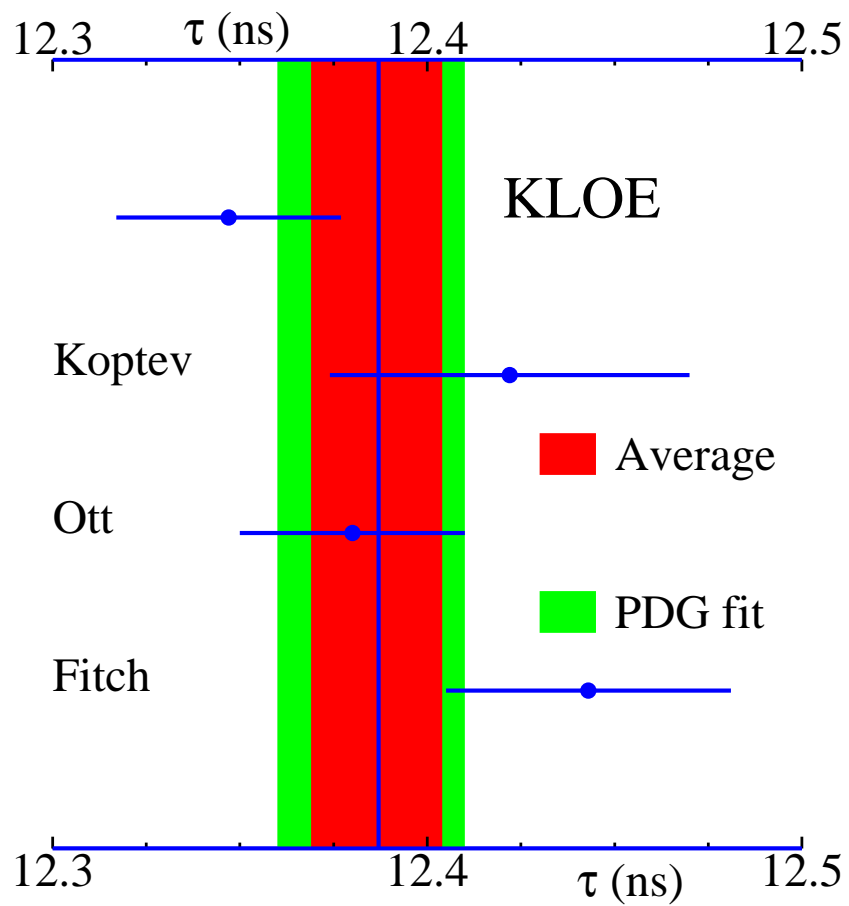
Figure 6.1: Charged kaon lifetime average using the correct values given in the text.

Bibliography

[1] M. Kobayashi and T. Maskawa, Prog. Theor. Phys. **49** (1973) 652.

[2] N. Cabibbo, Phys. Rev. Lett. **10** (1963) 531.

[3] L. L. Chau and W. Y. Keung, Phys. Rev. Lett. **53** (1984) 1802.

[4] L. Wolfenstein, Phys. Rev. Lett. **51** (1983) 1945.

[5] R. Kowalewski and T. Mannel [Particle Data Group Collaboration], Phys. Lett. B **867** (2006) 1.

[6] E. Blucher and W.J. Marciano [Particle Data Group Collaboration], Phys. Lett. B **677** (2006) 1.

[7] H. Leutwyler and M. Roos, Z. Phys. C **25** (1984) 91.

[8] A. Czarnecki, W.J. Marciano, Alberto Sirlin Phys. Rev. **D70:093006** 2004. [arXiv:hep-ph/0406324]

[9] A. Sirlin, Nucl. Phys. B **196** (1982) 83.

[10] V. Cirigliano, M. Knecht, H. Neufeld, H. Rupertsberger and P. Talavera, Eur. Phys. J. C **23** (2002) 121 [arXiv:hep-ph0110153].

[11] V. Cirigliano, H. Neufeld and H. Pichl, Eur. Phys. J. C **35** (2004) 53 [arXiv:hep-ph0401173].

[12] D. Becirevic *et al.*, [arXiv:hep-ph0403217].

[13] N. Cabibbo, E. C. Swallow and R. Winston, Ann. Rev. Nucl. Part. Sci. **53** (2003) 39 [arXiv:hep-ph/0307298].

[14] F. Mescia, for the KLOE collaboration, ICHEP 2004 presentation http://www.ihep.ac.cn/data/ichep04/ppt/8_cp/8-0811-antnoelli-m.pdf

[15] M. Palutan, for the KLOE collaboration, Kaon 2007 presentation http://www.lnf.infn.it/conference/kaon07/

[16] C. T. H. Davies *et al.* [HPQCD Collaboration], Phys. Rev. Lett. **92** (2004) 022001 [arXiv:hep-lat/0304004].

[17] W. J. Marciano and A. Sirlin, Phys. Rev. Lett. **71** (1993) 3629.

[18] W. J. Marciano and A. Sirlin, Phys. Rev. Lett. **56** (1986) 22.

[19] A. Sirlin, Rev. Mod. Phys. **50** (1978) 573 [Erratum-ibid. **50** (1978) 905].

[20] T. Kinoshita, Phys. Rev. Lett. **2** (1959) 477.

[21] M. Finkemeier, Phys. Lett. B **387** (1996) 391 [arXiv:hep-ph/9505434].

[22] K. Hagiwara *et al.* [Particle Data Group Collaboration], Phys. Rev. D **66** (2002) 010001.

[23] C. Aubin *et al.* [MILC Collaboration], arXiv:hep-lat/0409041.

[24] A. Czarnecki, W. J. Marciano and A. Sirlin, arXiv:hep-ph/0406324.

[25] I. H. Chiang, J. L. Rosen, S. Shapiro, R. Handler, S. Olsen and L. Pondrom, Phys. Rev. D **6** (1972) 1254.

[26] W.-M. Yao *et al.* (Particle Data Group Collaboration) *Journal of Physics* **G 33, 1** 2006 W. M. Yao *et al.*, J. Phys. G. 33,1 (2006).

[27] F. Lobkowicz *et al.* 1970. Phys.Rev.185:1676-1687,1969.

[28] R.J. Ott *et al.*. 1971. Phys.Rev. D3:52-56,1971.

[29] V. L. Fitch *et al.* Phys. Rev. 140, B1088 - B1091 1965

[30] V.P. Koptev *et al.* 1995. JETP Lett.62:877-881,1995, Pisma Zh.Eksp.Teor.Fiz.61:865-868,1995.

[31] "The DAΦNE Physics handbook", Ed. L. Maiani, G. Pancheri e N. Paver, I.N.F.N. L.N.F. (1995).

[32] F. Ambrosino et al. "The tracking detector of the KLOE experiment", Nucl. Inst. Meth. A 488, 1-23 2002.

[33] M. Adinolfi et al. "The KLOE electromagnetic calorimeter", Nucl. Inst. Meth. A **482** (2002) 363-385.

[34] S. Eidelman *et al.* [Particle Data Group Collaboration], Phys. Lett. B **592** (2004) 1.

[35] S. Bertolucci *et al.*, KLOE *note* (62) (1993).

[36] A. Aloisio et al. "The KLOE Data Acquisition system, addendum to the KLOE technical proposal", LNF-95/014(IR) (1995).

[37] R. Brun et al. GEANT3, CERN-DD/EE/84-1 (1984).

[38] R. Brun et al. GEANT: Simulation for particle physics experiments, user guide and reference manual, CERN-DD-78-2-REV (1978).

[39] C. M. Carloni Calame et al. The BABAYAGA event generator, hep-ph/0312014 (2003).

[40] W. Kim *et al.*, KLOE *memo* (6) (1996).

[41] A. Antonelli *et al.*, KLOE *note* (157) (1996).

[42] M. Incagli *et al.*, KLOE *memo* (147) (1996).

[43] K. W. Edwards *et al.*, Nucl. Instrum. Meth. A **252** (1986) 384.

[44] P. De Simone *et al.*, Ph.D. Thesis, Universitá degli studi di Roma "La Sapienza",(1994).

[45] V. S. Demidov, V. A. Dobrokhotov, E. A. Lyublev and A. N. Nikitenko, Sov. J. Nucl. Phys. **52** (1990) 1006 [Yad. Fiz. **52** (1990) 1595].

[46] F. Ambrosino *et al.* [KLOE Collaboration], Nucl. Instrum. Meth. A **534** (2004) 403.

[47] M. Adinolfi *et al.* [KLOE Collaboration], Nucl. Instrum. Meth. A **492** (2002) 134.

[48] F. Ambrosino, E. De Lucia, P. de Simone, P. Massarotti and V. Patera *Measurement of the reconstruction efficiency of the charged kaon decays.*, KLOE Memo **320** (2005).

List of Figures

160

161

List of Tables